Multiplicity dependence of charged-particle production in high-energy collisions at the LHC

Dissertation

zur Erlangung des Doktorgrades der Naturwissenschaften

vorgelegt beim Fachbereich Physik der Johann Wolfgang Goethe-Universität in Frankfurt am Main

von

Mario Krüger

aus Ilmenau

Frankfurt am Main 2024 (D 30)

Vom Fachbereich Physik der Johann Wolfgang Goethe-Universität als Dissertation angenommen.

Dekan: Prof. Dr. Roger Erb

Gutachter: Prof. Dr. Henner Büsching

Prof. Dr. Harald Appelshäuser

Datum der Disputation: 06.06.2025

Zusammenfassung

Hochenergetische Teilchenkollisionen erlauben es, die Struktur und Eigenschaften von Materie experimentell zu untersuchen. Am Large Hadron Collider (LHC) werden hierzu Atomkerne von Wasserstoff oder schwereren Elementen in zwei gegenläufigen Strahlrohren auf nahezu Lichtgeschwindigkeit beschleunigt und an vier Interaktionspunkten zur Kollision gebracht. Bei inelastischen Kollisionen dieser Atomkerne interagieren die fundamentalen Bausteine der Materie, die Quarks und Gluonen, miteinander und es entstehen neue Teilchen. Ausschlaggebend sind hierbei Prozesse der starken Wechselwirkung, die theoretisch durch die Quantenchromodynamik (QCD) beschrieben werden. In einer Teilchenkollision dominieren Interaktionen mit wenig Impulsübertrag, für die sich aus der QCD keine direkten Vorhersagen ableiten lassen. Daher werden diese Prozesse durch phänomenologische, QCD-inspirierte Modelle beschrieben, die in Monte Carlo (MC)-Eventgeneratoren implementiert sind. Um diese Modelle zu verifizieren und zu verbessern, benötigt es eine präzise experimentelle Vermessung des Endzustandes der Teilchenkollisionen. Hierbei leistet das ALICE-Experiment am LHC einen entscheidenden Beitrag. Der Forschungsschwerpunkt von ALICE ist die Untersuchung eines Zustandes heißer und dichter Materie, der in Schwerionenkollisionen erzeugt werden kann und nach heutigem Verständnis kurz nach dem Urknall vorherrschte.

Ziel der vorliegenden Arbeit ist es einerseits, die Produktion geladener Teilchen in verschiedenen Kollisionssystemen und bei unterschiedlichen Schwerpunktsenergien systematisch zu vergleichen, und sie andererseits den Vorhersagen theoretischer Modelle gegenüberzustellen. Hierzu wird eine umfangreiche Messung der Teilchenproduktion in Proton–Proton (pp), Proton–Blei (p–Pb), Xenon–Xenon (Xe–Xe) und Blei–Blei (Pb–Pb) Kollisionen präsentiert. Die verwendeten Messdaten wurden während der ersten beiden Strahlzeiten des LHC, Run 1 (2009 – 2013) und Run 2 (2015 – 2018), mit dem ALICE-Experiment aufgezeichnet und umfassen zehn verschiedene Kollisionsszenarien mit Schwerpunktsenergien pro Nukleonen-Paar im Bereich von 2.76 TeV $\leq \sqrt{s_{\rm NN}} \leq 13$ TeV. Für jeden der zehn Datensätze werden zwei charakteristische Größen bestimmt: Zum einen die Wahrscheinlichkeit, mit der in einer Kollision eine bestimmte Anzahl geladener Teilchen, auch Multiplizität genannt, erzeugt wird. Zum anderen die Produktionsrate der geladenen Teilchen in Abhängigkeit

von deren Transversalimpuls $p_{\rm T}$ sowie der Multiplizität $N_{\rm ch}$ der jeweiligen Kollision. Für die experimentelle Bestimmung der Observablen, die beide durch den Messprozess beeinflusst werden, ist eine Korrektur der gemessenen Daten notwendig, denn mit den Detektoren von ALICE können weder alle Kollisionen noch alle darin entstehenden Teilchen vollständig rekonstruiert werden. Zudem lassen sich sowohl die Multiplizität als auch der Transversalimpuls nur mit begrenzter Genauigkeit bestimmen. Um diese Effekte zu quantifizieren, sind MC-Simulationen erforderlich, bei denen Teilchen zunächst durch einen Eventgenerator erzeugt und anschließend durch eine virtuelle Nachbildung des ALICE-Experiments propagiert werden. Die von den Eventgeneratoren vorhergesagte Teilchenzusammensetzung kann jedoch falsch sein, was wiederum die damit bestimmten Messeffekte beeinflusst. Dieses Problem kann durch eine auf Messungen basierende Umgewichtung der Teilchenhäufigkeiten in der MC-Simulation behoben werden. Die so angepasste Simulation ermöglicht es, den Einfluss des Messprozesses präzise und realitätsnah zu quantifizieren.

Der Effekt der Messung auf die Observablen wird mithilfe einer iterativen Entfaltungsprozedur korrigiert. Mit dieser etablierten Methode lässt sich direkt die korrigierte Multiplizitätsverteilung bestimmen. Für die Messung der Produktionsrate geladener Teilchen in Abhängigkeit von $p_{\rm T}$ und $N_{\rm ch}$ kann die Methode jedoch nicht ohne Weiteres angewandt werden, da die verfügbare MC-Statistik hierfür nicht ausreicht. Im Rahmen dieser Arbeit wird daher eine sequentielle Entfaltungsprozedur entwickelt. Diese neue Methode erlaubt es, die $p_{\rm T}$ Spektren für einzelne Multiplizitäten zu bestimmen, anstatt, wie in vorhergehenden Analysen, nur für breite Multiplizitätsintervalle.

Die korrigierten Observablen können nun für die zehn betrachteten Datensätze verglichen werden. Dabei werden einerseits die Multiplizitätsverteilungen $P(N_{\rm ch})$ und andererseits der Mittelwert $\langle p_{\rm T} \rangle$ und die Standardabweichung $\sigma(p_{\rm T})$ der $N_{\rm ch}$ -abhängigen Transversalimpulsspektren betrachtet. Für jedes Kollisionssystem folgen die drei Observablen jeweils einem charakteristischen Verlauf und weisen innerhalb des Systems eine deutliche Energieabhängigkeit auf.

Des Weiteren wird untersucht, ob sich die Observablen in eine für das Kollisionssystem charakteristische, energieunabhängige Form transformieren lassen. Im Falle der Multiplizitätsverteilungen wird dabei die Koba-Nielsen-Olesen (KNO) Skalierung verwendet. Für die fünf verschiedenen pp Kollisionsenergien sowie die drei verschiedenen

AA (i.e. Xe–Xe und Pb–Pb)-Kollisionsenergien wird fast über den ganzen betrachteten Multiplizitätsbereich eine Übereinstimmung der KNO-skalierten Multiplizitätsverteilungen innerhalb von 20 % beobachtet. Im Falle der beiden p–Pb Kollisionsenergien liegt die Abweichung der Skalierung unter 10 %. Da vorangegangene Studien sich primär auf e^+e^- , p \bar{p} und pp Kollisionen fokussierten, geben diese Ergebnisse zum ersten Mal Einblick in die KNO-Skalierung der Multiplizitätsverteilungen größerer Kollisionssysteme.

Für die Betrachtung des Mittelwertes $\langle p_{\rm T} \rangle$ und der Standardabweichung $\sigma(p_{\rm T})$ der Transversalimpulsspektren als Funktion von $N_{\rm ch}$ in einer energieunabhängigen Form wird anders verfahren. Hier werden die jeweiligen Observablen durch die multiplizitätsintegrierten Werte $\langle p_{\rm T} \rangle_{\rm incl}$ bzw. $\sigma(p_{\rm T})_{\rm incl}$ und die mittlere Multiplizität $\langle N_{\rm ch} \rangle$ geteilt. Dabei wird beobachtet, dass die Größen einem universellen Verlauf folgen, welcher nur vom Kollisionssystem (pp, p–Pb oder AA) abhängt. Im Gegensatz zu den skalierten Multiplizitätsverteilungen wird eine bessere Übereinstimmung der verschiedenen Kollisionsenergien bei diesen Messgrößen festgestellt. Somit scheint für jedes Kollisionssystem ein allgemeiner Zusammenhang zwischen der produzierten Teilchenanzahl und deren Transversalimpulsverteilungen zu bestehen.

Der Vergleich der $p_{\rm T}$ Spektren verschiedener Kollisionssysteme zeigt, dass für pp und p-Pb Kollisionen mit steigender Multiplizität die Teilchen häufiger mit hohen Transversalimpulsen erzeugt werden. Gegenteiliges wird für AA Kollisionen beobachtet. Diese Unterdrückung der Teilchenproduktion bei hohem $p_{\rm T}$ ist vermutlich ein Resultat des Energieverlustes der Quarks und Gluonen in der heißen und dichten Materie, die in einer Schwerionenkollision erzeugt wird.

Die gewonnenen Erkenntnisse über das Verhalten der betrachteten Observablen in unterschiedlichen Kollisionssystemen und bei unterschiedlichen Schwerpunktsenergien werden den Vorhersagen von MC-Eventgeneratoren gegenübergestellt, die das aktuelle theoretische Verständnis einer Teilchenkollision abbilden. Der Vergleich mit den Messdaten ermöglicht es, die Validität der zugrundeliegenden Modelle zu überprüfen und somit zu deren Verbesserung beizutragen.

In der vorliegenden Arbeit werden die Multiplizitätsverteilungen sowie $\langle p_{\rm T} \rangle$ und $\sigma(p_{\rm T})$ als Funktion von $N_{\rm ch}$ für pp und p–Pb Kollisionen bei verschiedenen Energien mit den MC-Eventgeneratoren PYTHIA und EPOS LHC verglichen. Beide Eventgeneratoren

sagen für diese Observablen unterschiedliche Verläufe sowohl als Funktion der Multiplizität als auch der Energie voraus. Für pp Kollisionen liegen die Abweichungen zu den Messdaten im Fall der Multiplizitätsverteilungen über weite Bereiche unter 20% sowie für $\langle p_{\rm T} \rangle$ und $\sigma(p_{\rm T})$ als Funktion von $N_{\rm ch}$ unter 10% und sind somit insgesamt relativ gering. Im Allgemeinen produzieren beide Eventgeneratoren bei niedrigen Multiplizitäten einen zu geringen mittleren Transversalimpuls und zu schmale $p_{\rm T}$ Verteilungen. Bei der Beschreibung von p–Pb Kollisionen zeigt sich ein deutlicher Unterschied zwischen den beiden MC-Eventgeneratoren. EPOS LHC beschreibt die gemessenen Observablen besser als PYTHIA, unterschätzt jedoch die Produktionswahrscheinlichkeit von Kollisionen mit hohen Multiplizitäten. Beide Eventgeneratoren sagen systematisch zu geringe Mittelwerte und Breiten der $p_{\rm T}$ Spektren voraus, besonders ausgeprägt für PYTHIA, das eine Abweichung von 20% zu den experimentellen Ergebnissen aufzeigt. In AA Kollisionen werden die drei Observablen mit dem HIJING-MC-Eventgenerator verglichen, der insbesondere den mittleren Transversalimpuls in zentralen Kollisionen um etwa 20% unterschätzt.

Für den mittleren Transversalimpuls als Funktion der Multiplizität in pp, p–Pb und Pb–Pb Kollisionen bei einer Schwerpunktsenergie von $\sqrt{s_{\rm NN}}=5.02\,{\rm TeV}$ werden die Ergebnisse dieser Arbeit zudem mit Vorhersagen von PYTHIA, EPOS3 und einer hydrodynamischen Rechnung verglichen. Keine der drei theoretischen Vorhersagen kann die Messung gut beschreiben. Dies verdeutlicht die Relevanz der in dieser Arbeit präsentierten und in Ref. [1] publizierten Ergebnisse zum Verifizieren und Bewerten der verschiedenen theoretischen Modellierungen von Teilchenproduktion in Hochenergiekollisionen. Für eine nachhaltige Verwendbarkeit sind die Messergebnisse in einer zentralen Datenbank, HEPData, archiviert und stehen dem Forschungsfeld somit für weiterführende Studien und zukünftige Modellvergleiche zur Verfügung. Zudem ist die Analyse in RIVET, einem in der Hochenergiephysik weit verbreiteten Programm zum Vergleichen von experimentellen Messungen mit MC-Eventgeneratoren, implementiert. Hierdurch können die Ergebnisse dieser Arbeit zu einer Verbesserung der theoretischen Modellierung von Hochenergiekollisionen beitragen.

Contents

1	Intr	oduction	1					
	1.1	The strong interaction						
	1.2	High-energy collisions						
		1.2.1 Proton-proton collisions	5					
		1.2.2 Heavy-ion collisions	LC					
	1.3	Observables	5					
		1.3.1 Multiplicity distributions	5					
		1.3.2 Transverse-momentum spectra	8					
		1.3.3 $\langle p_{\rm T} \rangle$ as a function of $N_{\rm ch}$	21					
	1.4	Unfolding experimental data	23					
2	Exp	periment and data preparation 3	1					
	2.1	The Large Hadron Collider	31					
	2.2	The ALICE experiment	32					
		2.2.1 V0 detector	34					
		2.2.2 Inner Tracking System	35					
		2.2.3 Time Projection Chamber	36					
	2.3	Data preprocessing	8					
	2.4	Monte Carlo simulations	11					
3	Dat	a analysis 4	.3					
	3.1	Workflow	13					
	3.2	Datasets	14					
	3.3	Event class and event selection						
	3.4	Track selection	19					
3.5 P		Particle-composition correction	52					
	3.6	Unfolding corrections	54					
		3.6.1 Multiplicity distributions	66					
		3.6.2 Multiplicity-dependent $p_{\rm T}$ spectra 6	60					
	3.7	Systematic uncertainties	75					

Contents

4	Res	sults and discussion		81
	4.1	Experimental results		
	4.2	Comparison to published experimental results		
	4.3	Comparison to theoretical models		95
	4.4	Supplementary studies		102
		4.4.1	Extrapolations to unmeasured pp collision energies	103
		4.4.2	Outlook: First results from LHC Run 3	106
5	Sun	nmary		109

1 Introduction

In high-energy nuclear collisions, the strong interaction between quarks and gluons causes the creation of new particles. The underlying physical processes of this particle production are described by the theory of quantum chromodynamics (QCD). Due to the nature of the strong interaction, only hard parton-parton scattering can be calculated analytically through perturbative methods. However, the processes dominating particle production often involve small momentum transfers between the partons and hence their theoretical description relies on QCD-inspired phenomenological models. These models are implemented in Monte Carlo (MC) event generators simulating the entire evolution of the collision from initial parton-parton interactions towards the formation of final-state hadrons. To improve our understanding of the QCD mechanisms involved in particle production, these theoretical predictions need to be complemented and constrained by precise measurements characterizing the final state of a collision. Measuring the emerging particles requires sophisticated experiments such as ALICE at the CERN Large Hadron Collider (LHC), whose data is utilized in this work. Over many years of operation, a large amount of proton-proton and heavy-ion collisions at various center-of-mass energies have been recorded with ALICE. This thesis presents a precise measurement of charged-particle production in ten different collision scenarios, enabling a study of the collision-system and energy dependence. In particular, the number $N_{\rm ch}$ of produced charged-particles, denoted as multiplicity, and their momenta $p_{\rm T}$ transverse to the beam direction are considered. The analysis presented in this thesis yields two fundamental observables characterizing the charged-particle final state of a collision: the multiplicity distribution, and the charged-particle production rate as a function of $N_{\rm ch}$ and $p_{\rm T}$. Since detector effects influence the measurement of these observables, the experimental data needs to be corrected by means of an unfolding procedure. To enable a highly granular measurement of the charged-particle production rate as a function of $N_{\rm ch}$ and $p_{\rm T}$, a novel sequential 2D unfolding approach was developed in the course of this work.

The aim of this thesis is to compare the measurements between the different collision systems at different center-of-mass energies and to theoretical predictions of commonly used MC event generators. These comparisons constitute a crucial test for the accuracy of their underlying phenomenological modeling of QCD. The variety of the

considered collision scenarios furthermore gives insight into the validity of the models across collision systems and energies. In addition, the presented measurements are published in Ref. [1] and thus available for validating future theoretical approaches to modeling particle production in high-energy collisions. This contributes to a better understanding of the involved processes of strongly interacting matter.

In the following, a brief introduction to the strong interaction and high-energy particle collisions is given. Subsequently, Section 1.3 contextualizes the observables measured in this work by discussing previous measurements. Section 1.4 details the methodology of the unfolding corrections and Section 2 outlines the experimental setup of ALICE. The different steps of the data analysis are described in Section 3 followed by a discussion of the results in Section 4 and a summary in Section 5.

1.1 The strong interaction

Our everyday life is governed by the long-range forces of gravity and electromagnetism. At subatomic distances, however, the weak and strong interactions within the nucleons become dominant. While the former enables the β -decay of neutrons, the latter binds the nucleons within atomic nuclei, countering the destabilizing repulsion caused by the protons' positive electric charge. In the 1960s, deep inelastic scattering experiments revealed that nucleons consist of fundamental point-like particles, the quarks and gluons. These quarks and gluons interact via the strong interaction which is described by the theory of quantum chromodynamics (QCD) as part of the current standard model of particle physics. In this theoretical framework, six different quark flavors exist, denoted as up, down, strange, charm, top and bottom. The quarks carry one of the color charges red, green, or blue and antiquarks hold the respective anticolor charges. Through the color charge, the quarks interact by exchanging gluons, which are the mediators of the strong interaction. The gluons also carry a color charge, which constitutes a fundamental difference compared to the force carriers of electromagnetism, the photons, which are electrically neutral. In the ordinary matter surrounding us, quarks and gluons are confined in hadrons, forming color-neutral objects. Mesons consist of a quark-antiquark pair, while baryons are composed of three quarks. In addition to these valence quarks defining the particle's quantum numbers, a hadron consists of a

cloud of gluons and dynamically produced quark-antiquark pairs.

In the framework of perturbative QCD (pQCD), any interaction between partons involves an infinite number of possible intermediate virtual particle states. This includes quark-antiquark pair production and gluon self-interactions, which result in screening and antiscreening of the bare color charge, respectively. The latter is the dominant effect and as a result, a parton does not only experience the color field originating from a single quark but rather a much stronger field enhanced by a cloud of gluons surrounding it. High-energy partons can better penetrate this gluon cloud which can be thought of as increasing the magnifying power of viewing the system and, therefore, better resolve the smaller bare color charge of the quark. Consequently, the effective coupling strength $\alpha_{\rm S}$ of the strong interaction between partons depends on the respective probing scale or momentum transfer Q of a process. Considering only first-order perturbations, the effective coupling strength can be expressed as [2]:

$$\alpha_{\rm S}(Q^2) = \frac{\alpha_{\rm S}(\mu^2)}{1 + (33 - 2n_{\rm f})/(12\pi) \cdot \alpha_{\rm S}(\mu^2) \ln(Q^2/\mu^2)} \quad . \tag{1.1}$$

In this equation, $n_{\rm f}$ corresponds to the number of quark flavors contributing at the given energy, and μ is an arbitrary renormalization scale, for which conventionally the mass $m_{\rm Z}$ of the Z boson is used, that lies far away from quark production thresholds and well within the perturbative regime. Figure 1.1 shows experimental measurements of this running coupling as a function of Q together with the QCD prediction using the world average $\alpha_{\rm S}(m_{\rm Z}^2)$ determined by the Particle Data Group [3]. The effective QCD coupling decreases logarithmically as a function of the momentum scale. At large momentum transfers, respectively small distances, the interaction between the partons is weak, resulting in asymptotic freedom of the quarks and gluons. In this hard QCD regime, parton scattering cross-sections can be approximated analytically as an expansion in powers of the coupling constant as higher-order terms become more irrelevant. Conversely, for small momentum transfers or large distances, the coupling constant is large and becomes approximately unity around $1 \,\mathrm{GeV}/c$. The description of these soft QCD processes, which govern the hadron structure is beyond perturbative control and remains a theoretical challenge. It thus relies on phenomenological modeling, which can only be validated and tested by comparison to experimental measurements.

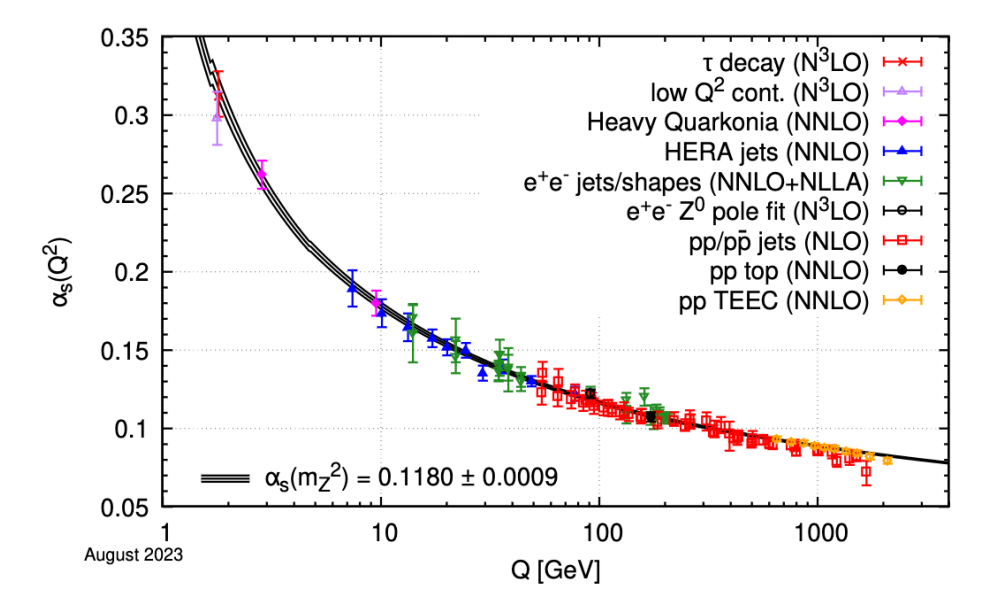


Figure 1.1: Coupling constant $\alpha_{\rm S}$ of the strong interaction as a function of the energy scale Q [3].

Nuclear matter that is heated and compressed up to a sufficient energy density, undergoes a phase transition to a medium of deconfined quarks and gluons. This exotic state of matter, called quark-gluon plasma (QGP), is believed to have been present in the early universe a few microseconds after the Big Bang. Similar high energy-density conditions can be recreated in the laboratory by colliding heavy ions. Ongoing experimental and theoretical efforts aim to better understand the phase diagram of nuclear matter which characterizes the phase transition as a function of temperature and baryon density.

1.2 High-energy collisions

The confinement of quarks and gluons into hadrons poses a challenge to experimentally study the strong interaction. High-energy collisions, where the partons interact and result in the creation of new color-neutral particles, serve as a means to investigate the effects of QCD scattering. The mesons and baryons emerging from such collisions are primarily composed of the three lightest quarks (up, down and strange). Their momentum transverse to the beam axis constitutes the kinematic property most directly related to the underlying production mechanism as it originates purely from the interactions occurring in the collision. In contrast, the longitudinal component of the momentum is boosted in beam direction due to the colliding particles' initial

momenta. A measure for the relativistic velocity along the beamline is the rapidity y. For momenta larger than the mass of the produced particle, y can be approximated by the pseudorapidity η , that only depends on the production angle relative to the colliding particles' original motion. The pseudorapidity represents an easily measurable quantity that in contrast to the rapidity y does not depend on the particle species. Proton-proton collisions constitute the simplest hadronic system for studying vacuum QCD effects. They are, however, already challenging to model due to the large number of involved partons and their predominantly soft interactions. Investigating the formation of a QGP requires significantly higher energy densities which can be achieved by colliding heavy ions. Such a heavy-ion collision represents a system considerably more complicated to describe than pp collisions due to the presence of multiple nucleons as well as the collective behavior and properties of the QGP itself. For experimental observables quantifying QGP effects in heavy-ion collisions, the pp vacuum baseline serves as a crucial reference measurement. Similarly, proton-nucleus collisions allow studying initial state effects due to the presence of an extended heavy ion, without the energy densities being sufficiently high for creating a QGP.

Describing the whole evolution of a high-energy collision requires phenomenological modeling of its different phases which are implemented and combined within event generators. In the following, the common notions of a proton-proton and a heavy-ion collision are outlined. Though the mechanisms affecting particle production can be very different, it is experimentally proven that some final-state observables transition smoothly from one system to the other. Current event generators, therefore, aim to incorporate a coherent description of all collision systems in their respective framework.

1.2.1 Proton-proton collisions

In the following paragraph, different event types of proton-proton (pp) collisions are briefly discussed. Then an overview of the different stages in the evolution of a pp collision is given. Both descriptions focus on phenomena implemented in the widely used event generator PYTHIA [4] whose predictions will be tested against the experimental results of this thesis in Section 4.3.

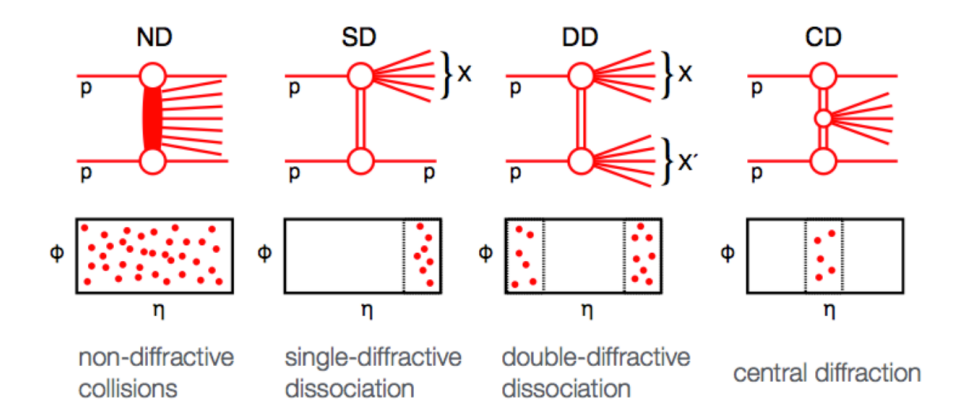


Figure 1.2: Schematic illustration of the different types of pp collisions and their expected η distribution of the produced particles [5].

Event types In most inelastic (INEL) pp collisions, the two incoming protons exchange color charges, generating a field that initiates a complex cascade of particle production. At mid-rapidity, most particles originate from such processes. Another type of pp scattering, called diffraction, corresponds to a colorless exchange of vacuum quantum numbers between the colliding protons [6]. Diffraction is described in the framework of Regge theory [7] and modeled through the exchange of so-called Pomerons [8]. These processes involve small energy transfers that can excite one or both of the incoming protons and create a diffractive system preserving their respective quantum numbers. This diffractive system decays into multi-particle final states where the few produced hadrons are clustered in phase space and typically have low transverse momenta.

As illustrated in Figure 1.2, a system where only one incident proton dissociates is called single-diffractive (SD) and produces particles on one side of the collision. For a double-diffractive (DD) event, both protons are excited and there is a rapidity gap between the two resulting sprays of particles. In a central-diffractive (CD) collision both interacting protons remain intact with new particles emerging at mid-rapidity. Collider experiments typically measure particle production transverse to the beam around mid-rapidity and are therefore not very sensitive to diffractive scattering. Yet, diffractive processes constitute a large fraction of the total inelastic cross-section. Therefore, measurements of particle production rates for inelastic collisions require some extrapolation into unseen phase space and a regime of theoretically not well-understood physical processes. This brings about large normalization uncertainties.

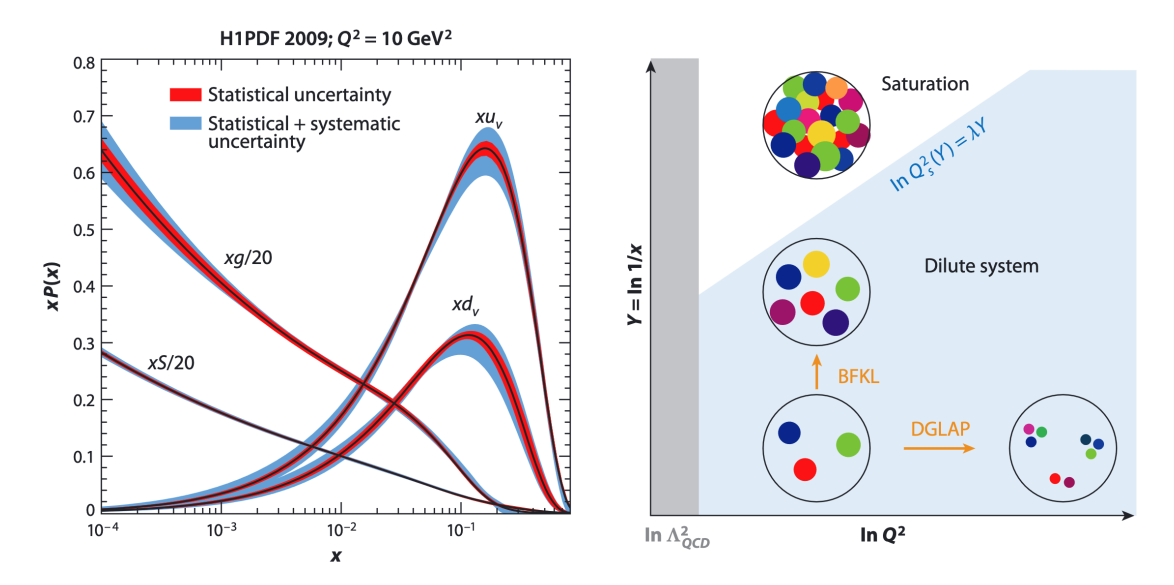


Figure 1.3: Exemplary parton distribution functions (left) and an illustration of gluon saturation in the $\ln(Q^2)$ - $\ln(1/x)$ plane (right) [9].

To mitigate this effect, experimental results are often reported for non-single diffractive (NSD) collisions, a more accessible class of events that can be detected with two-armed coincidence triggers at forward rapidities.

Initial state In a high-energy collider, protons are accelerated to relativistic velocities and, therefore, Lorentz contracted in the lab frame. Within the protons, each parton carries a fraction of the total momentum. The probability density for finding an (anti-)quark or gluon with momentum fraction x, is called the parton distribution function (PDF). The PDF can be inferred from deep-inelastic scattering (DIS) experiments. In these experiments the partonic structure of the proton is measured with a probe particle at a resolution scale Q^2 , venturing to lower $x = (Q/\sqrt{s})^2$ [10] by increasing the center-of-mass energy of the system. The scale dependence of the parton distribution functions is calculable in QCD perturbation theory and can be described by the Dokshitzer-Gribov-Lipatov-Altarelli-Parisi (DGLAP) equations, while their x dependence is represented by the Balitsky-Fadin-Kuraev-Lipatov (BFKL) equations. Based on parametrizations of a wide range of experimental data, these evolution equations allow predicting the PDFs for unmeasured Q^2 and thus enable event generators like PYTHIA to determine the initial momenta of the scattering partons when simulating a collision.

The left panel of Figure 1.3 shows an example set of PDFs in a proton probed at the scale $Q^2 = 10 \,\text{GeV}^2$. While most of the momentum is carried by the up and down valence quarks, at small momentum fractions x the proton is dominated by dynamically produced sea quarks and gluons. The larger the resolution scale Q^2 , the more of those low-x partons are found within the proton, which is a result of parton splitting. In the right panel of Figure 1.3, the structure of a proton is illustrated in the $\ln(Q^2)$ - $\ln(1/x)$ plane. At a fixed x, the number of observed partons increases with increasing Q^2 (DGLAP evolution). As a result of the uncertainty relation, the transverse momentum component $k_{\rm T}$ of the partons within the proton gives them a transverse extent which a probe can only resolve if $k_T^2 \leq Q^2$ [11]. Therefore, the average transverse size of the found partons decreases when the probing scale is increased, making the system more dilute. On the other hand, with increasing energy 1/x at fixed Q^2 the number of partons also rises due to long-lived fluctuations and many gluon splittings (BFKL evolution), but the average transverse size of the partons stays the same. The gluon population increases potentially up to a saturation point, where the gluons start to overlap and recombine. Gluon splitting and gluon recombination are assumed to be in balance at the saturation scale $Q_{\rm S}(x)$ which corresponds to the typical gluon transverse momentum [9] and increases with energy. In this saturated highenergy regime of QCD, the concept of individual partons is no longer meaningful and, instead, the system could be viewed as a condensed medium [11], the so-called Color Glass Condensate (CGC). The measurements presented in this work are compared to theoretical predictions based on the assumption of CGC initial conditions.

Evolution Modeling the whole evolution of a collision from the initial parton interactions towards the measurable final-state hadrons poses a theoretical challenge. Particle production is most accessible at high- $p_{\rm T}$, where hard and soft QCD effects can be separated and thus the cross-section for hadron production factorizes [12]. For both incoming protons, the initial momenta of the colliding partons are inferred from the PDFs. Since particles with high transverse momenta originate from hard initial parton-parton scatterings for which the coupling strength is small, the corresponding partonic cross-sections are calculable using pQCD. A highly energetic parton then initiates a collimated spray of hadrons denoted as a jet. The probability for the parton to produce a specific hadron carrying a fraction of the partons' initial momentum can

be determined experimentally and is encoded in the so-called fragmentation function. This factorization approach has proven successful in theoretically predicting high- $p_{\rm T}$ particle production rates.

While the hard parton scatterings are rare processes, soft QCD interactions govern the production of most particles emerging from a high-energy collision. MC event generators like PYTHIA aim to model the full range of energy scales accessible to experiments by implementing the evolution of a collision from the initial parton interactions towards the measurable multi-particle final state. In addition to the cross-sections of hard parton scatterings that can be rigorously derived from QCD, major parts of a PYTHIA simulation rely on phenomenological modeling of different aspects of the collision. Those model components contain $\mathcal{O}(100)$ [4] parameters which are inferred from comparisons to experimental data. A set of optimized parameter values is denoted as a PYTHIA tune. This work mainly relies on the so-called Monash 2013 [13] tune, which is optimized to describe pp collisions at $\sqrt{s} = 7 \,\text{TeV}$. The observables presented in this thesis are among the ones considered in the tuning process and hence the precise and comprehensive set of measurements resulting from this work could potentially provide important input to future model tuning efforts.

Figure 1.4 illustrates the evolution of a PYTHIA simulation, which typically begins with a hard parton-parton scattering ($d\sigma_0$), where the initial momenta of the partons are inferred from the corresponding PDFs. This scattering constitutes the hardest subprocess of the simulation and with increasing radial distance to the center of Figure 1.4, the hardness scale of the shown subprocesses decreases. The incoming and outgoing partons can radiate gluons and initiate parton showers. This initial and final state radiation is indicated in blue and red, respectively. Softer parton scatterings, so-called multiparton interactions (MPIs), can occur in parallel to the initial hard scattering. While the latter typically initiates a high-momentum jet, the remaining particles originating from the MPIs and beam-remnant interactions are referred to as the underlying event [14] of the collision. The so-called color reconnection (CR) mechanism allows the partons of the different initial scatterings to combine, which results in a redistribution of the available energy in favor of producing fewer particles but with larger momenta. When partons emerge from the collision, they hadronize into color-neutral particles, a process that is implemented in PYTHIA via the so-

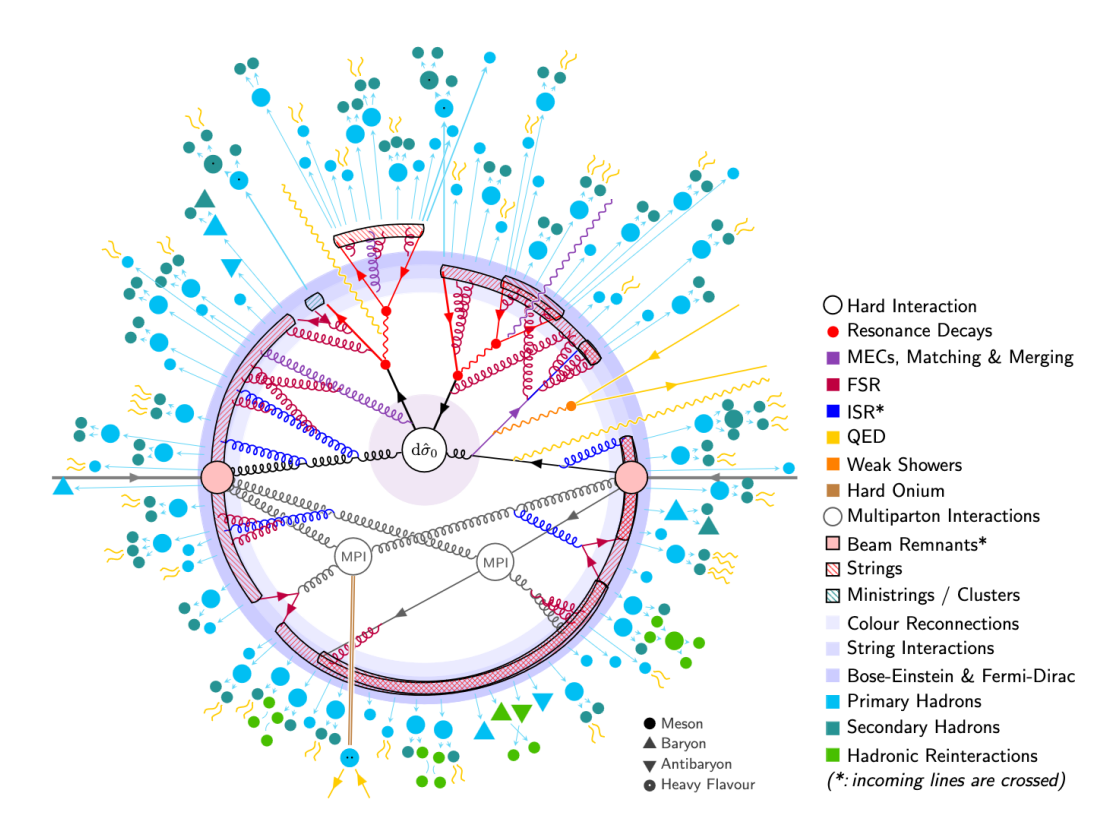


Figure 1.4: Illustration of a pp collision in PYTHIA [4].

called Lund string fragmentation model [15]. Since the potential energy between a color-connected quark-antiquark pair moving apart at some point grows linearly with the separation distance, it becomes energetically more favorable for the connecting color string to break and create a new quark-antiquark or diquark-antidiquark pair. As long as the energy stored in the string is large enough, this fragmentation continues and eventually results in final-state mesons and baryons, respectively. The emerging hadrons can then further decay and rescatter with one another before they arrive in a detector.

1.2.2 Heavy-ion collisions

By colliding heavy nuclei instead of single hadrons, a medium of quasi-free quarks and gluons, the QGP, can form at sufficiently high energy densities. While pp collisions are differentiated by their event types, in the collisions of two extended nuclei, their overlap area is most relevant for the collision outcome. The following paragraphs briefly describe the characteristics and the different stages of a heavy-ion collision.

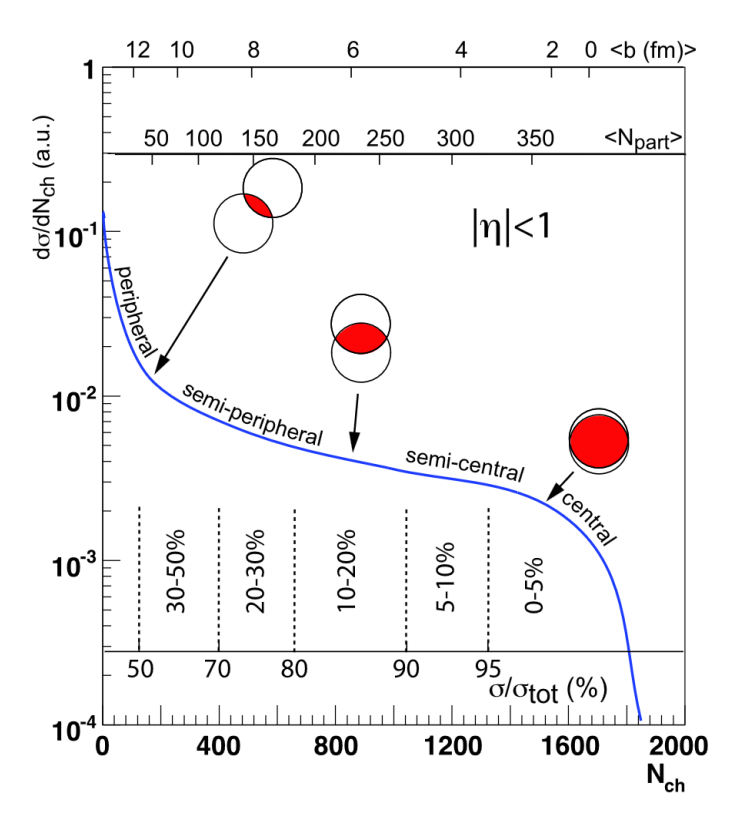


Figure 1.5: Schematic multiplicity distribution in heavy-ion collisions illustrating the different centrality intervals [16].

Centrality To characterize the transverse size of the collision volume, the overlap area of the two nuclei is quantified by an impact parameter b, defined as the transverse distance between the centers of the two heavy ions. Experimentally, the impact parameter b, is not directly measurable. Since the number of particles produced in a collision is related to the overlap area of the colliding nuclei, the centrality of a collision can be approximated via the measured event activity. Figure 1.5 schematically shows the abundance of events as a function of their charged-particle multiplicity $N_{\rm ch}$. The selection of events in percentiles of this distribution is referred to as a centrality selection. Depending on their centrality, collisions are referred to as peripheral, semi-peripheral, semi-central or central. By employing a so-called Glauber MC simulation [16], the centrality intervals can be related to initial state observables such as the average number of colliding nuclei $(\langle N_{\text{part}} \rangle)$, the average number of binary collisions $(\langle N_{\text{coll}} \rangle)$ and the impact parameter (b) of the collision. As expected, collisions with a small impact parameter – corresponding to a large transverse overlap area and a high number of participating nucleons – produce the most particles. Since all participating nuclei

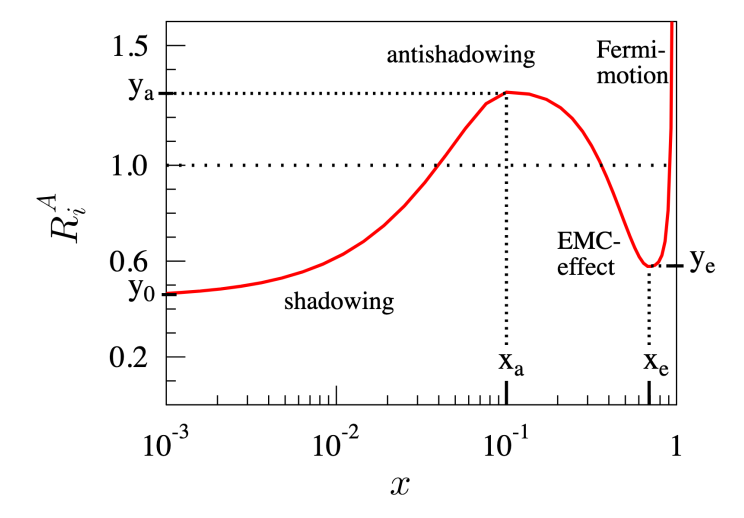


Figure 1.6: Illustration of the nuclear modification of the free proton PDF as a function of x [17].

deposit energy in the collision, the highest energy density and largest volume of the QGP is expected in the most central collisions. Selecting in centrality, therefore, allows relating measured signals in the detector to geometrical quantities of the Glauber model that can not be directly observed. Both the number $N_{\rm part}$ of participants and the impact parameter b characterize the initial state of the heavy-ion collision.

Initial state As previously discussed, the relevant degrees of freedom in high-energy collisions are not the nucleons themselves but the constituting quarks and gluons. For nucleons bound in a nucleus, the distribution of longitudinal momentum fractions x carried by a parton is modified with respect to the free proton. This relative nuclear modification $R_i^A = \text{PDF}_i^{\text{nucl.}}/\text{PDF}_i^{\text{free}}$ of the parton distribution functions is shown schematically in Figure 1.6. At small x, the nuclear PDF (nPDF) is suppressed compared to the free proton PDF as a result of shadowing. The suppression reverses to an enhancement due to anti-shadowing around $x \approx 0.1$, followed by another depletion due to the EMC effect. At x close to unity an excess resulting from the Fermi motion of the nucleons in the nucleus is observed. A quantitative description of the parton distributions in the bound nucleon as a function of x and Q^2 is achieved by a global parametrization of available experimental data. Multiple sets of nPDFs exist that differ in the included measurements, the functional shape used for their parametrization, and the underlying proton PDFs [18]. The nuclear modification of the PDFs showcases that the initial state of a heavy-ion collision is more complex than an overlap of single

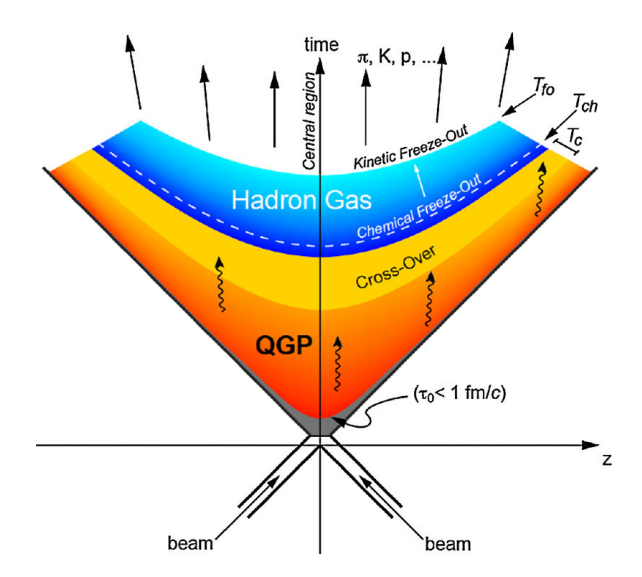


Figure 1.7: Space-time evolution of a central heavy-ion collision [19].

independent hadronic collisions.

Evolution In contrast to pp collisions, the high parton density in a central heavy-ion collision can lead to the formation of a hot and dense state of matter, the QGP. Figure 1.7 illustrates the space-time evolution of such a collision. After a short formation time $\tau_0 < 1 \, \mathrm{fm/}c$, the matter in the collision zone is in equilibrium. In this thermalized QGP, partons from initial hard scatterings can lose energy through collisions with the partons of the medium and medium-induced gluon radiation.

Due to internal pressure, the QGP expands and cools down. This can be described by hydrodynamic calculations, which are for example implemented in the EPOS event generator [20, 21]. The collective expansion of the system boosts the velocities of the produced particles, leading to a stronger push towards higher momenta for heavier particles, a phenomenon known as radial flow. Spacial anisotropies in the initial state result in momentum anisotropies of the emitted particles.

When the system reaches the critical temperature $T_{\rm C}$, the partonic degrees of freedom combine to form hadrons. At the high collision energies considered in this work, this phase transition is regarded as a smooth crossover. After further cooling, a process known as chemical freeze-out occurs at the temperature $T_{\rm chem}$ and hadrons cease to interact inelastically. The particle yields are fixed and the abundances of the different produced particle types are well described by thermal statistical models. At this stage of the collision hadrons can scatter elastically, affecting the momenta of the final-state

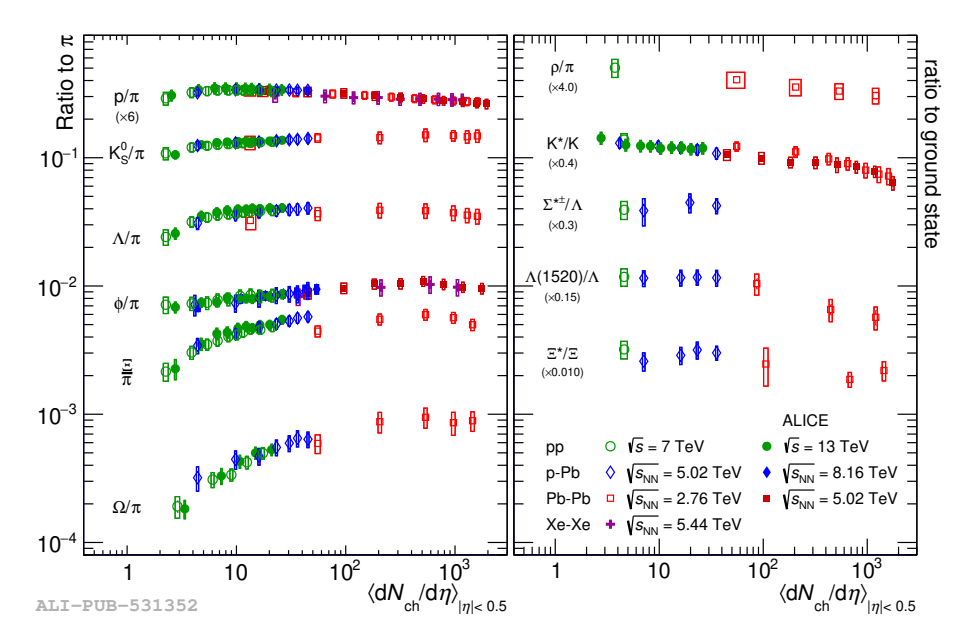


Figure 1.8: Particle abundances relative to pions (left) and particle ratios for resonances to their respective ground state (right) for multiple collision systems and energies as a function of multiplicity [22].

particles. Additionally, resonance states can form and decay, altering the particle yield. This process continues until the kinetic freeze out temperature $T_{\rm fo}$ is reached. The emerging particles can then be measured by detectors.

The left panel of Figure 1.8 shows the ratios of selected particle yields to the pion yield as a function of multiplicity. The figure combines measurements of different collision systems and energies, showing that the hadron chemistry evolves smoothly as a function of multiplicity. The relative contribution of particles with strangeness increases with multiplicity, an effect that scales with the strangeness content of the respective particle. The right panel of Figure 1.8 shows the particle ratios of selected resonance yields to their respective ground state as a function of multiplicity for different collision systems. Again a smooth transition in multiplicity is observed. The suppression of short-lived resonances in heavy-ion collisions is likely caused by rescattering of the resonance state in the hadronic phase.

These two observations highlight that the final-state charged-particle multiplicity, rather than the collision system or energy, is a key observable for characterizing particle production.

1.3 Observables

As previously discussed, the theoretical description of a high-energy collision depends on the correct modeling of soft QCD phenomena. To test and improve different model approaches, precise measurements of the collision's final state are crucial. This thesis focuses solely on electrically charged particles and presents the corresponding charged-particle multiplicity distribution as well as the multiplicity-dependent transverse-momentum spectra. These fundamental observables characterize how the energy available in a collision is distributed into the creation and kinetic energy of the emerging particles. To further investigate the center-of-mass energy and system-size dependence of charged-particle production, these observables are measured in ten different collision scenarios.

In the following, the results of this thesis are contextualized by discussing previous measurements of multiplicity distributions, transverse-momentum spectra, and the average transverse momentum as a function of multiplicity.

1.3.1 Multiplicity distributions

The most fundamental observable for characterizing multi-particle production is the multiplicity distribution, which represents the probability for producing a given number of particles in a collision. The left panel of Figure 1.9 shows previous measurements of charged-particle multiplicity distributions $P(N_{\rm ch})$ in NSD pp and pp̄ collisions within a center-of-mass energy range of $30.4\,{\rm GeV} \le \sqrt{s} \le 1.8\,{\rm TeV}$, where the number of charged particles is determined for the full phase space. In the majority of the collisions only a few charged particles are produced, while higher multiplicities are less likely to occur. However, with rising collision energy the probability for high-multiplicity events increases.

One way to study common features between the multiplicity distributions at different energies, was proposed by Koba, Nielsen, and Olesen (KNO) [25] in 1972. They derived for asymptotically high center-of-mass energies ($\sqrt{s} \to \infty$) that the multiplicity distribution only depends on the shape of an energy-invariant expression $\Psi (N_{\rm ch}/\langle N_{\rm ch} \rangle)$, scaled by the mean multiplicity $\langle N_{\rm ch} \rangle$ in the following way:

$$P(N_{\rm ch}) = \frac{1}{\langle N_{\rm ch} \rangle} \Psi\left(\frac{N_{\rm ch}}{\langle N_{\rm ch} \rangle}\right) + \mathcal{O}\left(\frac{1}{\langle N_{\rm ch} \rangle^2}\right) \quad . \tag{1.2}$$

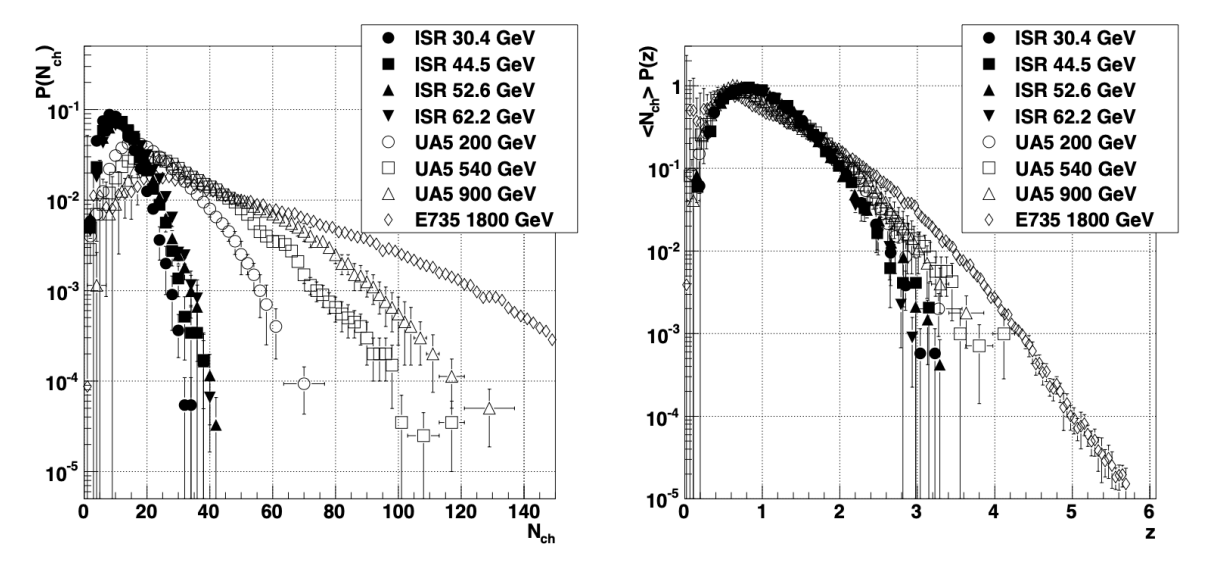


Figure 1.9: Multiplicity distributions of NSD events for the full phase space (left) and their KNO-scaled form (right) [23] with $z = N_{\rm ch}/\langle N_{\rm ch} \rangle$. The nomenclature in this figure differs from the one used in the present work. In this figure $P(z = N_{\rm ch}/\langle N_{\rm ch} \rangle)$ would correspond to $P(N_{\rm ch})$ in the present work.

This implies that the measured multiplicity distributions for different collision energies should approximately align in their so-called KNO-scaling form, where $\langle N_{\rm ch} \rangle P(N_{\rm ch})$ is expressed as a function of relative multiplicity $N_{\rm ch}/\langle N_{\rm ch} \rangle$.

The right panel of Figure 1.9 shows the result of applying this KNO-scaling to the previously discussed multiplicity distributions. For center-of-mass energies within the range $30.4\,\text{GeV} \leq \sqrt{s} \leq 62.3\,\text{TeV}$, the KNO-scaled distributions align well with each other. However, the measurements above $\sqrt{s}=200\,\text{GeV}$ deviate from the common scaling form at high relative multiplicities, as also described in Refs. [26, 27]. When considering INEL events instead of NSD events, a violation of KNO-scaling is observed for the lower energies as well [28].

The magnitude of the scaling violation is reduced for multiplicity distributions of particles produced within the central pseudorapidity range compared to considering the full phase space [27, 29, 30, 24]. This pseudorapidity dependence is illustrated in Figure 1.10, which shows the KNO-scaled charged-particle multiplicity distributions for pp collisions at $\sqrt{s} = 900 \,\text{GeV}$, 2.76 TeV, 7 TeV and 8 TeV in $|\eta| < 0.5$ (top) and $|\eta| < 1$ (bottom). The respective ratios to the $\sqrt{s} = 900 \,\text{GeV}$ reference are shown in the right panels. At high $N_{\text{ch}}/\langle N_{\text{ch}} \rangle$, the KNO-scaled multiplicity distributions differ by up to 250 % from the shape observed in $\sqrt{s} = 900 \,\text{GeV}$ and the deviations are

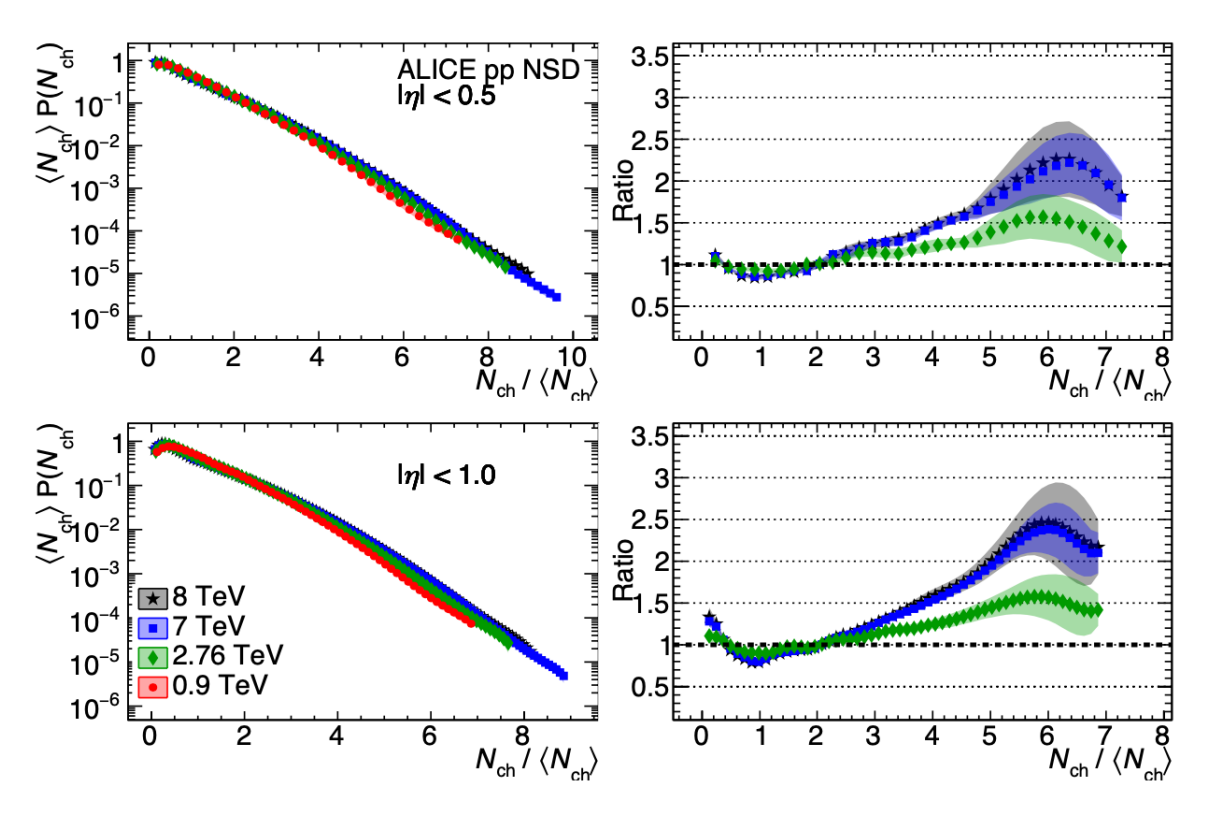


Figure 1.10: KNO-scaled multiplicity distributions of pp collisions at four different energies for $|\eta| < 0.5$ (top) and $|\eta| < 1$ (bottom) together with their ratio to the results at $\sqrt{s} = 900 \,\text{GeV}$ [24].

slightly smaller for the narrower pseudorapidity range $|\eta| < 0.5$.

Although the KNO-scaling apparently brings the measured multiplicity distributions at different collision energies to a more similar form, the level of agreement strongly depends on the considered energy range, the event class and the phase space in which the multiplicity is defined.

Another approach to describe multiplicity distributions is to assume that they follow a negative binomial distribution (NBD):

$$P(N_{\rm ch}) = \frac{\Gamma(N_{\rm ch} + k)}{\Gamma(k)\Gamma(N_{\rm ch} + 1)} \left(\frac{\langle N_{\rm ch} \rangle}{\langle N_{\rm ch} \rangle + k}\right)^{N_{\rm ch}} \left(\frac{k}{k + \langle N_{\rm ch} \rangle}\right)^{k} . \tag{1.3}$$

For $k \to \infty$, this expression coincides with a Poisson distribution, which would be the expected shape for independently emitted particles. Deviations from the Poisson distribution indicate correlations between the produced particles [23]. Experimental measurements show that multiplicity distributions for the full phase space as well as in restricted rapidity ranges are well described by NBDs up to an energy of

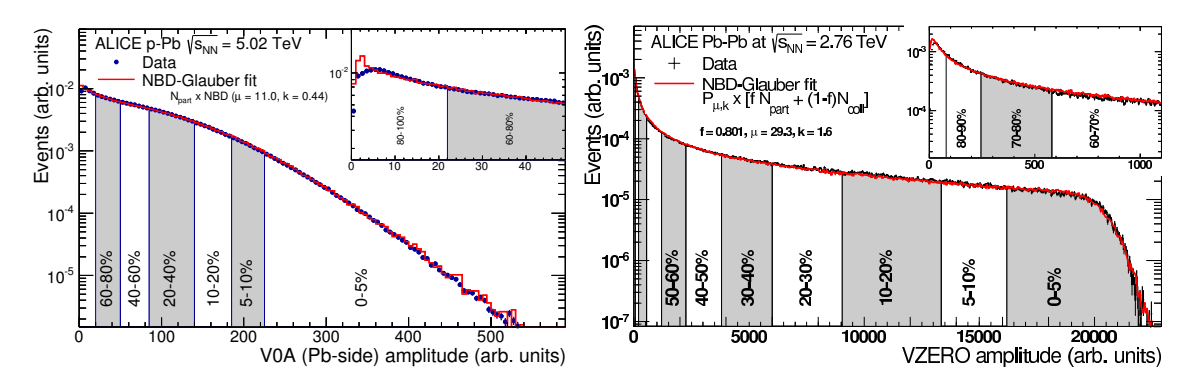


Figure 1.11: Multiplicity distributions for p-Pb (left) [32] and Pb-Pb (right) [33] collisions.

 $\sqrt{s}=540\,\mathrm{GeV}/c$ [27, 31]. For higher collision energies, the NBD is insufficient for parametrizing the multiplicity distributions, except if a very narrow phase space is chosen [27]. These multiplicity distributions are better described by the combination of two NBDs representing a soft and a semi-hard source of particle production [24]. Similarly, the multiplicity distributions of larger collision systems can be parametrized by assuming multiple independent sources that each produce particles according to a NBD. The centrality-dependent number of these particle-emitting sources is constructed using the $N_{\rm part}$ and $N_{\rm coll}$ values from a Glauber MC simulation. In Figure 1.11, the multiplicity distributions are shown for p–Pb and Pb–Pb collisions at $\sqrt{s_{\rm NN}}=5.02\,\mathrm{TeV}$ and 2.76 TeV, respectively. As expected, the shapes and the ranges of the multiplicity distributions differ significantly from the single pp collisions. The red lines indicate NBD-Glauber fits to the corresponding distributions.

The mean multiplicity is used to compare particle production in different collision systems and at different center-of-mass energies. Figure 1.12 shows these mean multiplicities per participating nucleon pair for pp, p—Pb and central AA collisions as a function of the center-of-mass energy per nucleon pair. The mean multiplicities in pp collisions are lower than in heavy-ion collisions with an increasing difference towards higher center-of-mass energies. All mean multiplicities exhibit a power-law dependence with the center-of-mass energy.

1.3.2 Transverse-momentum spectra

The second key observable considered in this thesis is the transverse-momentum spectrum representing the average number of particles per collision that are pro-

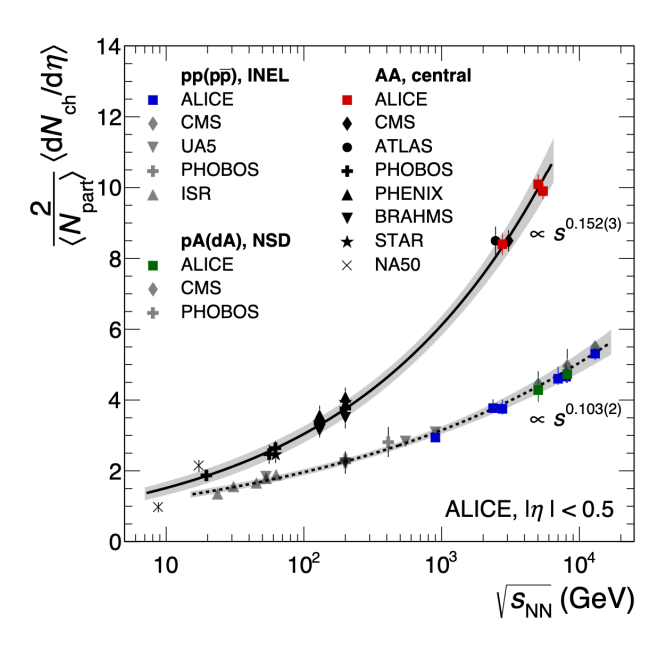


Figure 1.12: Compilation of mean multiplicities measured by different experiments at various center-of-mass energies [22].

duced within a given $p_{\rm T}$ interval. The left panel of Figure 1.13 shows the transverse-momentum spectra of charged particles produced in pp, p–Pb, and centrality-selected Pb–Pb collisions at an energy of $\sqrt{s_{\rm NN}}=5.02\,{\rm TeV}$. The figure illustrates that independent of the collision system most particles are produced with low transverse momenta and the probability for particle production steeply decreases towards higher $p_{\rm T}$. While the shape of the $p_{\rm T}$ spectrum in peripheral Pb–Pb collisions is similar to that of pp and p–Pb collisions, with increasing centrality a noticeable depletion of the particle yield occurs at $p_{\rm T}\gtrsim 5\,{\rm GeV}/c$, which is commonly attributed to parton energy loss in the hot and dense medium.

This effect can be further quantified by means of the nuclear modification factor (R_{AA}) , which compares the particle production in a heavy-ion collision to the corresponding expectation from a mere geometrical superposition of multiple pp collisions at the same energy. The R_{AA} is defined as the ratio of the heavy-ion p_T spectrum at a given centrality to the pp reference spectrum scaled by the mean number of binary collisions according to the Glauber model:

$$R_{\rm AA} = \frac{\mathrm{d}N/\mathrm{d}p_{\rm T}|_{\rm AA}}{\langle N_{\rm coll}\rangle \,\mathrm{d}N/\mathrm{d}p_{\rm T}|_{\rm pp}} \quad . \tag{1.4}$$

Deviations of the R_{AA} from unity indicate that additional phenomena in heavy-ion

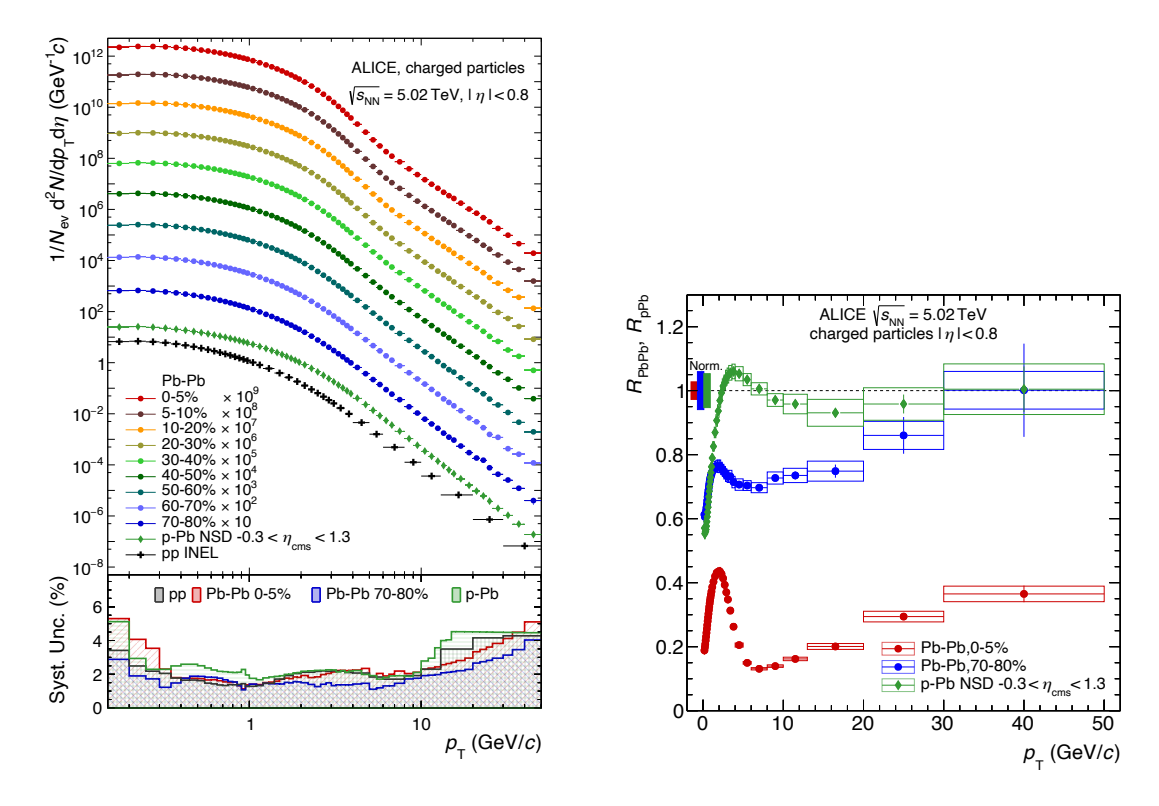


Figure 1.13: Charged-particle transverse-momentum spectra in pp, p–Pb and Pb–Pb collisions at $\sqrt{s_{\rm NN}} = 5.02\,{\rm TeV}$ (left) and the corresponding nuclear modification factors (right) [34].

collisions affect particle production. This includes both cold nuclear matter effects and parton energy loss in the hot and dense QCD matter.

The right panel of Figure 1.13 shows $R_{\rm AA}$ measurements for p-Pb collisions as well as for central and peripheral Pb-Pb collisions, based on the previously discussed $p_{\rm T}$ spectra. The measured $R_{\rm AA}$ in p-Pb collisions is consistent with unity for $p_{\rm T} \gtrsim 8\,{\rm GeV}/c$, suggesting no medium formation. In contrast, the $R_{\rm AA}$ measurement for central Pb-Pb collisions shows a strong suppression of particle production also at high $p_{\rm T}$, which can be interpreted as a result of parton energy loss in the QGP. For peripheral collisions only a moderate suppression and a weak $p_{\rm T}$ dependence is observed.

The average transverse momentum $\langle p_{\rm T} \rangle$ can be used to study the collision-energy dependence of the $p_{\rm T}$ spectra. Since the $p_{\rm T}$ range of experimental measurements is often limited, extrapolations of the spectra are required to determine $\langle p_{\rm T} \rangle$. In the case of pp collisions, two common parametrizations are the Two-Component Model (TCM) [36] and the modified Hagedorn function [37]. Both parametrizations

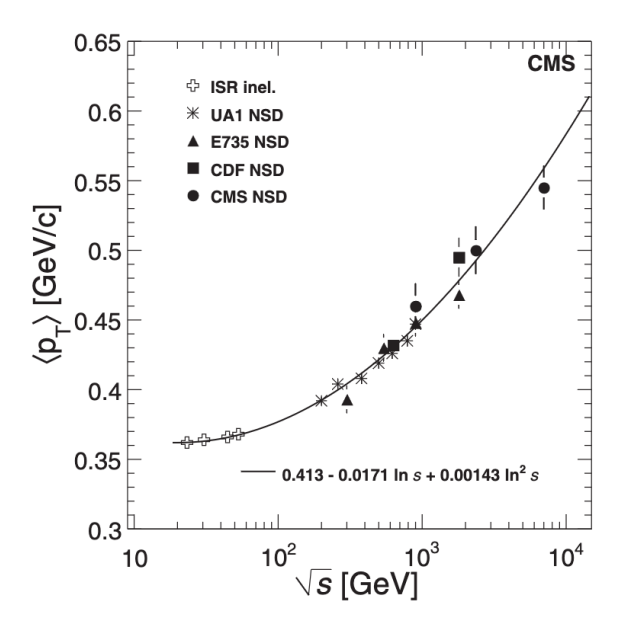


Figure 1.14: Mean transverse momenta for pp and p \bar{p} collisions measured with different experiments at center-of-mass energies within the range $23.3\,\text{GeV} \le \sqrt{s} \le 7\,\text{TeV}$ [35].

describe the low- $p_{\rm T}$ region with an exponential function and the high- $p_{\rm T}$ region with a power law, mirroring the shape of the measured $p_{\rm T}$ spectra.

Various $\langle p_{\rm T} \rangle$ values are shown in Figure 1.14 for pp and p $\bar{\rm p}$ collisions at different center-of-mass energies. The observed rise of $\langle p_{\rm T} \rangle$ with \sqrt{s} probably reflects an increase of particle production originating from hard parton-parton scatterings.

1.3.3 $\langle p_{\rm T} \rangle$ as a function of $N_{\rm ch}$

The main focus of the work presented in this thesis is to measure the correlation between the number of charged particles produced in a collision and their $p_{\rm T}$ distribution. A proxy for this relation, which characterizes the balance of particle creation and kinetic energy, is the mean transverse momentum, $\langle p_{\rm T} \rangle$, as a function of $N_{\rm ch}$. This observable has been studied extensively by previous analyses. In pp and pp̄ collisions these measurements cover centre-of-mass energies from $\sqrt{s} = 31 \,\text{GeV}$ up to 13 TeV (see Refs. [39, 40, 41, 42, 43, 44, 45, 29, 46, 47]) and for larger collision systems, measurements are for example available in p-Pb [38] and Pb-Pb [34] collisions at $\sqrt{s_{\rm NN}} = 5.02 \,\text{TeV}$ and Xe-Xe [48] collisions at $\sqrt{s_{\rm NN}} = 5.44 \,\text{TeV}$. All studies observe an increase of $\langle p_{\rm T} \rangle$ with $N_{\rm ch}$ in the central rapidity region.

In the left panel of Figure 1.15 this increase of $\langle p_{\rm T} \rangle$ with $N_{\rm ch}$ is shown for pp collisions

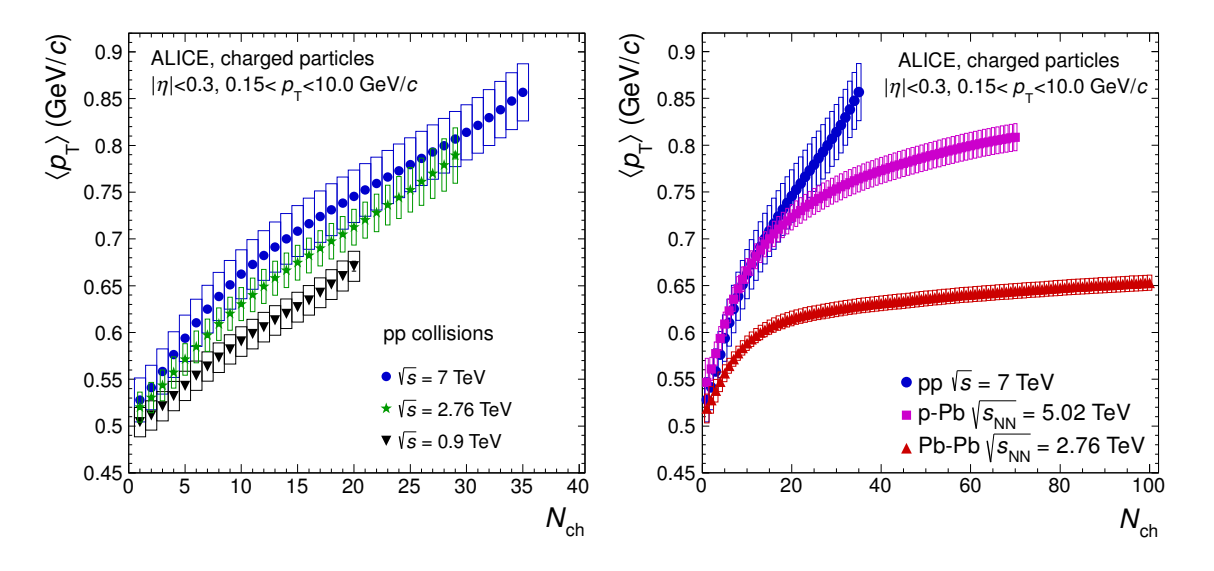


Figure 1.15: Mean transverse momentum of charged particles for pp collisions at three different center-of-mass energies (left) as well as for pp, p–Pb and Pb–Pb collisions (right) [38].

at three different center-of-mass energies. While the $\langle p_{\rm T} \rangle$ is similar for collisions with low multiplicities, an energy ordering becomes apparent with increasing $N_{\rm ch}$. The right panel of Figure 1.15 compares the $\langle p_{\rm T} \rangle - N_{\rm ch}$ correlation for pp, p-Pb and Pb-Pb collisions. Starting from similar values at the lowest multiplicity, the $\langle p_{\rm T} \rangle$ follows distinctly different trends as a function of $N_{\rm ch}$. In p-Pb collisions, $\langle p_{\rm T} \rangle$ first rises steeply with $N_{\rm ch}$, similar to the trend observed for pp collisions, before it deviates and continues with a slower slope. In Pb-Pb collisions, the average transverse momentum of the emerging particles is generally lower than in the other collision systems and also increases significantly slower with multiplicity.

While this measurement already constitutes an extensive characterization of the $\langle p_{\rm T}\rangle$ - $N_{\rm ch}$ correlation for multiple collision scenarios, the present work aims to provide an even more comprehensive dataset covering additional collision systems and energies. Furthermore, the analysis presented in this thesis achieves smaller systematic uncertainties compared to the previous measurement and additionally gives access to higher moments of the multiplicity-dependent $p_{\rm T}$ spectra by employing a new unfolding-based approach.

1.4 Unfolding experimental data

The work presented in this thesis aims to determine the charged-particle multiplicity distribution of collisions in the LHC and their per-event production rate of charged particles as a function of $N_{\rm ch}$ and $p_{\rm T}$. Both observables cannot be measured directly with perfect precision due to limitations of the experimental setup and the employed analysis procedures. In order to still obtain results comparable across different experiments and with theoretical predictions, the raw detector-biased measurements need to be corrected. This subsection discusses a general methodology to extract production rates of collisions or particles as a function of a given property $x_{\rm t}$, which in this work corresponds to either $N_{\rm ch}$, $p_{\rm T}$, or their correlation.

Three different phenomena affect the experimentally measured observables:

- Efficiency The sensitivity for measuring an observable of interest depends on the phase-space acceptance and performance of the detector as well as additional data quality requirements imposed on the detected collision events or charged-particle tracks. In this thesis, the measurement's response to this loss of signal is collectively denoted as efficiency and calculated as a function of x_t .
- Smearing Due to the finite detector resolution, the properties of a reconstructed collision or particle can only be determined with a certain precision. Hence, an actual property x_t will be observed experimentally with a smeared and potentially different property x_m . The corresponding probabilities for misidentification are encoded in the smearing matrix $S(x_m|x_t)$.
- Contamination The measured sample of collisions or particles may contain unwanted background or fake signals even after employing purity selections on the data. In contrast to the efficiency, this contamination is calculated as a function of $x_{\rm m}$ since it is an inherent feature of the measurement process.

Correcting the raw measurement for these three classes of detector effects is commonly referred to as unfolding the experimental data. Figure 1.16 illustrates how the measurement process affects an original distribution $n(x_t)$ to become an experimentally observed distribution $n(x_m)$. The colors indicate the different original properties of the collisions or particles. As suggested in the illustration, usually, the observables are

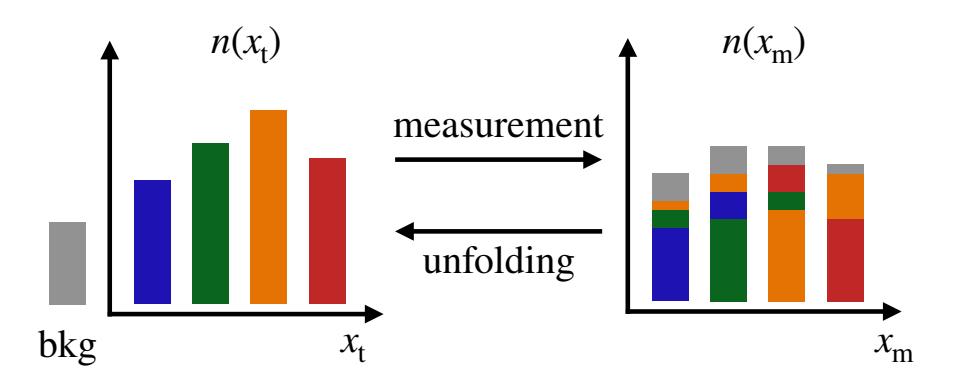


Figure 1.16: Illustration of the unfolding challenge.

accumulated in intervals, so-called bins, which define the maximum precision of the measurement. Due to the efficiency losses, the total yield is reduced in the measured distribution and contributions from various true properties x_t can be smeared into the same x_m interval. In addition, as indicated in gray, background contaminates the measurement. Unfolding the measured distribution $n(x_m)$ aims to undo the effects of efficiency losses, smearing, and contamination in order to obtain the original distribution $n(x_t)$ undistorted by the measurement process. Unfolding corrections require knowledge about the detector's performance, which can be gained through Monte Carlo (MC) simulations. These simulations consist of a physics-inspired model to generate artificial collisions and an ensuing virtual representation of the detector through which the simulated particles are propagated. Since the true $n_{\rm MC}(x_t)$ and measured $n_{\rm MC}(x_{\rm m})$ distributions are known in the simulation, the most straightforward approach for solving the unfolding problem is to calculate a pseudo-efficiency $(\varepsilon_{\rm pseudo} = n_{\rm MC}(x_{\rm m})/n_{\rm MC}(x_{\rm t}))$ and use it to correct the measurement:

$$n(x_{\rm t}) = n(x_{\rm m}) \cdot \frac{n_{\rm MC}(x_{\rm t})}{n_{\rm MC}(x_{\rm m})} \quad . \tag{1.5}$$

Historically, this so-called bin-by-bin unfolding or correction factor method [49] was widely used in high-energy physics. Usually, the background contamination (inferred from the MC simulation) is subtracted from both measured distributions $(n(x_{\rm m})$ and $n_{\rm MC}(x_{\rm m}))$ prior to applying this correction. The bin-by-bin unfolding method implicitly assumes equivalent intervals in $x_{\rm t}$ and $x_{\rm m}$ and simultaneously corrects both for efficiency and smearing, resulting in pseudo-efficiencies that can potentially be larger than unity. If the effect of smearing is significant, the correction becomes highly

sensitive to the accuracy of the underlying true distributions provided by the MC event generator, since relative differences in the yield of neighboring intervals contributing to a measured $x_{\rm m}$ bin also affect the resulting pseudo-efficiency. Due to this strong model dependence, the correction factor method is not suited for high-precision measurements of observables significantly prone to detector smearing. Thus, several other approaches to the unfolding challenge in high-energy physics have emerged [50, 51, 52, 53] with current research focusing on machine-learning-based techniques [54, 55, 56].

In general, a trustworthy correction procedure should allow for imperfections of the distributions produced by the MC event generator and solely rely on the assumption that the performance of the detector is well represented in the simulation. Any binned representation of the detector response has an intrinsic event-generator dependence in case the underlying true distributions within the chosen intervals are not well reproduced. Therefore, a fine granularity of the detector response is preferable if permitted by the available MC statistics. The event-generator bias in the detector response can furthermore be reduced by defining the truth baseline for the unfolding corrections as close as possible to the experimentally accessible region of phase space and thus avoid extrapolating the data purely based on the MC simulation.

Technically, the measured distribution $n(x_{\rm m})$ is the result of folding the true distribution $n(x_{\rm t})$ with the response $P(x_{\rm m}|x_{\rm t})$ of the detector:

$$n(x_{\rm m}) = \sum_{\rm t} P(x_{\rm m}|x_{\rm t}) \ n(x_{\rm t}) \quad .$$
 (1.6)

As illustrated in Figure 1.16, the background can be treated as an additional, virtual source of yield contributing to the measurement and is, therefore, included in the sum. The detector response is represented by the conditional probability $P(x_{\rm m}|x_{\rm t})$ for measuring a collision or particle with property $x_{\rm t}$ and detecting it with property $x_{\rm m}$. It is a product of the efficiency $\varepsilon(x_{\rm t})$ and the bin-migration probability represented by the smearing-matrix $S(x_{\rm m}|x_{\rm t})$. By definition, the elements of the response matrix, therefore, fulfill the following normalization condition for each true property $x_{\rm t}$:

$$\sum_{\mathbf{m}} P(x_{\mathbf{m}}|x_{\mathbf{t}}) = \varepsilon(x_{\mathbf{t}}) \quad . \tag{1.7}$$

To unfold the measured distribution and obtain $n(x_t)$, the composition of the measurement $n(x_{\rm m})$ with respect to the various true properties $x_{\rm t}$ must be known. This composition is represented by the un-smearing matrix $P(x_t|x_m)$, which contains the conditional probabilities that the yield measured with some property $x_{\rm m}$ originally had property x_t . In principle, $P(x_t|x_m)$ could be directly obtained from the MC simulation analogously to the detector response $P(x_{\rm m}|x_{\rm t})$. In this case, however, $P(x_{\rm t}|x_{\rm m})$ would be biased by the shape of the distribution $n_{\rm MC}(x_{\rm t})$ produced by the underlying event generator (see Ref. [57] for an illustrative example). The detector response $P(x_{\rm m}|x_{\rm t})$ in contrast, mainly depends on the accuracy of the virtual detector model. Therefore, in the present work, $P(x_t|x_m)$ is constructed by inverting the conditional probabilities $P(x_{\rm m}|x_{\rm t})$ of the response matrix. This is done by iteratively applying Bayes' theorem [58] to gradually modify an initial guess for the true distribution such that folding it with the detector response results in the measured distribution. This procedure was presented by G. D'Agostini in Ref. [50] and is often referred to as Iterative Bayesian Unfolding (IBU). Other common names are D'Agostini iteration method, expectation-maximization iteration with early stopping [59], or Richardson-Lucy (R-L) method [60, 61] after its original authors in the fields of optics and astronomy. The IBU procedure is described in the following, complemented by an illustrative summary of the involved equations shown in Figure 1.17. This work uses an implementation of the IBU algorithm in the RooUnfold [62] software package.

Iterative Bayesian Unfolding Suppose $P(x_t)$ and $P(x_m)$ are the probability distributions for the occurrence of the true and measured properties, respectively, and the probability for a certain (x_t, x_m) -pair is given by $P(x_t \cap x_m)$. Then, the corresponding conditional probabilities are defined as:

$$P(x_{\rm m}|x_{\rm t}) = \frac{P(x_{\rm t} \cap x_{\rm m})}{P(x_{\rm t})}$$
 and $P(x_{\rm t}|x_{\rm m}) = \frac{P(x_{\rm t} \cap x_{\rm m})}{P(x_{\rm m})}$ (1.8)

Combining the two expressions results in Bayes' theorem:

$$P(x_{t}|x_{m}) = \frac{P(x_{m}|x_{t}) P(x_{t})}{P(x_{m})} .$$
 (1.9)

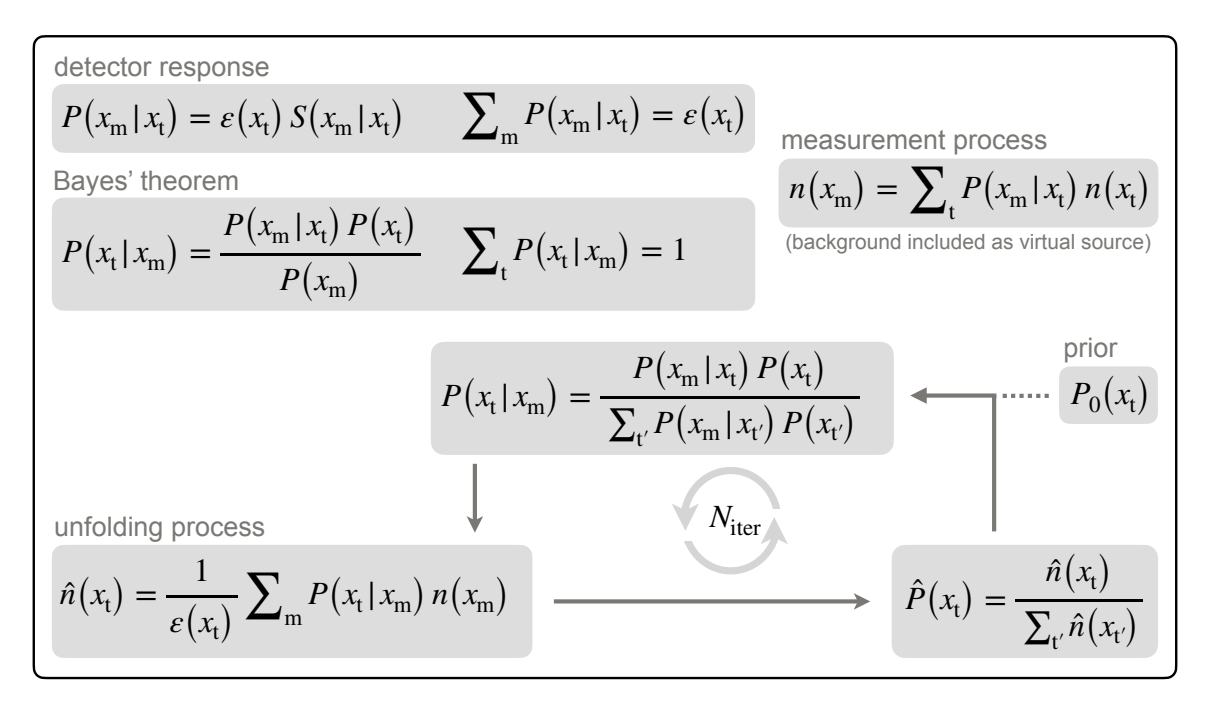


Figure 1.17: Summary of the IBU procedure.

In analogy to Equation (1.6), the total probability of detecting a collision or particle with a property $x_{\rm m}$ can be constructed by folding the true distribution with the detector response:

$$P(x_{\rm m}) = \sum_{\rm t} P(x_{\rm t} \cap x_{\rm m}) = \sum_{\rm t} P(x_{\rm m}|x_{\rm t}) \ P(x_{\rm t}) \quad . \tag{1.10}$$

Therefore, the un-smearing matrix can be expressed independently of the measured probability distribution:

$$P(x_{t}|x_{m}) = \frac{P(x_{m}|x_{t}) P(x_{t})}{\sum_{t'} P(x_{m}|x_{t'}) P(x_{t'})} .$$
 (1.11)

For a fixed $x_{\rm m}$ the sum of these conditional probabilities over all true properties $x_{\rm t}$ is normalized to unity since all measured yield must originate from a true source (or the virtual background):

$$\sum_{t} P(x_{t}|x_{m}) = 1 \quad . \tag{1.12}$$

With an arbitrary choice for the prior $P(x_t)$, Equation (1.11) can be used to calculate a first guess for the un-smearing matrix $\hat{P}(x_t|x_m)$ and tentatively unfold the measured

distribution:

$$\hat{n}(x_{\rm t}) = \frac{1}{\varepsilon(x_{\rm t})} \sum_{\rm m} \hat{P}(x_{\rm t}|x_{\rm m}) \ n(x_{\rm m}) \quad . \tag{1.13}$$

Commonly the MC truth distribution is used as the prior for the unfolding. It is important to note that if the initial guess for $P(x_t)$ is zero for some x_t -interval, the procedure is by construction unable to recover the yield corresponding to this property. The preliminary unfolded distribution directly allows inferring an updated estimate for $P(x_t)$:

$$\hat{P}(x_{t}) = \frac{\hat{n}(x_{t})}{\sum_{t'} \hat{n}(x_{t'})} \quad . \tag{1.14}$$

The measured distribution $n(x_{\rm m})$, which is a direct effect of the unknown underlying distribution $P(x_t)$, contributes to Equation (1.13) and thereby indirectly constrains the estimate $\hat{P}(x_t)$. Therefore, this estimated probability distribution is closer to the actual $P(x_t)$ than the arbitrary initial guess. Using $\hat{P}(x_t)$ as a better guess in Equation (1.11) and starting the procedure over again results in an even more accurate $\hat{P}(x_t)$. This suggests repeating the process several times. The more $\hat{P}(x_t)$ is compatible with the measurement, the less it changes from iteration to iteration. This decreasing difference of $\hat{P}(x_t)$ between consecutive iterations is, therefore, used as an indicator for convergence. Since the statistical uncertainty of the measured distribution $n(x_{\rm m})$ contributes to $\hat{P}(x_{\rm t})$ in each repetition, the number of iterations should be restricted. A detailed calculation of the corresponding propagation of uncertainties can be found in Ref. [62]. As a result of smearing, the uncertainties of the unfolded data points can be strongly correlated. In addition to increasing the statistical uncertainties, too many iterations can result in unstable, oscillating solutions that do not properly represent the underlying probability distribution. This is a result of so-called overfitting, which occurs when the unfolding procedure unsuccessfully tries to find a true distribution that reproduces statistical fluctuations of the measurement. Therefore, the number N_{iter} of iterations serves as a regularization parameter of the unfolding procedure and must be chosen such that this overfitting is avoided or at least minimized without biasing the results towards the prior. In the present work, the unfolding is stopped automatically after a minimum of three iterations once the χ^2 per degree of freedom between the unfolding results of two consecutive steps falls below unity.

Not only the measured distribution is prone to statistical fluctuations, but also the detector response extracted from the MC simulation can suffer from insufficient statistics and, therefore, not properly represent the corresponding probabilities. This will result in a systematic bias of the unfolded results that cannot be mitigated. Therefore, the dimensionality and interval widths for x_t and x_m need to be chosen such that the detector response is sufficiently populated with the available MC statistics. Commonly, the x_t distributions in high-energy physics are of a steeply falling nature and, thus, also the statistics of the simulated data decreases towards higher values of x_t , limiting the range in which the unfolding corrections are reliable.

The IBU method forms the basis of all corrections employed in this work and is directly used to obtain the multiplicity distribution of collisions as a function of $N_{\rm ch}$. Correcting the charged-particle production rate as a function of $p_{\rm T}$ and $N_{\rm ch}$ with the intended high granularity would, however, require an unreasonably large amount of MC statistics to populate the corresponding detector response. Therefore, a novel sequential unfolding approach is developed in the scope of this work to effectively achieve this 2D unfolding. The details of this procedure are discussed in Section 3.

2 Experiment and data preparation

The measurement presented in this thesis is based on particle collisions at the Large Hadron Collider (LHC) recorded with the ALICE experiment at the European Organization for Nuclear Research (CERN), near Geneva in the French-Swiss border region. The ALICE collaboration maintains the detectors and ensures the data calibration, reconstruction, and quality, providing the foundation for this analysis.

This section gives an overview of the LHC and a description of the experimental setup of ALICE, focusing on the detectors relevant to this work. Furthermore, selected aspects of the central preprocessing of the raw detector data are discussed. Then, a brief description of the centrally produced MC simulations, complementing the experimental data, is given.

2.1 The Large Hadron Collider

CERN operates the current world's largest and most powerful particle accelerator, the LHC, which resides in a tunnel of 27-kilometer circumference. Within two beam pipes, ions are accelerated in an ultrahigh vacuum by the electric fields of radiofrequency (RF) cavities in two opposite directions. Strong superconducting dipole magnets bend the particles on their circular paths, and quadrupole magnets serve as lenses to focus the beam. In the LHC, protons and heavy ions are accelerated to velocities close to the speed of light and brought to collision at four designated interaction points, where the four large-scale experiments ATLAS, ALICE, CMS and LHCb are located. In order to acquire sufficiently large kinetic energy for injection into the LHC, the ions travel through a chain of pre-accelerators schematically depicted in Figure 2.1. Hydrogen or heavier elements are stripped of their electrons before taking different paths to the Proton Synchrotron (PS) and then entering the Super Proton Synchrotron (SPS). Protons are injected into the LHC with a kinetic energy of 450 GeV and could then technically be accelerated up to the LHC design energy of 7 TeV [63]. Compared to the proton energy for the same LHC setup, the corresponding kinetic energy of heavy ions scales with their respective charge-to-mass ratio.

During the operational periods relevant to this work, LHC Run 1 (2009 - 2013) and Run 2 (2015 - 2018), pp, p-Pb, Xe-Xe, and Pb-Pb have been brought to collision in

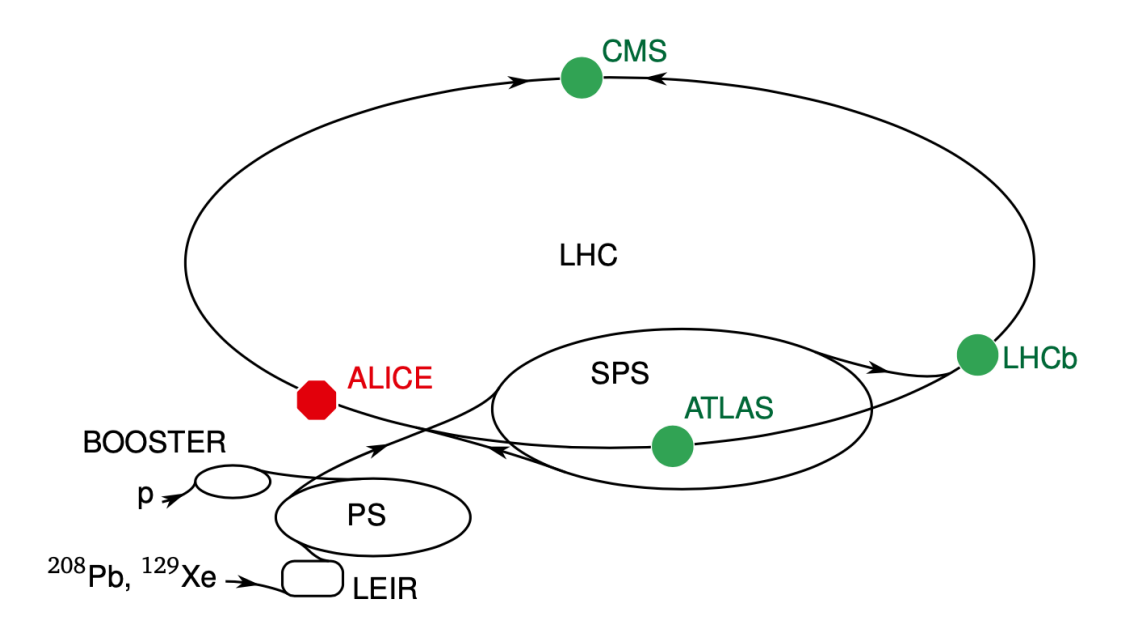


Figure 2.1: Illustration of the LHC accelerator complex [64].

the LHC. In that period, the maximum kinetic energy of protons reached 6.5 TeV, resulting in a center-of-mass energy coverage for pp collisions of $0.9\,\mathrm{TeV} \le \sqrt{s} \le 13\,\mathrm{TeV}$. LHC beams consist of distinct clouds of particles, so-called bunches, that are filled into the accelerator ring and kept circulating until their intensity has decreased significantly due to the collisions. With a certain probability some ions in two crossing bunches collide. The frequency of these collisions, called interaction rate, depends on the bunch-filling scheme as well as the focus and crossing angle of the beams. The four experiments are built around the LHC interaction points to measure the particles emerging from the high-energy collisions of the accelerated ions.

2.2 The ALICE experiment

All data presented in this thesis were collected with ALICE, a general-purpose experiment whose research program focuses on the study of hot and dense nuclear matter. ALICE employs various detector technologies to measure the different particles produced by collisions in the LHC. A distinguishing feature of ALICE compared to the other three LHC experiments is its excellent charged-particle tracking capability at mid-rapidity ($|\eta| < 0.8$) down to low transverse momenta ($p_T > 150 \,\mathrm{MeV}$), even for the high particle densities present in central heavy-ion collisions. This allows for precise studies of soft QCD probes like the observables presented in this thesis.

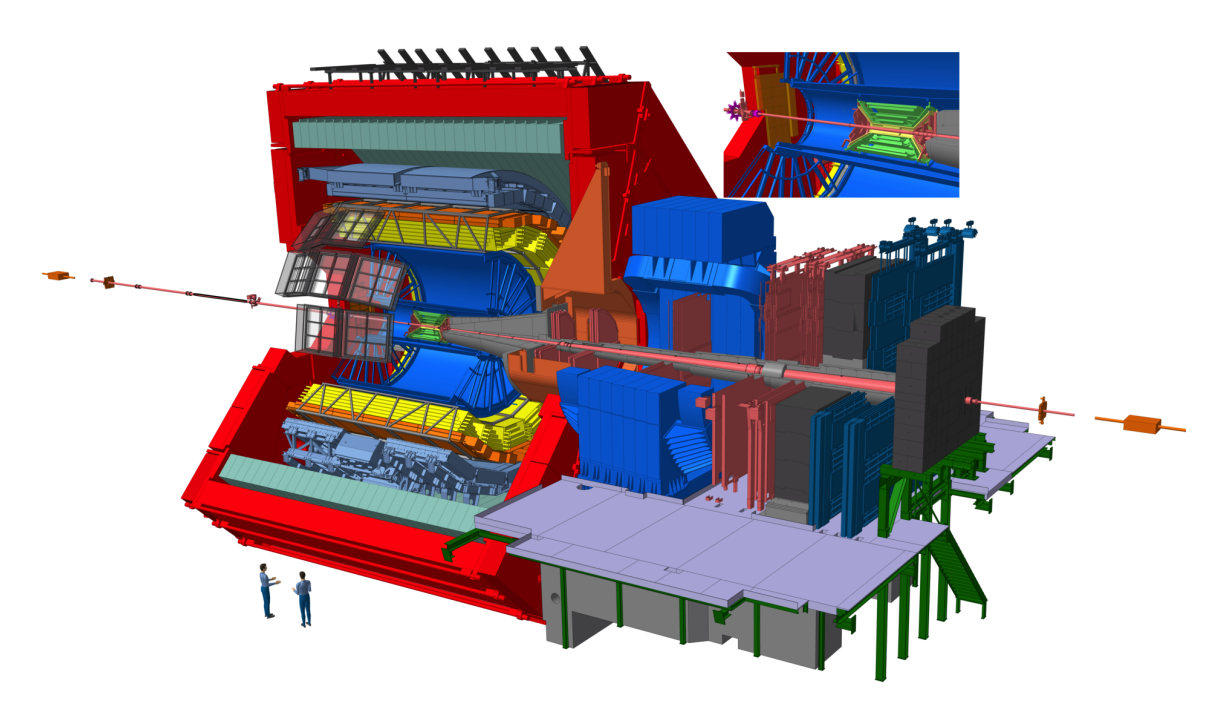


Figure 2.2: Illustration of the ALICE experiment during LHC Run 2 [65].

Figure 2.2 illustrates the general layout of the experiment in its LHC Run 2 setup. A comprehensive description of the different components can be found in Ref. [66]. ALICE's central detector systems are assembled around the interaction point in cylindrical layers and reside within the large L3 solenoid magnet indicated in red in Figure 2.2. Since this thesis focuses on charged-particle production, the following subsections detail the two main tracking detectors of the experiment, namely the Inner Tracking System (ITS) and the Time Projection Chamber (TPC), highlighted in Figure 2.2 in green and blue, respectively. Those detector systems can also be used to distinguish different charged-particle species like pions, kaons, protons or electrons through their specific energy loss in the detector material. The particle identification capability is complemented by the time-of-flight measurements with the TOF detector, indicated in orange, as well as by the electromagnetic calorimeters and the muon system at forward rapidities.

In addition to the two main tracking detectors, this work relies on the V0 system, which is a crucial component for determining whether a collision occurred at the ALICE interaction point. Therefore, the next subsection presents the technical details of this detector system.

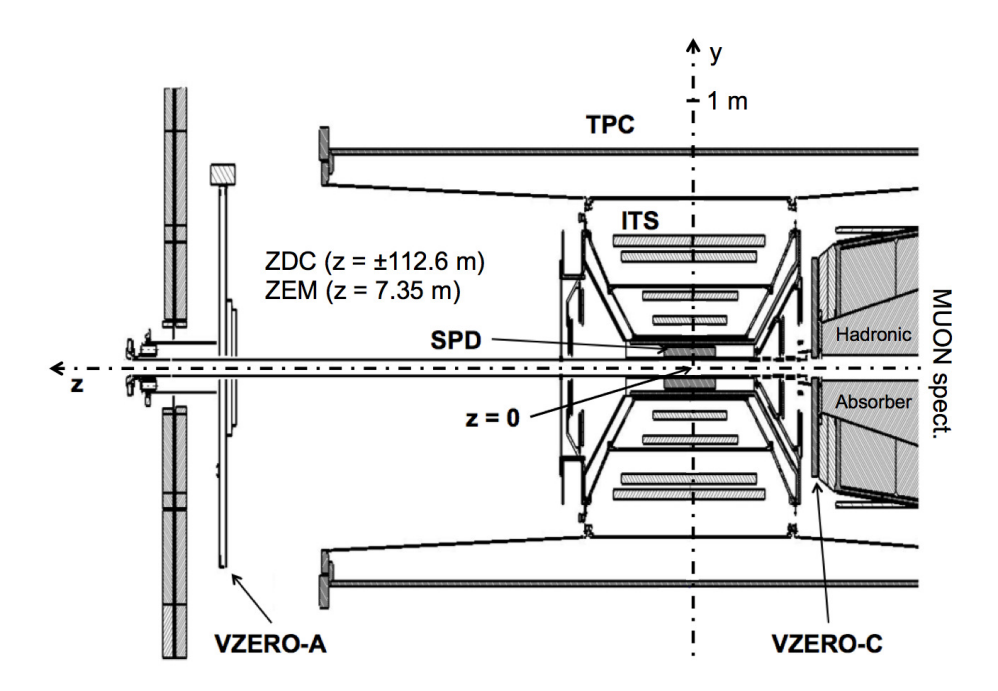


Figure 2.3: Lateral profile of the inner part of the ALICE experiment indicating the position of the V0 (VZERO) systems [67].

2.2.1 V0 detector

The V0 (or VZERO) detector consists of two plastic scintillator arrays (V0A and V0C) installed on the two sides of the interaction point along the beam direction z. It is used to measure particle production at forward rapidities covering $2.8 < \eta < 5.1$ (V0A) and $-3.7 < \eta < -1.7$ (V0C). The position of the V0 detectors within the ALICE experiment is indicated in Figure 2.3. The V0A is located at $z=329\,\mathrm{cm}$ and has a diameter of 82 cm. The V0C detector is positioned closer to the interaction point at $z=-86\,\mathrm{cm}$ due to the spatial constraints from the muon spectrometer on this side of the experiment, and it has a slightly smaller diameter of 64 cm. Both V0 detectors are segmented into four rings in the radial direction, with each ring consisting of eight sectors spanning 45° in azimuth. More technical details and a performance evaluation based on the V0 system's first few years of operation can be found in Ref. [67]. The fast V0 detector is mainly used to trigger the data-taking when inelastic collisions occur in the LHC. By requiring a coincidence of signals in the two V0 discs, non-

single diffractive collisions can be selected. In addition, the event activity at forward

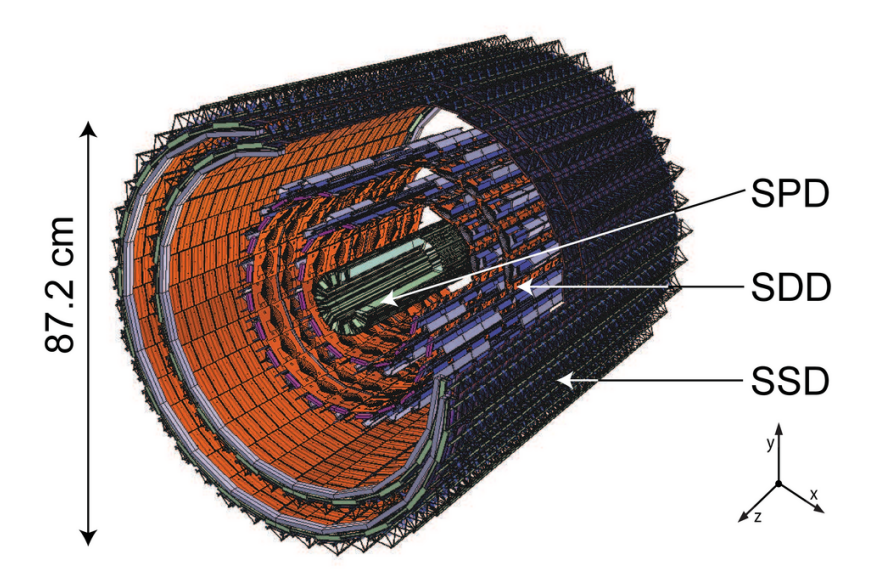


Figure 2.4: Schematic view of the ALICE Inner Tracking System [68].

total signal amplitudes measured in V0A and V0C.

2.2.2 Inner Tracking System

The Inner Tracking System (ITS) consists of six layers of silicon-based semiconductor detectors assembled cylindrically around the LHC beam pipe. Figure 2.4 shows a schematic view of the ITS, indicating its three subdetector systems: the Silicon Pixel Detector (SPD), the Silicon Drift Detector (SDD) and the Silicon Strip Detector (SSD). Each subdetector implements a different silicon detector technology and consists of two consecutive layers. The active detector layers span radii between 3.9 cm and 43 cm, and the ITS covers full azimuth and a pseudorapidity range of $|\eta| < 0.9$ for particles created within ± 5 cm relative to the nominal collision vertex position along the beam direction.

The main purpose of the ITS is to measure track points along the trajectory of charged particles passing through the detector. Due to its radial proximity to the interaction point, the ITS is essential for precisely localizing the primary vertex of a collision and for finding secondary vertices from decays of hyperons and heavy-flavor particles. The track constraints provided by the ITS improve the track resolution near the vertex and are therefore crucial for separating primary from secondary charged particles. In particular, the SPD, the innermost subdetector of the ITS, offers a fine pixel granularity close to the collision where the particle densities are high. The signal

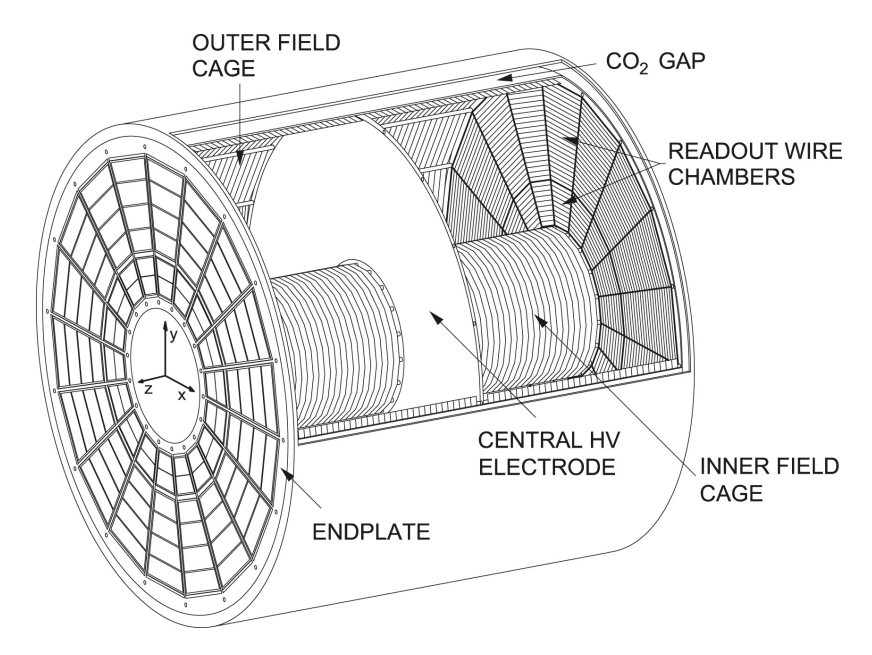


Figure 2.5: Schematic view of the ALICE Time Projection Chamber [70].

amplitudes measured with the SDD and SSD furthermore allow for identifying low momentum particles via their specific energy loss in the detector material.

Further technical details of the ITS are described in Ref. [68]. For LHC Run 3 the ITS is replaced with a seven-layer silicon pixel detector based on the Monolithic Active Pixel Sensor (MAPS) technology [69].

2.2.3 Time Projection Chamber

The Time Projection Chamber (TPC) constitutes the main tracking detector of ALICE, capable of measuring charged-particle trajectories with full azimuthal coverage in a pseudorapidity range of $|\eta| < 0.9$. The TPC consists of an $88\,\mathrm{m}^3$ large gas-filled cylindrical barrel installed around the ITS and has a length and diameter of 5 m, making it the largest TPC to date. As illustrated in Figure 2.5, a central electrode subdivides the volume of the TPC into two parts, denoted as A-side and C-side. The endplates on both sides are segmented into 18 trapezoidal-shaped sectors, each consisting of an inner and an outer read-out chamber. A high voltage difference of $100\,\mathrm{kV}$ between the central electrode and the two cathode endplates of the barrel generates homogeneous electric fields. These fields are aligned in parallel to the magnetic field of the L3 solenoid magnet surrounding the experiment.

Charged particles traversing the TPC ionize the gas molecules along their paths. The

freed electrons are pulled towards the endplates of the detector, where the position, arrival time, and signal amplitude are read out. This signal amplitude is proportional to the number of freed electrons per unit path length. The TPC gas consists of an ionizing noble gas (Ar or Ne) and a quencher gas (CO₂) intended to absorb photons produced during signal amplification. For a given gas mixture, the mean energy loss per unit path length due to the ionization depends only on the particle's velocity and charge as described by the Bethe-Bloch formula [3]. By reconstructing this specific energy loss through the measured signal amplitudes and combining it with the momentum measurement for the corresponding track, the particle species can be identified.

As a result of scattering with the gas molecules, the electrons accelerated by the electric field move with a constant drift velocity towards the readout chambers. The measured digits on the readout pads are merged to so-called clusters. The space points along the particle's path are inferred from the positions of these reconstructed clusters in the readout plane together with the arrival times of the signals, which, due to the constant drift velocity of the electrons in the TPC gas, allow locating the ionization coordinate in the beam direction. In LHC Run 2 the intended average electron drift velocity is $\langle v_{\rm drift} \rangle = 2.65\,{\rm cm/\mu s}$ [71] corresponding to a maximum drift time of 94 µs. The exact electron drift velocity depends on environmental conditions like the gas mixture, pressure and temperature and, therefore, needs to be precisely calibrated for the track reconstruction.

Electrons reaching the endplates are detected by the readout system. The system is composed of multi-wire proportional chambers (MWPCs) and a subsequent pad plane consisting of 159 tangential pad rows. Within the MWPCs, the incoming electrons are accelerated between a cathode and an anode wire grid to initiate a cascade of further ionization processes. The free electrons almost immediately reach the anode wires, while the heavier ions drift relatively slowly back towards the cathode while inducing mirror charges on the pad plane. These signals are picked up and digitized by the readout electronics. After the maximum drift time that electrons produced in the primary ionization processes need to reach the end plates, a gating grid is activated to prevent the ions from entering the drift volume of the TPC, which would otherwise cause significant distortions of the electron drift paths. This gated operation of the MWPCs limits the readout rate of the TPC. While the gating grid is open, also

additional ionization electrons of particles from previous or later collisions can (with a biased drift-time measurement) contribute to the measured signals assigned to an event. This so-called pileup can affect the tracking performance and the corresponding reconstructed tracks need to be identified and disregarded in the subsequent physics analyses.

Further technical details of the TPC can be found in Ref. [71]. For LHC Run 3 the MWPCs were replaced by so-called Gas Electron Multipliers (GEMs) to enable a continuous operation of the TPC [72].

2.3 Data preprocessing

In order to reconstruct the charged particles emerging from a collision, the detector signals measured with the ITS and TPC need to be calibrated and clustered to obtain three-dimensional space points which are then connected to the corresponding trajectories. These reconstructed tracks allow inferring the particles' momenta. The data reconstruction is centrally carried out by the ALICE Data Preparation Group. It is performed separately for each data-taking period – a series of consecutive runs with the same collision setup. The reconstruction is performed shortly after recording the data and occasionally repeated with improvements to the calibration and tracking software. As a consequence, for most of the data-taking periods, multiple so-called reconstruction passes are available for physics analyses. After the conclusion of LHC Run 2, a consistent reprocessing and reconstruction of most LHC Run 2 and selected LHC Run 1 datasets has been performed incorporating the most advanced detector calibration and reconstruction procedures.

The following paragraphs outline selected aspects of data taking and preprocessing to ease the understanding of the analysis description provided in Section 3.

Minimum-bias triggers The LHC beams provide a high frequency of crossing particle bunches at the ALICE interaction point. To register hadronic interactions between ions in the crossing bunches and initiate the recording of an event a so-called minimum-bias (MB) trigger is employed. The minimum-bias trigger condition is intended to select collisions with as little physics bias as possible while suppressing background events originating from interactions of beam particles with residual gas

molecules in the LHC vacuum pipes.

The low interaction rate data-taking periods of LHC Run 1 employ a highly effective MB trigger denoted as V0OR that requires a signal in either of the V0A, V0C, or SPD, and hence is sensitive also to single-diffractive pp collisions. With the increasing interaction rates in LHC Run 2, the contribution from beam-gas-induced background events rises. Therefore, the more stringent V0AND trigger condition is implemented, which requires a coincidence of signals in both V0A and V0C. V0AND almost exclusively selects non-single diffractive interactions.

Since V0OR and V0AND are sensitive to different types of collisions, the MB trigger employed to record the data also affects the efficiency corrections that have to be applied to the experimental data as discussed in Section 3.

Event reconstruction The detector signals measured with the ITS and TPC are grouped into clusters, calibrated, and passed through a centralized event reconstruction procedure described in Ref. [73]. The clusters are connected to a track using the Kalman filter technique [74]. In ALICE, this Kalman filter is employed in three consecutive tracking steps (inward-outward-inward scheme): The algorithm starts with a so-called track seed constrained by a pair of clusters at the outer radius of the TPC and a preliminary collision vertex. The vertex is defined as the crossing point of most straight lines connecting clusters in the two innermost ITS layers, the so-called SPD tracklets.

Starting from the track seed, the Kalman filter searches for compatible clusters along the helix-like path of the charged particle in the magnetic field. The local track parameters (position and momentum vectors) are continuously refined based on the found clusters while following the track inward in the TPC. This cluster-finding approach naturally reflects the stochastic nature of the particle's actual motion through the detector, which is affected by multiple scattering and energy loss in the TPC gas. From the signal amplitudes of the TPC clusters associated with the track, a preliminary particle hypothesis is obtained which allows incorporating the effect of its energy loss on the predicted trajectory in the consecutive tracking steps. In case multiple tracks are reconstructed with a large fraction of overlapping clusters, only the track with the best quality is kept. Tracks with too few contributing clusters (in total or compared to the geometrical expectation) are removed from the sample of track candidates. The

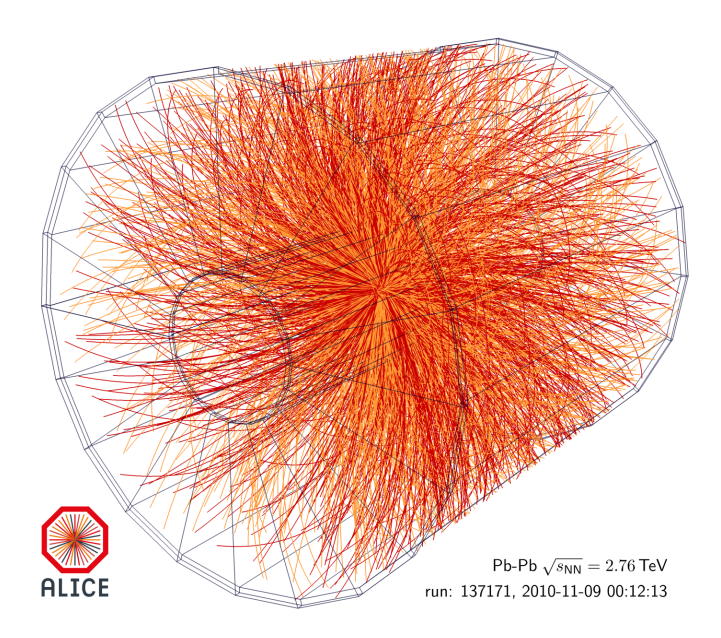


Figure 2.6: Event display of the tracks reconstructed for an exemplary Pb–Pb collision measured with ALICE [76].

remaining tracks are further constrained with compatible ITS clusters. In the second tracking step, the trajectories are propagated outward starting with the current set of parameters at the closest point to the preliminary vertex and considering the expected energy loss. This iteration gives an updated mass hypothesis for the final inward fit of the track. From the prolongation of these tracks, the collision vertex position is determined, which is more accurate than the one obtained from the SPD tracklets. The final track parameters are stored at the distance of closest approach (DCA) to this vertex, hence representing the particle properties (momenta) at the origin of production.

The presented procedure corresponds to the track finding for so-called primary charged particles. In ALICE, a primary charged particle [75] is defined as a charged particle with a mean proper lifetime τ larger than $1\,\mathrm{cm/c}$, which is either produced directly in the interaction or from decays of particles with τ less than $1\,\mathrm{cm/c}$, excluding particles produced in interactions with the detector material. Particles from weak decays originate from secondary vertices further away from the collision vertex and are therefore found with a slightly different tracking procedure described in Ref. [73]. Figure 2.6 shows the reconstructed trajectories of particles produced in a central Pb–Pb collision, illustrating that the tracking procedure is capable of finding thousands

of distinct particle trajectories. In this work, the number of those reconstructed tracks as well as their transverse momenta are the basis for the further analysis.

Pileup At the ALICE interaction point, the LHC beams are aligned such that multiple collisions in the same bunch-crossing are unlikely to occur. In those rare cases, however, the additional particles contaminate the track sample associated with a collision and hence bias the measurement. For such in-bunch pileup events, the tracks or SPD tracklets prolonged to the beam pipe point to more than one collision vertex and can thus be identified and removed in the present analysis.

Drift electrons originating from bunch crossings previous to or after the trigger event can contribute to the signals measured during the TPC read-out time of a collision. This so-called out-of-bunch pileup degrades the tracking performance and is particularly relevant for data-taking at high interaction rates. Reconstructed tracks from these pileup events can be distinguished from the particles emerging from the trigger collision through their DCA to the vertex. The drift time measurement of tracks from pileup events is biased since it is calculated in reference to the trigger collision and hence all corresponding space points are shifted along the beam direction. Tight selections on the DCA of the tracks can therefore efficiently remove pileup particles from the track sample selected for further analysis.

Quality assurance Data-taking periods usually span long time intervals, during which the detector availability and performance can vary. A centralized quality assurance (QA) monitors the data quality for each run to identify outliers from the trend of the period that potentially have bad quality. Based on the feedback provided by various detector experts the Data Preparation Group prepares lists of good-quality runs suited for different types of analyses. The runs analyzed in this work are mostly selected based on these centrally provided run lists.

2.4 Monte Carlo simulations

As discussed in Section 1.4, correcting reconstructed experimental data requires understanding the detector's response to particles produced in a collision. Therefore, the data measured with ALICE is generally complemented by centrally produced Monte Carlo (MC) simulations. The collisions underlying these simulations are provided by event generators implementing QCD-inspired models. The MC productions used in this work are based on the event generators PYTHIA for pp, EPOS LHC for p-Pb, and HIJING [77] for AA collisions. Particles emerging from these simulated collisions are propagated through a virtual GEANT3 [78] model of the ALICE experiment, where they interact with the detector material and produce detector signals which are then used as input to the same event reconstruction procedure as the experimental data. To correctly reflect the state of all detectors during data-taking, the simulations are anchored to the different experimental runs. Hence, they reproduce time-dependent changes in detector performance and phase space acceptance during the measurement. For a more realistic description of the TPC's tracking performance at high interaction rates, the MC simulations anchored to LHC Run 2 data also include pileup collisions. Due to the limited amount of available computing resources it is in practice not feasible to simulate all measured particle collisions of an anchored run. Instead, it is ensured that the relative number of particle collisions between runs are consistently simulated. The anchored MC simulations allow associating reconstructed tracks to the corresponding simulated particles and additionally give access to the generated particles that are not reconstructed with the virtual ALICE detector and thus can be used to correct the experimental data for detector effects.

3 Data analysis

The present analysis aims to measure the charged-particle final state of high-energy collisions at the LHC with unprecedented precision. It provides a comprehensive set of measurements for most LHC Run 1 and 2 data-taking campaigns, covering multiple collision systems and center-of-mass energies. For each of the ten different collision scenarios, two observables are measured: the charged-particle multiplicity distribution, i.e. the probability of producing a certain amount of particles in a collision, and the transverse-momentum spectra corresponding to these collisions. In particular, the latter correlation of particle production with $N_{\rm ch}$ and $p_{\rm T}$ is challenging to measure with high granularity since both the multiplicity and the transverse momentum are simultaneously biased by detector effects. Unfolding this 2D correlation using solely the procedure described in Section 1.4 would require a large amount of MC statistics to sufficiently populate the corresponding detector response. Since the number of events in the available ALICE simulations is usually limited, a novel approach to effectively achieve this 2D unfolding by approximating it as a sequence of multiple 1D unfolding steps was developed in the course of this thesis. Prior to the unfolding, a data-driven correction accounts for imperfections of the particle composition in the MC generators underlying the ALICE simulations to avoid biases in the detector response.

This section first outlines the general analysis strategy and workflow. Then, the datasets, as well as quality selections for the measured events and tracks are presented. Afterwards, the data-driven corrections of the MC particle composition are introduced, followed by a detailed discussion of the procedures employed to unfold the multiplicity distributions and the multiplicity-dependent $p_{\rm T}$ spectra.

3.1 Workflow

Figure 3.1 illustrates the general workflow employed in this analysis. For each dataset, the recorded LHC collisions and the corresponding anchored MC productions are processed by a so-called analysis task. This task applies kinematic and quality selection criteria on the data before it is used for local processing. In the MC analysis, additional generator-level information is accessed and stored. To correct for an inaccurate particle

3 Data analysis 3.2 Datasets

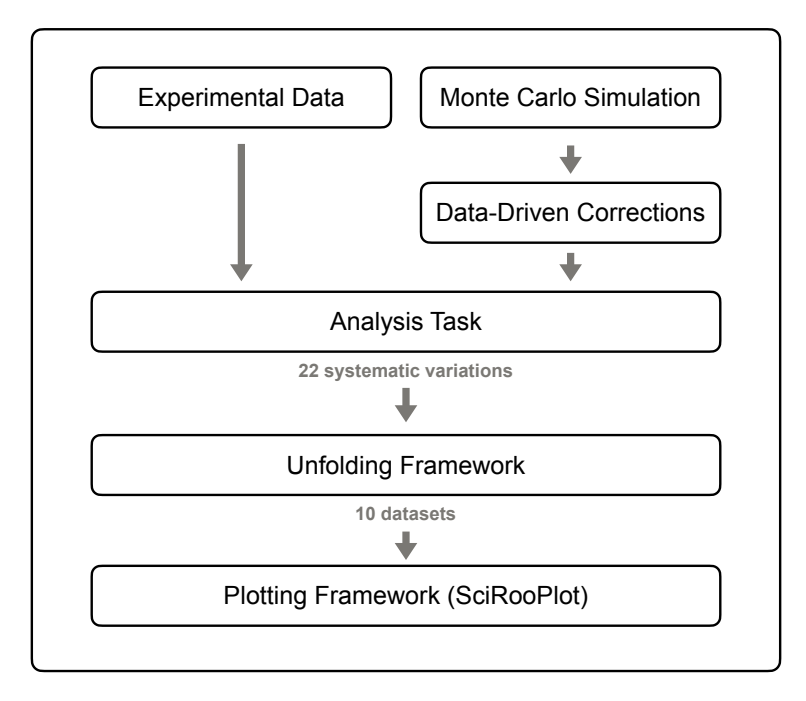


Figure 3.1: Workflow of the analysis.

composition an on-the-fly data-driven correction is applied to the MC data.

In order to correct the raw measurement for detector effects, the data and MC output files of the analysis task are further processed by an unfolding framework [79] based on RooUnfold.

The entire analysis chain is run multiple times for each of the ten datasets with varying analysis decisions (mostly track selections) to estimate the measurement's systematic uncertainties. To organize and display the many results of the analysis, in the course of this work a general-purpose plotting framework (SciRooPlot [80]) was developed by the author. All original figures shown in this thesis are created with this new open-source program.

3.2 Datasets

The data analyzed in this work covers all collision scenarios of LHC Run 1 and 2 except for two small datasets from the beginning of Run 1 (pp collisions with $\sqrt{s} = 0.9 \,\text{TeV}$ and 2.36 TeV). They comprise pp, p–Pb, Xe–Xe, and Pb–Pb collisions at center-of-mass energies per nucleon pair ranging from $\sqrt{s_{\text{NN}}} = 2.76 \,\text{TeV}$ up to 13 TeV. Table 1 summarizes the collision scenarios considered in this thesis, their year of data-taking, and the employed minimum bias trigger. It also lists the effective average interaction

3 Data analysis 3.2 Datasets

	$\sqrt{s_{\mathrm{NN}}}$ (TeV)	year	trigger	⟨IR⟩ (kHz)	sim. (X = with pileup)	<u>)</u>
pp	2.76	2011	VOOR	24.99	PYTHIA6 Perugia0	
	5.02	2017	V0AND	66.54	PYTHIA8 Monash13	X
	7	2010	V0OR	4.54	PYTHIA6 Perugia11	
	8	2012	V0AND	32.30	PYTHIA8 Monash13	
	13	2016	V0AND	123.82	PYTHIA8 Monash13	X
p–Pb	5.02	2016	V0AND	16.48	EPOS LHC	X
	8.16	2016	V0AND	27.54	EPOS LHC	X
Xe-Xe	5.44	2017	V0AND	0.15	HIJING	
Pb–Pb	2.76	2010	VOOR	0.12	HIJING	
	5.02	2015/18	V0AND	5.40	HIJING	X

Table 1: Overview of the analyzed collision scenarios, corresponding year of data-taking, trigger condition, effective average interaction rate, and generators used for the anchored MC simulations.

rates $\langle IR \rangle$ calculated by weighting each run's recorded minimum bias interaction rates with the respective number of collisions selected for analysis. The generators underlying the corresponding anchored MC simulations are given as well. For the most recently reconstructed datasets, the simulations marked with an X in the table contain pileup events. This pileup in the simulations is particularly important for the high IR datasets to best describe the detector performance.

All data-taking periods are used in their latest reconstruction pass available at the time of this thesis and with the corresponding anchored MC productions. The runs considered in this analysis are selected based on the central ALICE detector QA. For most of the datasets, a list of suitable runs is provided by the Data Preparation Group. For the remaining datasets, the run selections are based on information stored in the so-called ALICE Run Condition Table (RCT), a database containing QA details of the different detectors. Only runs with operational ITS and TPC are selected to ensure optimal charged-particle tracking performance. In particular, runs where TPC sectors were temporarily turned off during the data-taking are excluded. Hereby a homogeneous detector acceptance over the whole data-taking period is achieved. This is necessary since the MC productions in practice do not reproduce the relative abundances of events among the different runs in a data-taking period.

The LHC Run 2 datasets exhibit the highest quality since they were produced with the most up-to-date tracking and calibration software. In addition, the LHC Run 1 Pb–Pb data at $\sqrt{s_{\rm NN}}=2.76\,{\rm TeV}$ were also reconstructed with software improvements compared to older reconstruction passes, yet the corresponding MC does not include pileup. For some LHC Run 1 datasets, parts of the ITS were inoperational, resulting in minor holes in azimuth coverage. The track reconstruction of the pp collision data recorded at $\sqrt{s}=2.76\,{\rm TeV}$ was performed without including hits in the SDD layers of the ITS, resulting in a significantly degraded quality, and thus these data suffer from the largest uncertainties in the presented measurement. For pp collisions at $\sqrt{s}=2.76\,{\rm TeV}$ and $7\,{\rm TeV}$, the rather old PYTHIA version 6 is utilized in the two tunes Perugia0 and Perugia11 [81], respectively. The other pp datasets are complemented by MC simulations based on PYTHIA8 in its latest tune, Monash13 [13]. All data were taken at the nominal magnetic field of $0.5\,{\rm T}$ except for the Xe–Xe dataset, which was recorded at a lower magnetic field of $0.2\,{\rm T}$.

3.3 Event class and event selection

The events measured with ALICE represent a subsample of all INEL (see Section 1.2.1) collisions occurring in the LHC that are biased by the experiment's conditions. Furthermore, due to varying minimum-bias triggers and data-taking conditions in the experiment, e.g. interaction rates and detector efficiencies, the sample of events is strongly dataset-dependent. The reconstructed data must be corrected for these biases in the measurement such that the final results of the analysis represent a common class of events and thus are comparable among different datasets as well as to theoretical models. All corrections applied in this work are purely based on information from the MC simulations anchored to the respective experimental data and are discussed in detail in Section 3.6.

Corrections aiming at the class of INEL events come with a strong generator bias since for pp collisions they rely on an accurate modeling of diffractive processes. To reduce the contributions from diffraction, the LHC experiments often report their results for the so-called INEL>0 event class, defined as all collisions with one charged particle regardless of its momentum within $|\eta| < 1$ around midrapidity. In this work, all results are reported for collisions with at least one charged particle within ALICE's fiducial tracking acceptance $|\eta| < 0.8$ and $0.15 \, {\rm GeV}/c < p_T < 10 \, {\rm GeV}/c$, which also corresponds to the phase space region within which the multiplicity distributions and

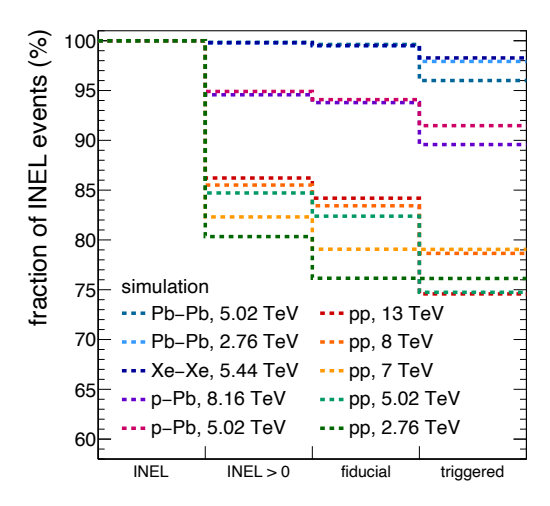


Figure 3.2: Fraction of all inelastic events in the MC simulations anchored to the data after sequentially selecting different event classes indicated at the axis. The underlying generators are listed in Table 1.

multiplicity-dependent $p_{\rm T}$ spectra are measured. The choice of this more stringent subset of the INEL>0 event class from now on is referred to as the fiducial event class. This avoids strong dependence on the correct modeling of low $p_{\rm T}$ charged particle production in the collisions.

Figure 3.2 displays the fraction of all INEL collisions contained in the INEL>0 and fiducial event classes, respectively, as predicted by the different MC generators listed in Table 1. For pp collisions, the number of events in the INEL>0 class is significantly reduced compared to INEL due to the suppressed diffractive collisions. The results indicate a larger contribution from diffractive processes in the older PYTHIA6 generators ($\sqrt{s}=2.76\,\mathrm{TeV}$ and $7\,\mathrm{TeV}$) compared to the PYTHIA8 generator used for the remaining pp collision energies. This highlights that it would not be advisable to use the MC simulations to correct the experimental data towards the INEL event class. For p–Pb collisions the EPOS LHC generator predicts only a 5% difference between INEL>0 and INEL, while for AA collisions all INEL collisions are also part of the INEL>0 class according to the HIJING generator. In all cases, the fiducial event class slightly reduces the sample of considered events further, with the largest effect observed for the PYTHIA6 simulations. In AA collisions almost all INEL events are part of the fiducial event class, around 94% of the p–Pb collisions, but only 75-85% of all pp collisions remain.

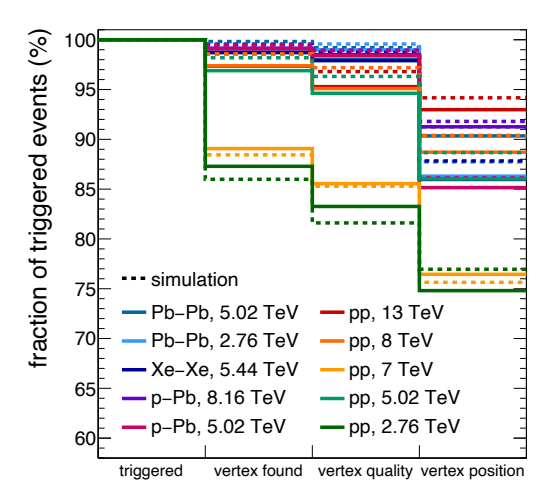


Figure 3.3: Fraction of triggered collisions remaining after sequentially applying the selection criteria indicated at the axes.

The last column of Figure 3.2 shows the fraction of INEL events contained in the fiducial event class that remains after applying the respective trigger condition (V0OR or V0AND, see Table 1) as well as additional background and pileup removal criteria. These selections are equivalent to the ones applied to the experimental data: Inelastic beam-gas interactions in the LHC are identified and rejected based on the coincidence of the timing information in the two V0 detectors or the correlation between the number of clusters and tracklets in the SPD. Events with more than one reconstructed vertex within the SPD readout time are considered as pileup.

In addition, further event selections are applied to the triggered events after pileup and background rejection to ensure adequate data quality: Collisions in which a vertex is found (vertex found) and those with good vertex resolution (vertex quality) are considered. Additionally, a reconstructed primary vertex must be located within $|V_{\rm z}^{\rm meas}| < 10\,{\rm cm}$ along the beam direction relative to the nominal interaction point to ensure a pseudorapidity coverage of $|\eta| < 0.8$ for all tracking detectors (vertex position).

Figure 3.3 shows the fraction of all triggered events (excluding pileup and beam-induced background) after sequentially requiring the different event selection criteria both for the experimental data and the MC simulations. For the V0OR triggered pp datasets ($\sqrt{s} = 2.76\,\text{TeV}$ and $7\,\text{TeV}$), the vertex requirement significantly reduces the sample size since the vertex finding for single diffractive events is less efficient.

3 Data analysis 3.4 Track selection

	$\sqrt{s_{\mathrm{NN}}}$ (TeV)	events data (M)	events MC (M)	MC / data (%)
	2.76	47.63	2.88	6
pp	5.02	315.99	60.59	19
	7	128.98	126.07	98
	8	25.88	44.27	171
	13	180.15	43.87	24
n Dh	5.02	309.48	63.62	21
p–Pb	8.16	14.5	2.92	20
Xe-Xe	5.44	1.17	6.09	521
Pb–Pb	2.76	18.66	0.72	4
	5.02	239.03	4.92	2

Table 2: Number of collisions after event selection.

Overall, the effect of the selections on experimental data is fairly well reproduced by the anchored MC simulations.

Table 2 presents the resulting number of selected events for each dataset and the corresponding MC simulation. The available statistics for the different measurements vary significantly, between 1 M and 300 M events. The right column of the table shows the fraction of selected events reproduced by the corresponding MC simulation, ranging from a few percent up to 5 times the experimental data.

3.4 Track selection

The present measurement focuses on primary charged particles produced within the kinematic range $0.15\,\mathrm{GeV}/c < p_\mathrm{T} < 10\,\mathrm{GeV}/c$ and $|\eta| < 0.8$. At lower transverse momenta, the efficiency for reconstructing a track drops significantly for data taken at the nominal magnetic field. Restricting the analysis to $p_\mathrm{T} < 10\,\mathrm{GeV}/c$ ensures that for all datasets a sufficient number of simulated particles are available to enable the differential unfolding corrections intended in this work.

A sample of tracks reconstructed within this kinematic range can also contain trajectories originating from secondary particles or particles from pileup collisions. In addition, some tracks may not be well constrained by their corresponding measured space points, resulting in poor precision of the transverse momentum. Extensive studies for previous ALICE publications [34, 48], which are similar to the analysis presented in this thesis, found a set of selection criteria optimized for minimal contamination and best track

3 Data analysis 3.4 Track selection

quality. These selection criteria are briefly motivated in the following.

• Tracks originating from a location close to the primary interaction vertex are less likely products of weakly decaying particles, interactions with the detector material, or pileup collisions. Therefore, tight selections on the closest distance of the extrapolated tracks to the primary vertex, the distance of closest approach (DCA_{xy}) and DCA_{z} , allow obtaining a pure sample of the desired primary charged particles. The DCA resolution improves when a track is constrained by ITS space points close to the collision vertex. In general, the DCA in the transverse plane becomes smaller with increasing transverse momentum of the track. The corresponding DCA_{xy} distributions are parametrized in p_T intervals so that tracks can be selected relative to the widths (σ_0) of these distributions. In practice, a power-law parametrization of σ_0 as a function of p_T is utilized to interpolate these widths to arbitrary transverse momenta.

- The accuracy of a track's measured transverse momentum can degrade if only a small fraction of TPC space points are detected along its path or if it shares many clusters with other tracks. Applying threshold values for these properties filters out falsely reconstructed and low-quality tracks.
- The length of a track's projected curve in the TPC readout plane depends on its transverse momentum. Since the active tracking volume is separated by dead areas in azimuth due to the TPC sector boundaries, the so-called geometric length of a track further depends on its exact topology. For each track, a minimum geometric length in centimeters of $L = A B \cdot p_{\rm T}^C$ with baseline length A, and the parameters $B = 1 \, {\rm cm} \cdot ({\rm GeV}/c)^{-C}$ and C = -1.5 is required, of which 85% must be detected with the TPC readout pad rows crossed by the track.
- An essential quality measure for the accuracy of a track is defined by the χ^2 between its reconstructed path and the constraining space points. This χ^2 is determined separately for the ITS and the TPC ($\chi^2_{\rm ITS}$ per ITS cluster and $\chi^2_{\rm TPC}$ per TPC cluster). Tracks with incorrectly assigned ITS clusters or from particles where significant scattering occurred in the detector material between the ITS and TPC are identified via the $\chi^2_{\rm TPC-ITS}$ quantifying the difference of a TPC track constrained to the primary vertex and the global track including the ITS.

3 Data analysis 3.4 Track selection

track selection criterion	nominal value	variations	
		lower	higher
$max. DCA_z$	$2\mathrm{cm}$	$1\mathrm{cm}$	$5\mathrm{cm}$
$\max DCA_{xy}$	$7 \sigma_0$	$4 \sigma_0$	$10 \sigma_0$
one hit in the SPD	required	not required	
max. fraction of shared TPC clusters	0.4	0.2	1
min. ratio of crossed rows over findable clusters	0.8	0.7	0.9
geometric length (track length)	$130\mathrm{cm}$	$120\mathrm{cm}$	$140\mathrm{cm}$
geometric length (dead TPC area)	$3\mathrm{cm}$	$2\mathrm{cm}$	$4\mathrm{cm}$
max. χ^2_{TPC} per TPC cluster	4(2.5)	3(2)	5(3)
max. $\chi^2_{\rm ITS}$ per ITS cluster	36	25	49
max. $\chi^2_{\text{TPC-ITS}}$	36	25	49

Table 3: Track selection criteria and their systematic variations.

Table 3 summarizes the values of the track selection criteria used in this analysis, which are equivalent to the ones employed in Refs. [34, 48], with one exception concerning the maximum $\chi^2_{\rm TPC}$ per TPC cluster. In the newly reconstructed Run 2 datasets, an improvement of the error propagation in the tracking algorithm results in smaller $\chi^2_{\rm TPC}$ values compared to previous reconstruction passes. Therefore, another threshold value (indicated in brackets in the table), is used to achieve an equivalent selection of tracks.

The selection criteria enhance the purity and quality of the considered track sample and focus the analysis on a domain where the complementary MC simulations reliably reproduce the track properties. Operating in a regime where the simulations properly represent the detector performance is crucial to ensure that the corrections applied to the reconstructed data are accurate. Variations of the chosen track selection criteria allow for estimating the precision of the applied corrections. Table 3 lists upper and lower variations of all the track selection criteria as those are used for determining the systematic uncertainties of the present measurement.

Figure 3.4 shows the average relative $p_{\rm T}$ resolution of the selected tracks for all datasets considered in this work. The resolution is inferred from the measurement uncertainty of the inverse transverse momentum, according to $\sigma_{p_{\rm T}}/p_{\rm T} \approx p_{\rm T} \ \sigma_{1/p_{\rm T}}$. All selected tracks exhibit an excellent $p_{\rm T}$ resolution well below 4%, with the highest precision around $p_{\rm T} \approx 1-2\,{\rm GeV}/c$. Multiple scattering of the produced particles with the detector material deteriorates the resolution of low- $p_{\rm T}$ tracks. Towards large transverse

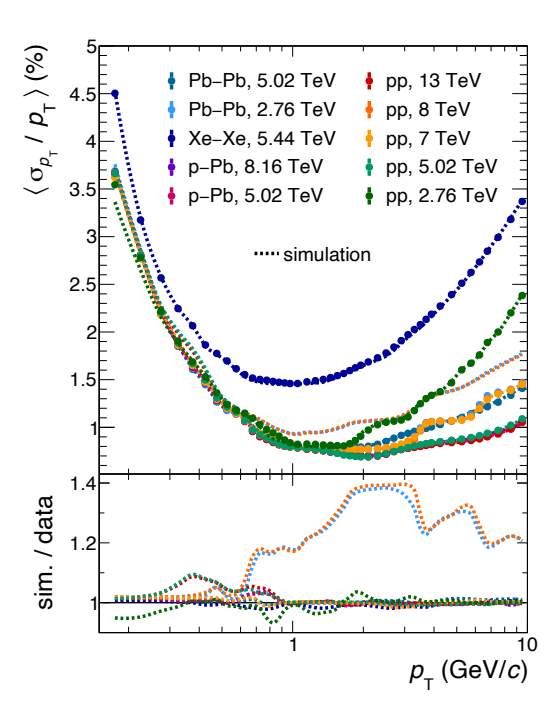


Figure 3.4: Average relative $p_{\rm T}$ resolution of the selected charged-particle tracks for the different datasets as well as from the corresponding MC simulations.

momenta, the track's curvature becomes smaller and, therefore, more difficult to resolve over the length of the particle's path within the detector volume leading to a worsening of the $p_{\rm T}$ resolution. A similar effect is observed for the Xe–Xe dataset, as the lower magnetic field results in straighter tracks. Among the data taken at the nominal magnetic field, the tracks from pp collisions at $\sqrt{s}=2.76\,{\rm TeV}$ exhibit the worst $p_{\rm T}$ resolution. Figure 3.4 also shows the $p_{\rm T}$ resolution for the anchored MC simulations as dotted lines. The simulations almost perfectly reproduce the $p_{\rm T}$ resolution of the reconstructed tracks. Only for Pb–Pb collisions at $\sqrt{s_{\rm NN}}=2.76\,{\rm TeV}$ and pp collisions at $\sqrt{s}=8\,{\rm TeV}$, the simulations predict a worse resolution above $p_{\rm T}\approx 1\,{\rm GeV}/c$. However, since the $p_{\rm T}$ resolution is well below 2%, this deviation from the experimental data does not significantly affect the results of the present analysis.

3.5 Particle-composition correction

In this work, all corrections applied to the experimental data are based on MC simulations relying on event generators that define the abundances of the different particles produced in a collision. Since the tracking capability of the ALICE detector

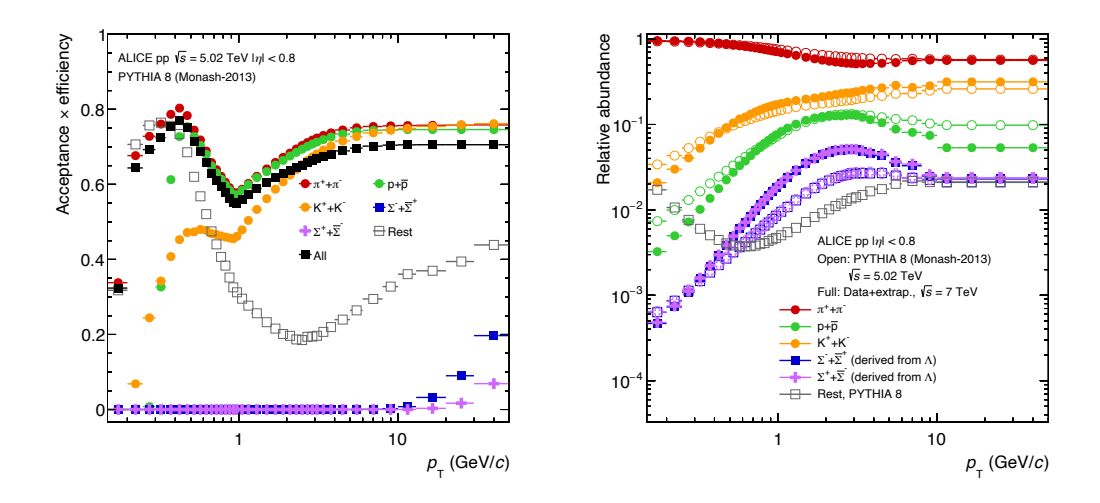


Figure 3.5: Acceptance times efficiency (in this work collectively denoted as efficiency, see Section 1.4) of different charged-particle species (left) [34] and the particle composition derived from ALICE measurements compared to PYTHIA (right) [34].

system varies for different particle species, the average efficiency for reconstructing an unidentified charged particle in the simulation depends on the composition of the generated particles.

The left panel of Figure 3.5 illustrates that the tracking efficiency for kaons, the second most abundantly produced particle species, differs significantly from the efficiency for tracking the prevalent pions. It was found in previous measurements [82, 83] that current MC event generators do not perfectly reproduce the experimentally observed relative particle abundances, in particular for particles with strangeness content. This is illustrated in the right panel of Figure 3.5, where the measured particle composition (closed markers) is compared to the one generated by PYTHIA (open markers).

In order to correct the resulting bias in the inclusive charged-particle analysis, the particle abundances from the event generator are re-weighted to match the measured ones. For the present work the particle composition correction was extended [84] compared to previous publications [85, 34, 48]. The particle-composition correction utilizes several ALICE π , K, p and Λ (a proxy to construct Σ) measurements of p_T spectra as a function of multiplicity (in coarse intervals) for different collision systems [83, 86, 87, 88, 89]. These measurements comprise only one center-of-mass energy per collision system (pp. 13 TeV; p–Pb, 5.02 TeV; Pb–Pb, 2.76 TeV) but are still vi-

able to correct all datasets considered in this thesis as the particle composition only depends on the multiplicity as apparent in Figure 1.8. From these interpolated measurements, scaling factors suited for each considered MC generator are determined as a function of particle species, multiplicity, and transverse momentum. While processing the MC simulation with the analysis task, a particle is considered an integer number of times corresponding to its randomly rounded scaling factor. This on-the-fly scaling of the particle abundances affects the multiplicity on an event-by-event basis. The correction changes the inclusive charged-particle tracking efficiency most prominently around $p_{\rm T} \approx 3\,{\rm GeV}$ where it can drop by up to 5%. The effect of the PCC is less pronounced for MC simulations based on the EPOS LHC event generator due to its more accurate particle composition. An imperfect composition of particles produced by the generator also affects the MC estimate for feed-down contamination from weakly decaying particles in the track sample selected for analysis. The particle-composition correction accounts for these imperfections in the estimated feed-down contamination, changing it by up to 50%.

3.6 Unfolding corrections

The main goal of this analysis is to find the correlation between primary charged-particle $p_{\rm T}$ spectra and their corresponding event multiplicities $N_{\rm ch}$, both defined in the kinematic range $0.15\,{\rm GeV}/c < p_{\rm T} < 10\,{\rm GeV}/c$ and $|\eta| < 0.8$. In the experiment, however, this observable is affected by the measurement process. The measured transverse momentum $p_{\rm T}^{\rm meas}$ is smeared with respect to the particle's true transverse momentum $p_{\rm T}$ due to the detector resolution. The measured multiplicity $N_{\rm ch}^{\rm meas}$ consists of only a fraction of the true number of primary charged particles $N_{\rm ch}$ remaining after tracking efficiency losses. In addition, it contains tracks from secondary particles or particles smeared into the kinematic acceptance of the measurement as a result of detector resolution (i.e. from $|\eta| \geq 0.8$ or $p_{\rm T} \leq 0.15\,{\rm GeV}/c$, $p_{\rm T} \geq 10\,{\rm GeV}/c$). Due to event-by-event fluctuations of the tracking efficiency and the contamination of the track sample, the correlation between $N_{\rm ch}$ and $N_{\rm ch}^{\rm meas}$ is not unique. Multiple collisions with a true multiplicity $N_{\rm ch}$ can be measured with different $N_{\rm ch}^{\rm meas}$ and, hence, contribute to various multiplicity-dependent $p_{\rm T}^{\rm meas}$ spectra. Consequently, each of those spectra contains particles originating from events with many true multiplicities. This implies

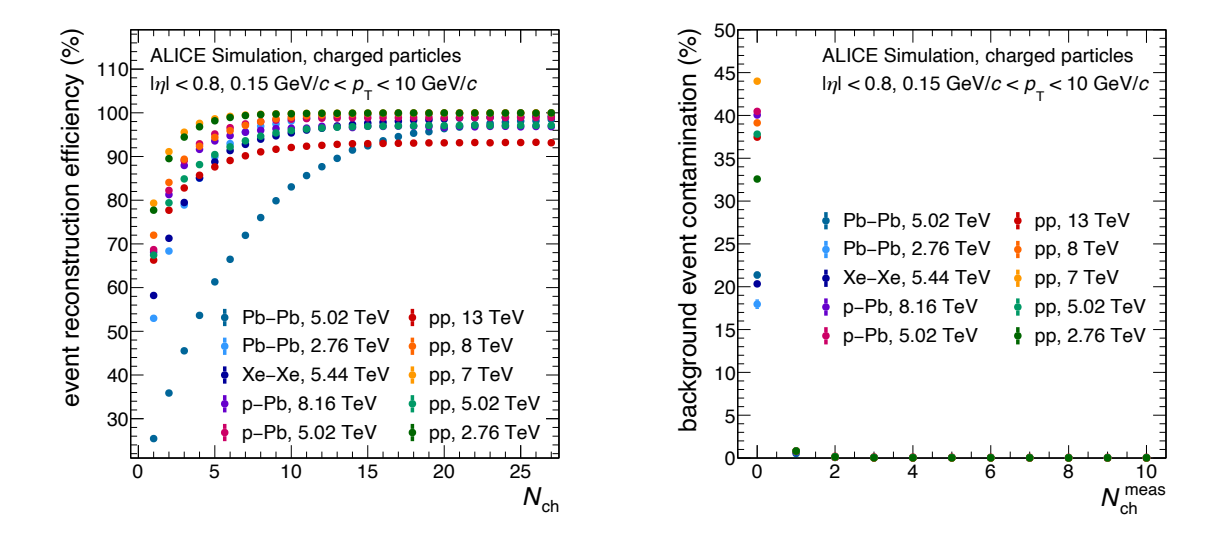


Figure 3.6: Event reconstruction efficiency as a function of $N_{\rm ch}$ (left) and background event contamination as a function of $N_{\rm ch}^{\rm meas}$ (right).

that the physical quantity characterizing the final state of a collision ($p_{\rm T}$ spectra vs. $N_{\rm ch}$) eludes direct observation and can be extracted only by deconvoluting the measured data.

The following subsections first illustrate the unfolding of event multiplicity distributions, a more straightforward, one-dimensional problem that is directly solvable with the iterative deconvolution procedure presented in Section 1.4. Then, the sequential 2D unfolding approach employed to extract the $N_{\rm ch}$ -dependent $p_{\rm T}$ spectra is described. To characterize the evolution of the $p_{\rm T}$ spectra with $N_{\rm ch}$, their mean transverse momentum $\langle p_{\rm T} \rangle$ and standard deviation $\sigma(p_{\rm T}) = \sqrt{\langle (p_{\rm T} - \langle p_{\rm T} \rangle)^2 \rangle}$ are presented as a function of multiplicity.

In the following, the technical details of the analysis are illustrated only for pp collisions at $\sqrt{s} = 5.02 \,\text{TeV}$. This example dataset is used to conceptually describe the analysis procedures. The corresponding figures for the nine remaining datasets are similar as documented in the ALICE-internal note [90] supplementing this analysis.

While the analysis is carried out for the whole range of multiplicities, all figures shown in the following will be restricted to dataset-dependent maximum $N_{\rm ch}$ values, after which the final results are found to have large systematic uncertainties.

3.6.1 Multiplicity distributions

The first part of the analysis aims to determine the probability density $P(N_{\rm ch})$ for producing a certain amount of charged particles within $0.15\,{\rm GeV}/c < p_{\rm T} < 10\,{\rm GeV}/c$ and $|\eta| < 0.8$. All corrections applied to the measured multiplicity distribution $n(N_{\rm ch}^{\rm meas})$ are calculated with respect to the fiducial event class, i.e., those simulated collisions with at least one charged particle within the aforementioned kinematic range. To avoid unnecessary MC-based extrapolation, the true vertex position in the MC simulation ($|V_{\rm z}| < 10\,{\rm cm}$) is restricted to the same range as the measured vertex position ($|V_{\rm z}^{\rm meas}| < 10\,{\rm cm}$). This selection does not affect the final observable $P(N_{\rm ch})$ since the results obtained within this restricted range around the nominal vertex position are representative for all collisions.

In the measurement some collisions are not registered by the minimum-bias trigger or disregarded by the subsequent event selection. These efficiency losses need to be corrected for. The total efficiency for reconstructing a collision of the fiducial event class with a vertex located within $|V_z| < 10 \,\mathrm{cm}$ is shown in the left panel of Figure 3.6 as a function of $N_{\rm ch}$ for the MC simulations of the ten considered datasets. This event reconstruction efficiency is reduced for low multiplicity collisions since the small number of produced particles reduces the probability for triggering the data-taking and finding a vertex of the required quality. The two pp datasets recorded with the more sensitive V0OR trigger ($\sqrt{s} = 2.76 \,\text{TeV}$ and $7 \,\text{TeV}$) exhibit a slightly higher efficiency. A multiplicity-independent efficiency reduction is observed for all MC simulations containing pileup as the employed event selection criteria reject triggered events with additional collisions in their vicinity. This constant efficiency reduction is most prominently visible for pp collisions at $\sqrt{s} = 13 \,\text{TeV}$, which corresponds to the dataset with the highest interaction rate as summarized in Table 1. The lowest event reconstruction efficiency is observed for peripheral Pb-Pb collisions at $\sqrt{s_{\rm NN}} = 5.02 \, {\rm TeV}$. Presumably this is caused by the dataset-dependent event selection criteria that are not optimized for these low multiplicity events since heavy-ion analyses of the ALICE collaboration rarely focus on collisions with centralities above 80 %.

Another measurement effect is the contamination with background events. The right panel of Figure 3.6 shows the background contamination of the selected event sample as a function of the measured track multiplicity $N_{\rm ch}^{\rm meas}$. The contamination consists

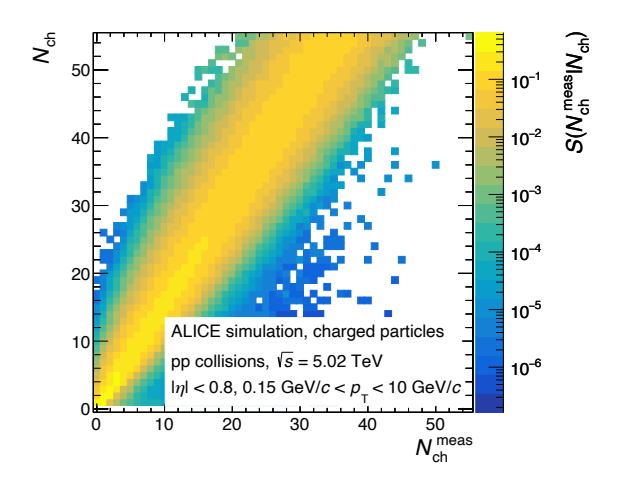


Figure 3.7: Multiplicity-smearing matrix of the example dataset.

of collisions located outside $|V_z| < 10\,\mathrm{cm}$ or not belonging to the fiducial event class. Events with $N_\mathrm{ch}^\mathrm{meas} = 0$, i.e. without any track of sufficient quality reconstructed in the considered kinematic range, exhibit the largest contamination, which, depending on the dataset, ranges from 15 % to 45 % of the selected events. For $N_\mathrm{ch}^\mathrm{meas} > 0$, the background contamination of the selected event sample is negligibly small.

The tracking efficiency and track sample contamination influence the track multiplicity measured for a given event. The probability to measure $N_{\rm ch}^{\rm meas}$ tracks in a collision with multiplicity $N_{\rm ch}$ is encoded in the smearing matrix $S(N_{\rm ch}^{\rm meas}|N_{\rm ch})$. Figure 3.7 shows this smearing matrix for the example dataset. On average, the track multiplicity $N_{\rm ch}^{\rm meas}$ is 30-50% smaller than the original charged-particle multiplicity $N_{\rm ch}$ with a considerable spread around the corresponding $\langle N_{\rm ch}^{\rm meas} \rangle$.

In the analysis, the presented efficiency, contamination, and smearing information are used to unfold the experimentally measured multiplicity distributions $n(N_{\rm ch}^{\rm meas})$ following the procedure described in Section 1.4. The resulting fully corrected multiplicity distributions $n(N_{\rm ch})$, which correspond to the total number of collisions within the chosen multiplicity intervals $\Delta N_{\rm ch}$, are then normalized to represent the corresponding probability density:

$$P(N_{\rm ch}) = \frac{1}{\Delta N_{\rm ch}} \frac{n(N_{\rm ch})}{\sum_{N'_{\rm ch}} n(N'_{\rm ch})} \quad . \tag{3.1}$$

To quantify the accuracy of the unfolding method, a closure test is performed, as discussed in the following.

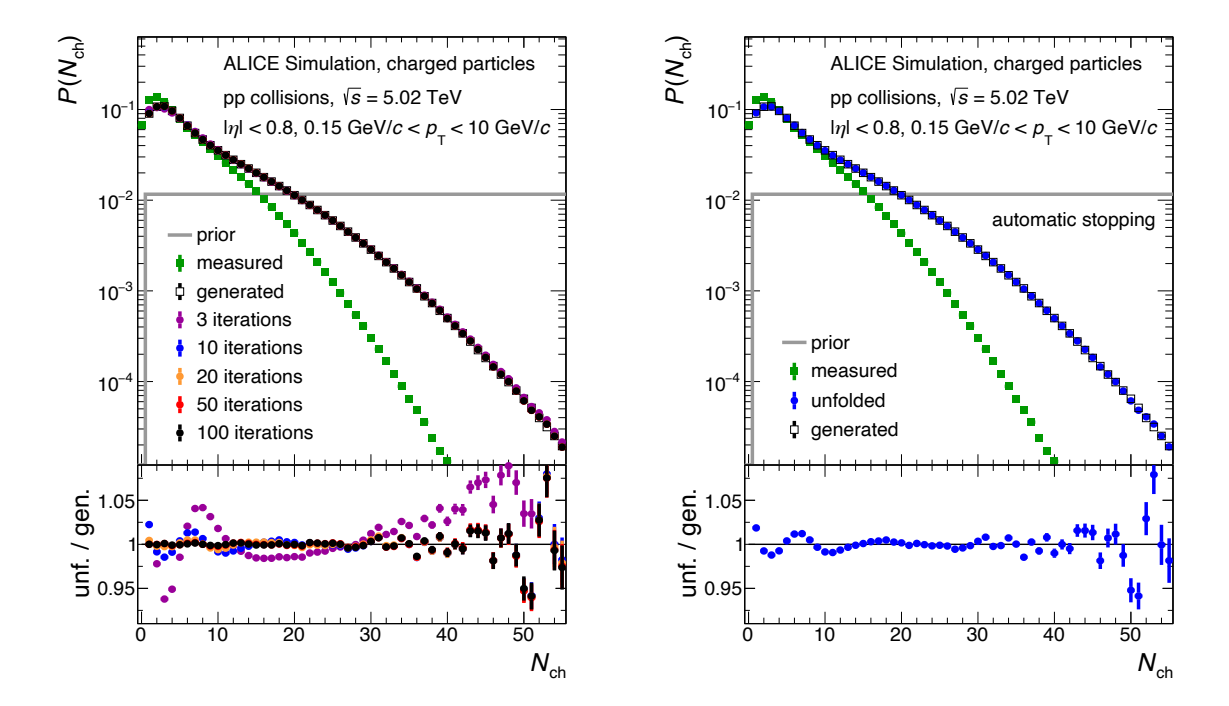
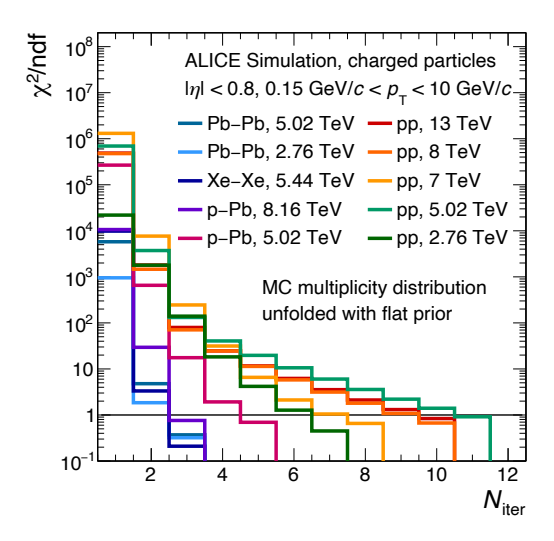


Figure 3.8: Measured, unfolded, and generated multiplicity distributions from the MC simulation anchored to the example dataset. The unfolding procedure is started with a flat prior. The unfolding is stopped after various numbers of iterations (left) or with the automatic stopping procedure (right).

Closure test The MC simulation is ideally suited to validate the self-consistency of the unfolding procedure. Since the underlying true multiplicity distribution $n_{\rm MC}(N_{\rm ch})$ of the generated collisions is known, it can be directly compared to the one obtained by unfolding the measured multiplicity distribution $n_{\rm MC}(N_{\rm ch}^{\rm meas})$. For this so-called closure test, the iterative unfolding procedure is started with a flat initial distribution (prior), i.e. without any assumption about its shape.

The left panel of Figure 3.8 shows the generated and measured multiplicity distributions together with the unfolded samples after different numbers of iterations ($N_{\text{iter}} = 3$, 10, 20, 50, and 100) for the MC simulation anchored to the example dataset. After only three iterations, the unfolded and generated distributions deviate by less than 5 %, while 50 iterations result in a nearly perfect agreement. No further improvement can be seen when using 100 iterations.

The required number of iterations for convergence strongly depends on the distribution and the chosen prior. Therefore, as discussed in Section 1.4, no fixed number



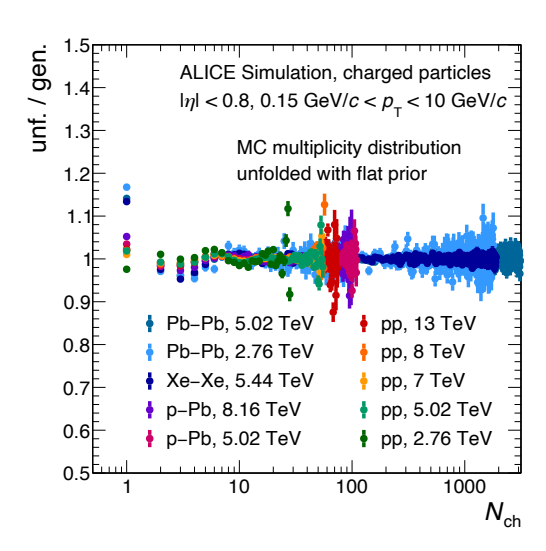


Figure 3.9: χ^2 /ndf between consecutive unfolding iterations of the simulated multiplicity distribution as a function N_{iter} (left). Ratio of the unfolded multiplicity distribution after the last iteration to the generated multiplicity distribution (right).

of iterations is used in this work. Instead, the χ^2 /ndf between the unfolded distributions of two consecutive iterations is employed as a measure for convergence and the procedure is stopped automatically once this quantity becomes less than unity. The right panel of Figure 3.8 shows the unfolded multiplicity distribution obtained using this automatic stopping procedure. In this case, the deviations between the unfolded and generated distributions are less than 2%, which shows that the unfolding method with automatic stopping produces accurate results.

The left panel of Figure 3.9 shows the χ^2/ndf as a function of the number of unfolding iterations N_{iter} for the MC simulations anchored to the ten datasets considered in this work. Fewer iterations are required to reach the convergence criterion $\chi^2/\text{ndf} < 1$ for unfolding the multiplicity distributions of p–Pb and AA collisions than for the pp datasets. This demonstrates the advantage of the automatic stopping procedure over arbitrarily choosing a fixed number of iterations.

The right panel of Figure 3.9 summarizes the corresponding ratios of the unfolded multiplicity distributions after automatic stopping to the generated multiplicity distributions. Except for $N_{\rm ch}=1$ and the highest multiplicities in each dataset, the deviations between the unfolded and generated distributions are generally below 5%. As this closure test quantifies the accuracy of the unfolding method, the deviations

shown in this figure contribute to the systematic uncertainty assigned to $P(N_{ch})$.

3.6.2 Multiplicity-dependent p_T spectra

The second part of the analysis aims to correct the raw yield of charged-particle tracks measured as a function of $p_{\rm T}^{\rm meas}$ and $N_{\rm ch}^{\rm meas}$ to obtain the $p_{\rm T}$ spectra of primary charged particles as a function of $N_{\rm ch}$ representing collisions of the fiducial event class. This 2D unfolding problem can in principle be solved with the iterative procedure described in Section 1.4, simply by using value pairs for the true $x_{\rm t} = (N_{\rm ch}, p_{\rm T})$ and measured $x_{\rm m} = (N_{\rm ch}^{\rm meas}, p_{\rm T}^{\rm meas})$ properties, respectively. Given the intended high granularity of the measurement in both $N_{\rm ch}$ and $p_{\rm T}$, a large amount of MC statistics would be required to sufficiently populate the histograms representing the efficiency, contamination, and, in particular, the smearing matrix $S(x_{\rm t}|x_{\rm m})$.

In this work, therefore, an alternative approach is used to achieve the 2D deconvolution by correcting the $N_{\rm ch}$ and $p_{\rm T}$ dimensions in sequential unfolding steps. This is possible since the probability of reconstructing a charged particle with transverse momentum $p_{\rm T}$ produced in a collision with multiplicity $N_{\rm ch}$ is affected by two fundamentally different components: On the one hand, event-level effects that are intrinsically multiplicity dependent, and on the other hand, track-level effects, that mainly depend on the particle's transverse momentum. Correcting the measured track sample for these two phenomena separately simplifies the unfolding problem. In the following these two classes of effects are outlined in more detail before the sequential unfolding approach is discussed.

Event-level effects The goal of the analysis is to measure the charged particles produced in collisions belonging to the fiducial event class as defined in Section 3.3 with a vertex located within $|V_z| < 10$ cm. On the event level, this measurement is influenced by two effects: The efficiency for measuring a collision and the contamination from background events, as previously discussed in Section 3.6.1.

In this work, the signal efficiency is defined as the ratio of the number of charged particles produced in events selected for analysis to the number of charged particles produced in all collisions of the fiducial event class with a vertex located within $|V_z| < 10 \,\mathrm{cm}$. Similarly, the fraction of measured tracks originating from collisions not

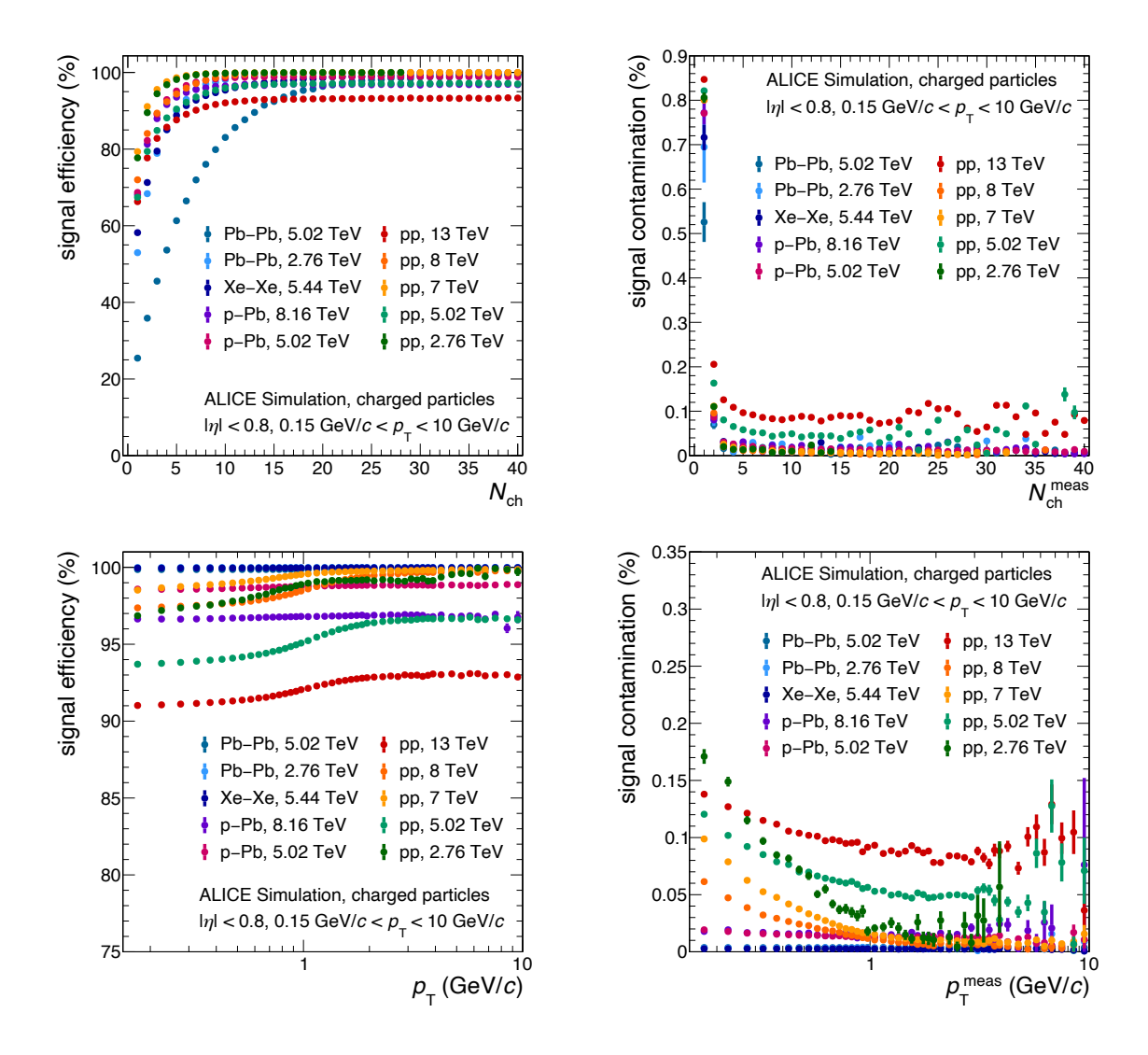
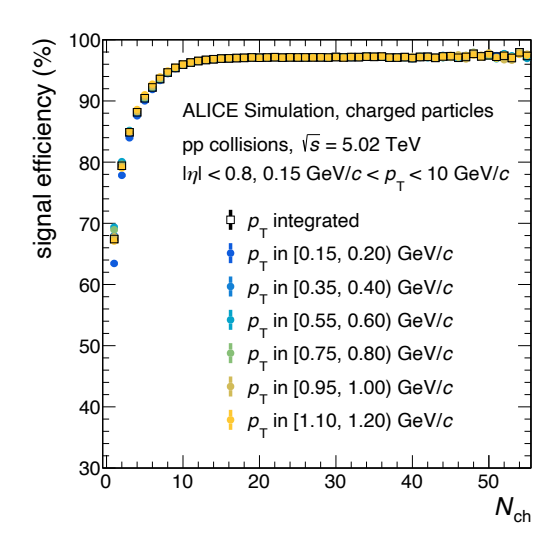


Figure 3.10: Signal efficiency (left) and signal contamination (right) as a function of multiplicity (top) and transverse momentum (bottom).

belonging to the fiducial event class or with a vertex located outside $|V_z| < 10 \,\mathrm{cm}$, is referred to as the signal contamination. Both quantities are extracted from the MC simulations. As discussed in Section 1.4, the efficiency is determined as a function of the original collision and particle properties $N_{\rm ch}$ and $p_{\rm T}$, respectively, while the contamination depends on the measured event and track properties $N_{\rm ch}^{\rm meas}$ and $p_{\rm T}^{\rm meas}$. Figure 3.10 shows the signal efficiency (left) and signal contamination (right) as a function of multiplicity (top) and transverse momentum (bottom) for all analyzed datasets.

As previously observed in Figure 3.6, the signal efficiencies shown in the left panels of Figure 3.10 do not saturate at 100% for simulations containing pileup collisions,



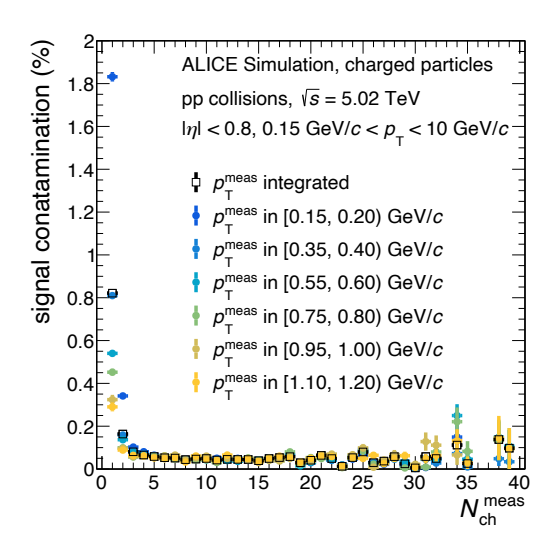


Figure 3.11: Signal efficiency (left) and signal contamination (right) as a function of multiplicity in selected transverse momentum intervals for the example dataset.

which is visible most prominently for the dataset with the highest interaction rate: pp collisions at $\sqrt{s} = 13 \,\text{TeV}$. Generally, the largest fraction of particles is lost in low-multiplicity collisions since those are affected the most by the trigger and event selection. For the five pp datasets, this rejection of predominantly low-multiplicity collisions results in a stronger reduction of the signal efficiency at low p_{T} , as shown in the bottom left panel of the figure.

The top right panel of Figure 3.10 illustrates that also the contamination from background events affects mostly low-multiplicity events. For events with only one reconstructed track, the contamination is the highest, but still below 0.9%. However, since these events overall contribute little to the measured track sample, the $p_{\rm T}$ -dependent signal contamination shown in the bottom right panel of Figure 3.10 is even smaller, below 0.2%, and completely negligible for p-Pb and AA collisions.

Since the signal efficiency and contamination are event-level effects, by definition they include all particles or tracks of a collision, and are thus intrinsically multiplicity dependent. Most of the transverse-momentum dependence observed in the bottom panels of Figure 3.10 is merely an effect of this multiplicity-dependent event-sample bias. The actual transverse-momentum dependence of the signal efficiency and signal contamination, is shown in Figure 3.11 for the example dataset as a function of $N_{\rm ch}$ and $N_{\rm ch}^{\rm meas}$, respectively. Only at the lowest multiplicities, there is a small transverse-

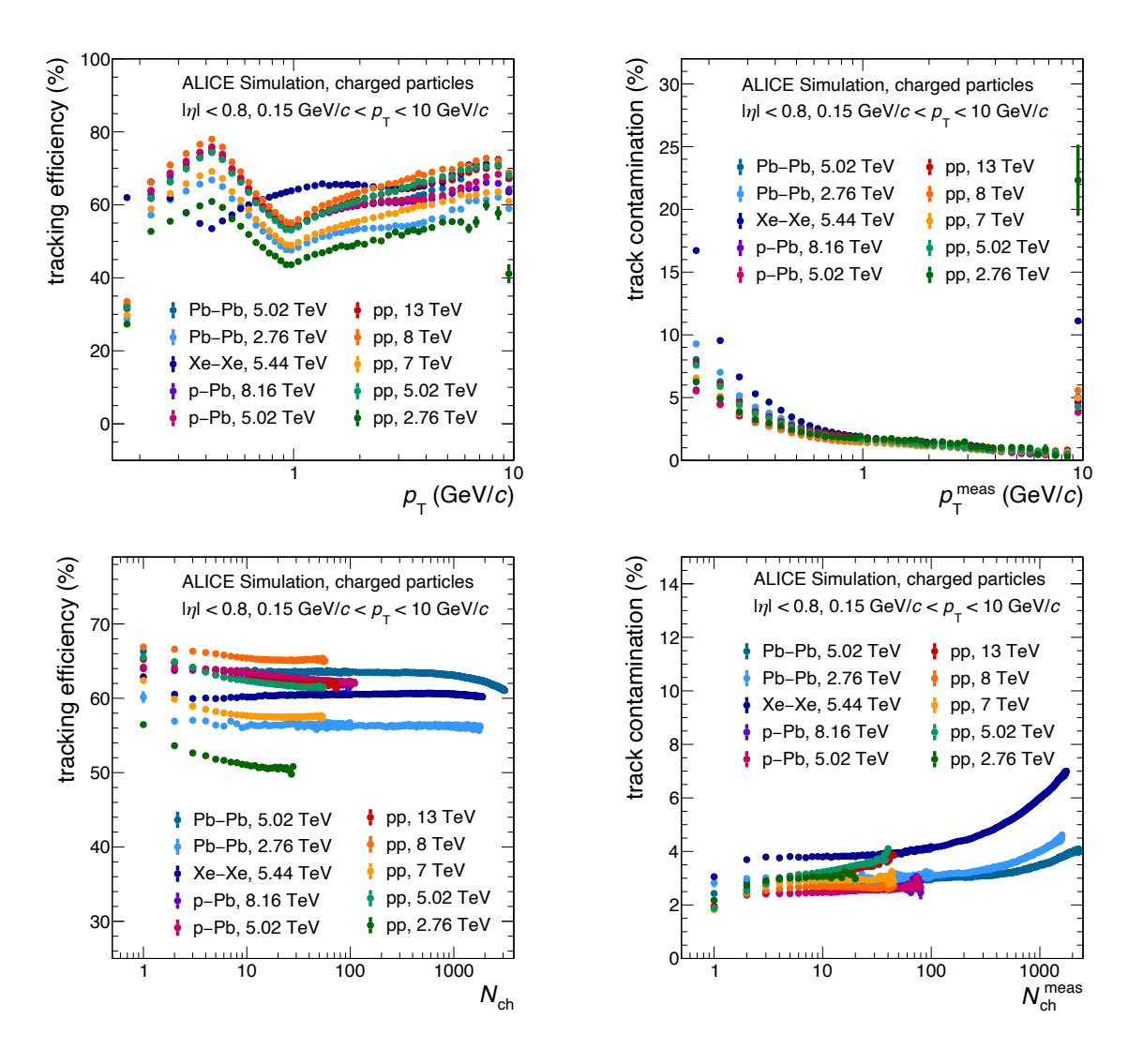


Figure 3.12: Tracking efficiency (left) and track contamination (right) as a function of transverse momentum (top) and multiplicity (bottom).

momentum dependence of both quantities.

Both the $p_{\rm T}$ -dependent signal efficiency and the signal contamination are used for the sequential unfolding procedure described at the end of this subsection.

Track-level effects The measurement of primary charged particles produced within the kinematic range $0.15\,\mathrm{GeV}/c < p_\mathrm{T} < 10\,\mathrm{GeV}/c$ and $|\eta| < 0.8$ by a collision that passes the event selection is influenced by two track-level effects: The efficiency for tracking and selecting a charged particle and the contamination of the selected track sample with background.

In this work, the tracking efficiency is defined as the ratio of the number of primary charged particles with a reconstructed track fulfilling the quality criteria described in Section 3.4 to the total number of primary charged particles produced within the considered kinematic range by an event selected for analysis. Similarly, the fraction of selected tracks originating from secondary particles or from particles produced outside the considered kinematic range is denoted as track contamination. Figure 3.12 shows the tracking efficiency (left) and track contamination (right) as a function of transverse momentum (top) and multiplicity (bottom) for all analyzed datasets.

The tracking efficiency as a function of $p_{\rm T}$ is shown in the top left panel of Figure 3.12. All datasets exhibit a similar trend and a distinct minimum around $p_{\rm T}\approx 1\,{\rm GeV}/c$. This minimum is caused by the requirement of a minimal geometric track length in the detector [64]. For the Xe–Xe dataset, the distribution is shifted towards smaller transverse momenta due to the lower magnetic field. In the highest transverse momentum interval, the efficiency decreases with respect to the previous trend since some particles are reconstructed with $p_{\rm T}^{\rm meas} \geq 10\,{\rm GeV}/c$. The lowest tracking efficiency is observed for pp collisions at $\sqrt{s}=2.76\,{\rm TeV}$, where the SDD layers are not included in the track reconstruction and acceptance holes due to inoperational ITS sectors reduce the spatial coverage of the detector. The $p_{\rm T}$ integrated tracking efficiency shown in the bottom left panel of Figure 3.12 slightly decreases as a function of $N_{\rm ch}$.

The top right panel of Figure 3.12 illustrates that the contamination of the track sample with secondary particles from weak decays and material interactions is most relevant at low transverse momenta and can reach up to 10 %, except for the low-field Xe–Xe dataset where it reaches 17 %. In the highest transverse-momentum interval, tracks originating from charged particles with $p_{\rm T} \geq 10\,{\rm GeV}/c$ contaminate the track sample by 5-22 %. The bottom right panel of Figure 3.12 shows that the $p_{\rm T}^{\rm meas}$ -integrated contamination slightly increases with $N_{\rm ch}^{\rm meas}$. Even though it is not apparent due to the logarithmic scale, for AA collisions the contamination follows a linearly rising trend with a small slope as the range is around two thousand tracks.

A slight multiplicity dependence is observed in the bottom panels of Figure 3.12 for both the tracking efficiency and track contamination. As these transverse-momentum-integrated quantities are also influenced by the shape of the underlying multiplicity-dependent transverse-momentum spectra, the actual multiplicity dependence of the

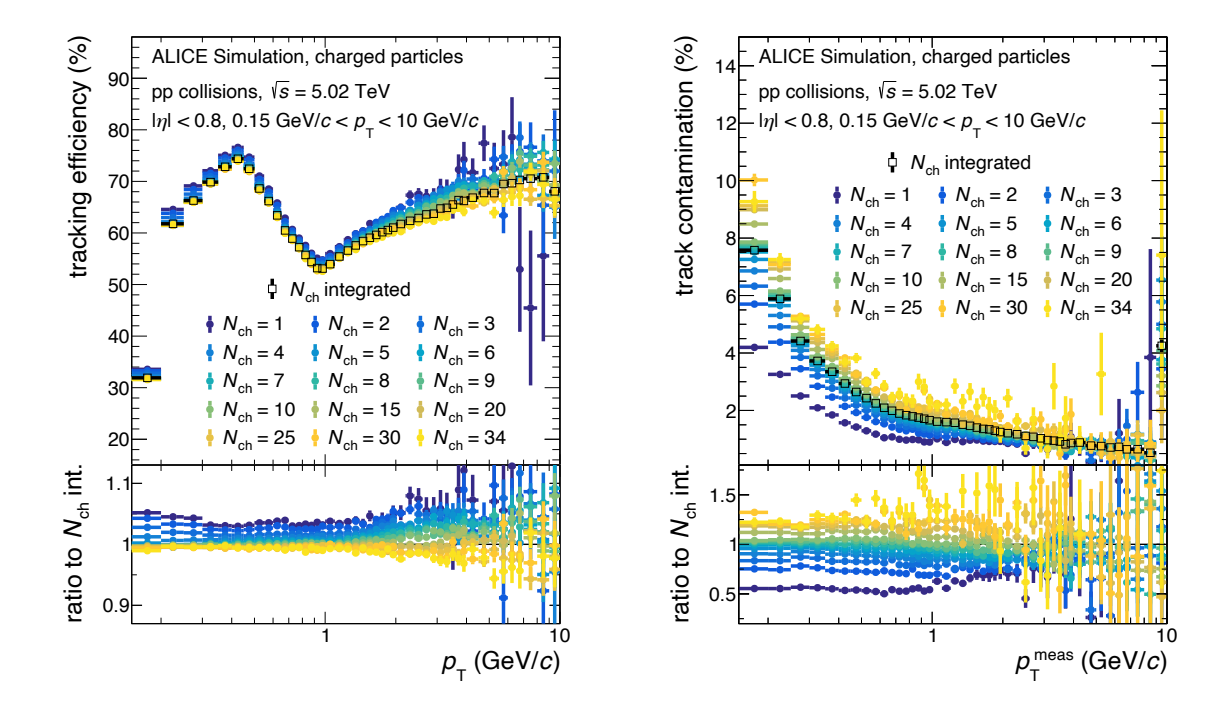


Figure 3.13: Tracking efficiency (left) and track contamination (right) as a function of transverse momentum at selected multiplicities for the example dataset.

detector response needs to be determined.

To illustrate the actual multiplicity dependence of the detector response, Figure 3.13 shows the tracking efficiency and contamination at selected multiplicities for the example dataset. Note, that here and in the following the track contamination is shown for true multiplicities $N_{\rm ch}$ instead of the measured track multiplicities $N_{\rm ch}^{\rm meas}$, since the track-level effects are considered in the second step of the sequential unfolding approach, where the multiplicity is already corrected. The black square markers indicate the $N_{\rm ch}$ -integrated efficiency and contamination, which also constitutes the reference for the ratios shown in the bottom panels. Figure 3.13 illustrates that the $p_{\rm T}$ dependence of efficiency and contamination is similar for all multiplicities. In first approximation, both quantities differ from the $N_{\rm ch}$ -integrated curves only by a multiplicity-dependent scaling factor, which is largest for the lowest multiplicities.

The sequential unfolding described in the next paragraph requires the transverse-momentum-dependent efficiency and contamination individually for each multiplicity interval. However, as apparent in Figure 3.13, for single multiplicities both quantities are prone to large statistical fluctuations. Under the assumption of an identical $p_{\rm T}$

dependence in all multiplicity intervals, the tracking efficiency $\varepsilon(p_{\rm T}, N_{\rm ch})$ and track contamination $\xi(p_{\rm T}^{\rm meas}, N_{\rm ch})$ can be approximated by multiplying their $N_{\rm ch}$ -integrated counterparts $\varepsilon(p_{\rm T})$ and $\xi(p_{\rm T}^{\rm meas})$ with multiplicity-dependent scaling factors:

$$\varepsilon(p_{\rm T}, N_{\rm ch}) = \varepsilon(p_{\rm T}) \cdot a(N_{\rm ch})$$
 (3.2)

$$\xi(p_{\mathrm{T}}^{\mathrm{meas}}, N_{\mathrm{ch}}) = \xi(p_{\mathrm{T}}^{\mathrm{meas}}) \cdot b(N_{\mathrm{ch}}) \quad . \tag{3.3}$$

To determine the scaling factor $a(N_{\rm ch})$, first the generated $N_{\rm ch}$ -dependent $p_{\rm T}$ spectra of collisions passing the event selection are folded with the $N_{\rm ch}$ -integrated $\varepsilon(p_{\rm T})$. This means that the $p_{\rm T}$ spectra are multiplied by the $\varepsilon(p_{\rm T})$ and integrated over $p_{\rm T}$ to obtain

The scaling factors $a(N_{\rm ch})$ and $b(N_{\rm ch})$ are determined in the MC simulation.

the number $n_{\text{meas}}^{\text{pseu}}(N_{\text{ch}})$ of 'pseudo-measured' charged particles. Second, this number is divided by the actual number $n_{\text{meas}}^{\text{actual}}(N_{\text{ch}})$ of measured charged particles:

$$a(N_{\rm ch}) = \frac{n_{\rm meas}^{\rm actual}(N_{\rm ch})}{n_{\rm meas}^{\rm pseu}(N_{\rm ch})} \quad . \tag{3.4}$$

The lower part of the left panel of Figure 3.14 shows $a(N_{\rm ch})$. In the upper part of the figure, the two quantities $n_{\rm meas}^{\rm actual}$ and $n_{\rm meas}^{\rm pseu}$ are visualized as the respective efficiencies, i.e. divided by the generated number of particles: $\varepsilon(N_{\rm ch})$ and $\varepsilon(N_{\rm ch})^{\rm pseu}$.

The scaling factor $b(N_{\rm ch})$ for the contamination is obtained similarly: The multiplicity-dependent measured $p_{\rm T}^{\rm meas}$ spectra of non-background events are folded with $\xi(p_{\rm T}^{\rm meas})$ to obtain the number $n_{\rm bkg}^{\rm pseu}$ of expected 'pseudo-background' tracks. This number is then divided by the actual number $n_{\rm bkg}^{\rm actual}(N_{\rm ch})$ of measured background tracks. At low multiplicities $n_{\rm bkg}^{\rm actual}(N_{\rm ch})$ is extrapolated assuming a linear relation resulting in $n_{\rm bkg}^{\rm 'actual}(N_{\rm ch})$. The ratio is calculated as:

$$b(N_{\rm ch}) = \frac{n_{\rm bkg}^{'\rm actual}(N_{\rm ch})}{n_{\rm bkg}^{\rm pseu}(N_{\rm ch})} \quad . \tag{3.5}$$

The lower part of the right panel of Figure 3.14 shows $b(N_{\rm ch})$. In the upper part of the figure, the three quantities $n_{\rm bkg}^{\rm actual}$, $n_{\rm bkg}^{\prime \rm actual}$ and $n_{\rm bkg}^{\rm pseu}$ are visualized as the respective contaminations, i.e. divided by the measured number of tracks: $\xi(N_{\rm ch})$, $\xi'(N_{\rm ch})$ and $\xi(N_{\rm ch})^{\rm pseu}$.

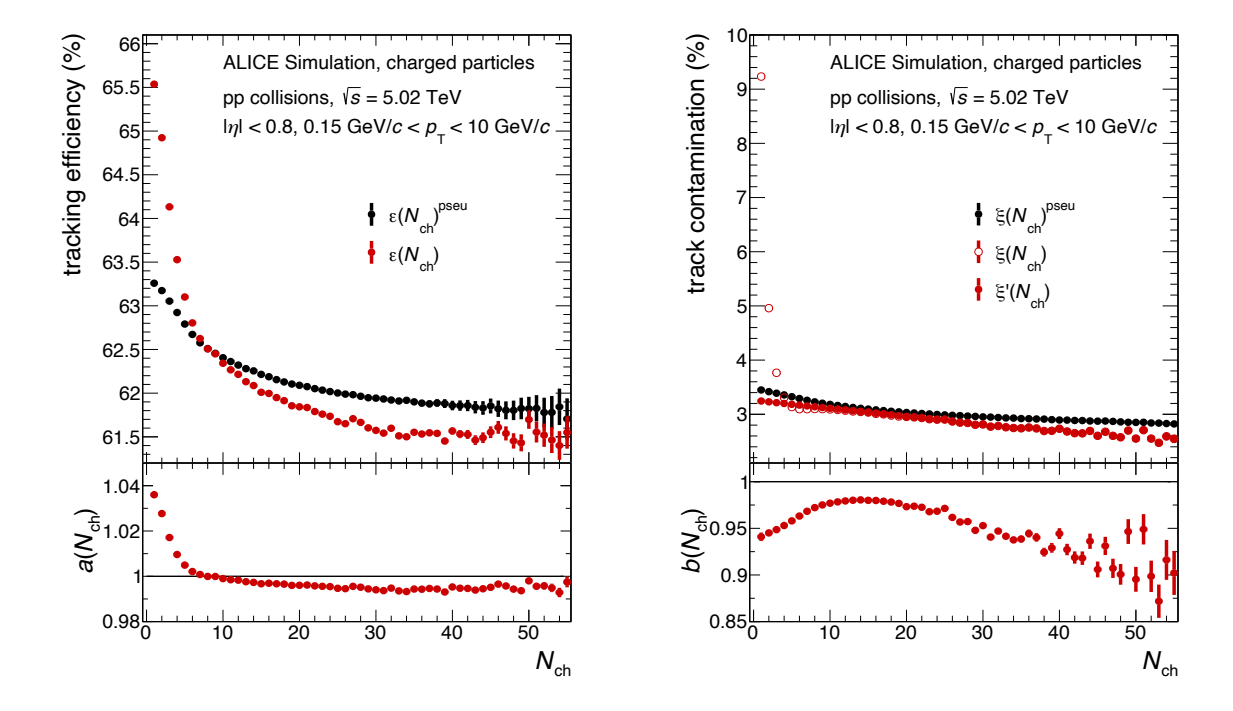


Figure 3.14: Scaling factors for the tracking efficiency (left) and contamination (right). The shown variables are defined in the text.

The constructed $\varepsilon(p_{\rm T}, N_{\rm ch})$ and $\xi(p_{\rm T}^{\rm meas}, N_{\rm ch})$ are used for the sequential unfolding described in the following paragraph.

Sequential unfolding To obtain the $p_{\rm T}$ spectra of primary charged particles as a function of $N_{\rm ch}$, the raw yield of charged-particle tracks measured as a function of $p_{\rm T}^{\rm meas}$ and $N_{\rm ch}^{\rm meas}$ has to be unfolded. The unfolding requires the previously presented event-level and track-level contamination and efficiency. Additionally, the correlation between $N_{\rm ch}$ and $N_{\rm ch}^{\rm meas}$ as well as $p_{\rm T}$ and $p_{\rm T}^{\rm meas}$ are required to account for the experimental resolution. Figure 3.15 shows the corresponding smearing matrices for the multiplicity $N_{\rm ch} \to N_{\rm ch}^{\rm meas}$ (left) and for the transverse momentum $p_{\rm T} \to p_{\rm T}^{\rm meas}$ (right). In the figure, the normalized smearing probability is denoted as $S_{\rm prim}$.

In the following explanation of the unfolding procedure, the raw yield of charged-particle tracks is called $Y_{\rm track}$, while the charged-particle yield corrected for efficiency, contamination and smearing is labelled $Y_{\rm ch}$. To achieve a 2D unfolding of $Y_{\rm track}(N_{\rm ch}^{\rm meas}, p_{\rm T}^{\rm meas})$ and obtain $Y_{\rm ch}(N_{\rm ch}, p_{\rm T})$, in this thesis, a strategy is employed that consists of two consecutive steps comprised of multiple 1D unfolding processes as described in Section 1.4. The unfolding is followed by a normalization step.

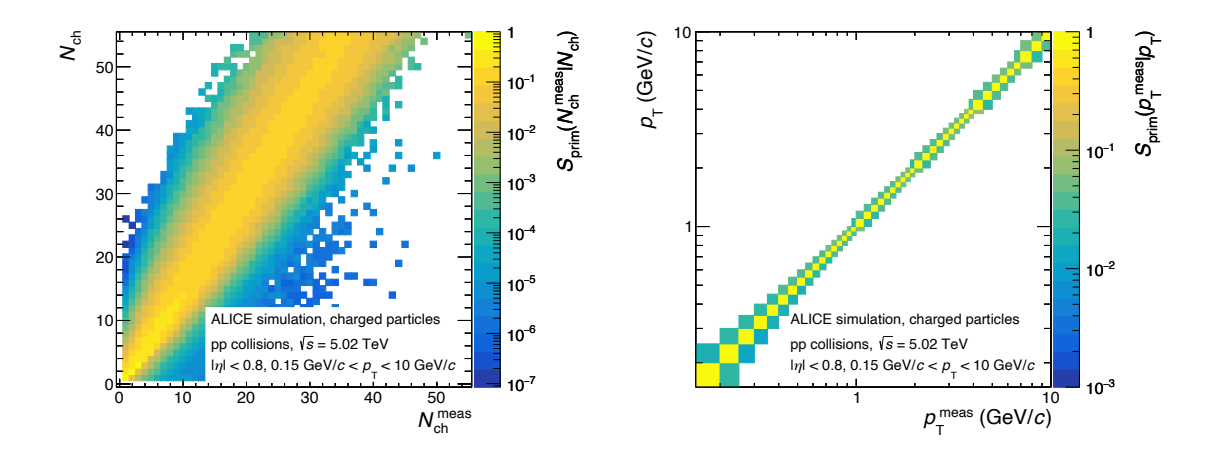


Figure 3.15: Multiplicity (left) and transverse momentum (right) smearing matrices of primary charged particles.

Figure 3.16 illustrates the three steps of the sequential unfolding method from top to bottom. The middle column shows the evolution of the 2D spectra at the different correction steps, while the left and right columns show projections of exemplary intervals on the multiplicity and transverse momentum axis, respectively.

In step ①, $Y_{\text{track}}(N_{\text{ch}}^{\text{meas}}, p_{\text{T}}^{\text{meas}})$ is corrected for event-level effects. For each $p_{\text{T}}^{\text{meas}}$ -interval, the corresponding track yield $Y_{\text{track}}(N_{\text{ch}}^{\text{meas}})|_{p_{\text{T}}^{\text{meas}}}$ is unfolded separately resulting in $Y'_{\text{track}}(N_{\text{ch}}, p_{\text{T}}^{\text{meas}})$. This unfolding uses the N_{ch} -dependent signal efficiencies and $N_{\text{ch}}^{\text{meas}}$ -dependent signal contamination of the respective $p_{\text{T}}^{\text{meas}}$ interval as well as the multiplicity smearing matrix. As a result, all measured tracks are redistributed to the proper true multiplicities N_{ch} and corrected for track losses related to the event selection as well as the contamination originating from background events.

In step ②, $Y'_{\text{track}}(N_{\text{ch}}, p_{\text{T}}^{\text{meas}})$ is corrected for the track-level effects. For each N_{ch} interval, the corresponding track yield $Y'_{\text{track}}(p_{\text{T}}^{\text{meas}})|_{N_{\text{ch}}}$ is unfolded separately resulting in $Y_{\text{ch}}(N_{\text{ch}}, p_{\text{T}})$. This unfolding uses the p_{T} -dependent tracking efficiencies and $p_{\text{T}}^{\text{meas}}$ -dependent track contaminations of the respective N_{ch} interval as well as the transverse momentum smearing matrix.

Finally, in step ③, $Y_{\rm ch}(N_{\rm ch}, p_{\rm T})$ is normalized to the number of collisions, inferred from unfolded multiplicity distribution obtained as described in Section 3.6.1. In addition, the yield is divided by the respective interval-widths $\Delta p_{\rm T}$ and $\Delta N_{\rm ch}$ as well as the pseudorapidity range $\Delta \eta = 1.6$. As a result, the double differential charged-particle production rate per collision in the fiducial event class $\frac{1}{N_{\rm evt}, N_{\rm ch} > 0} \frac{{\rm d}^3 N}{{\rm d} p_{\rm T} \, {\rm d} N_{\rm ch} \, {\rm d} \eta}$ is obtained.

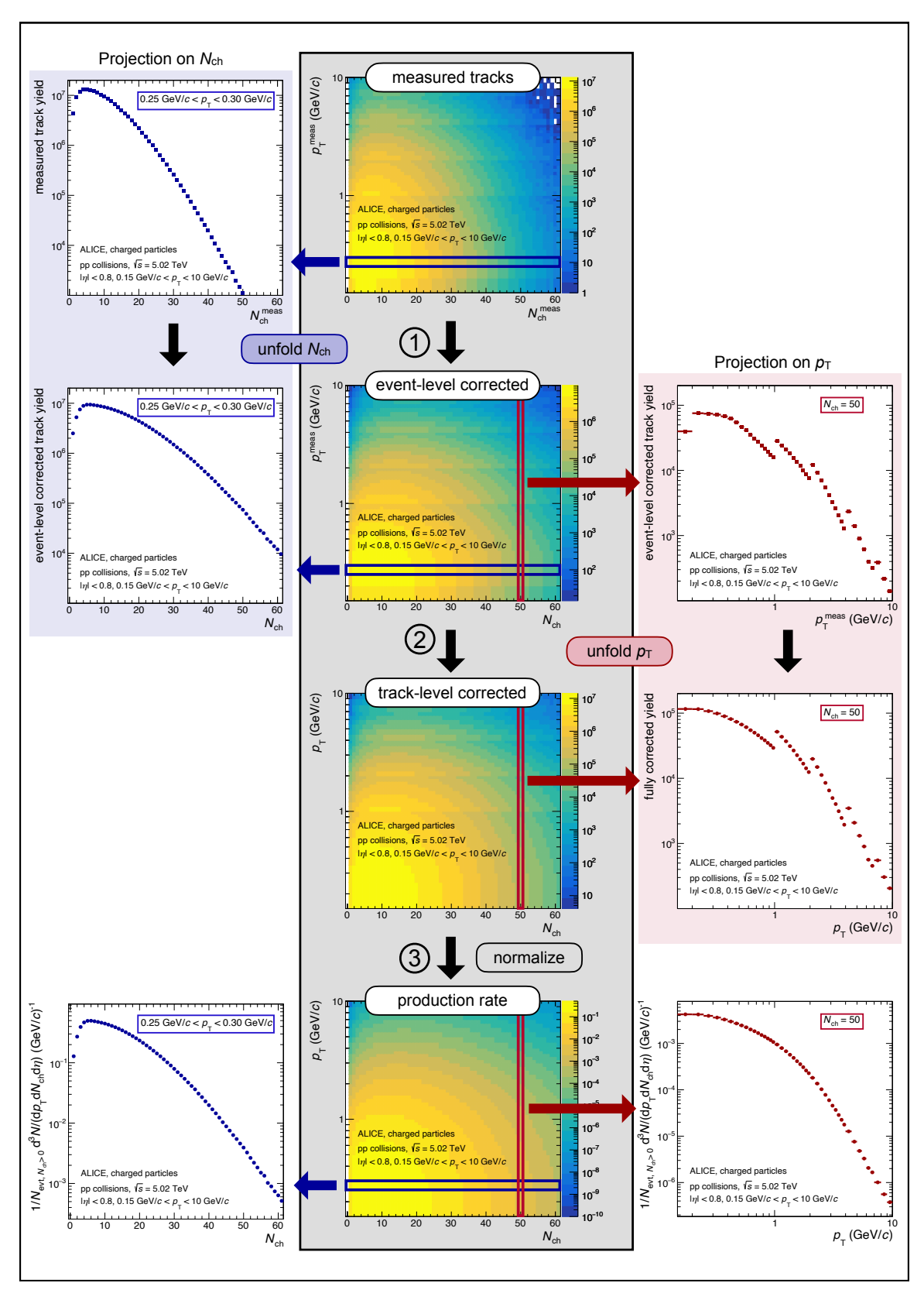


Figure 3.16: Illustration of the sequential unfolding approach showing the different stages of the 2D spectra (middle) and projections of exemplary intervals on the multiplicity (left) and transverse momentum (right) dimensions during the correction procedure.

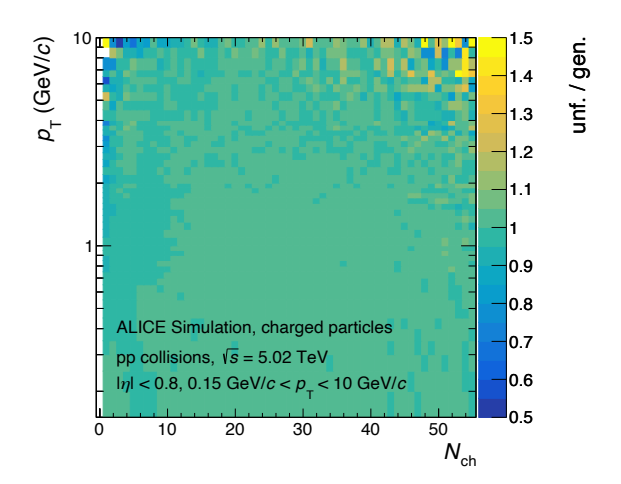


Figure 3.17: Ratio of unfolded and generated $N_{\rm ch}$ and $p_{\rm T}$ dependent charged-particle production rates of the simulation (closure test).

Closure test As for the 1D unfolding, a closure test is performed for the 2D unfolding to validate the self-consistency of the sequential unfolding procedure and estimate systematic errors from its assumptions and approximations. Figure 3.17 shows the ratio of the unfolded and generated $N_{\rm ch}$ and $p_{\rm T}$ dependent charged-particle production rates for the example dataset. The comparison illustrates that over most of the $N_{\rm ch}$ and p_{T} range the unfolded and the generated distributions agree very well with only a few minor outliers at high transverse momenta and highest or lowest multiplicities. Another way to quantify the agreement between the unfolded and generated 2D spectra is to perform a closure test for derived quantities like $\langle p_{\rm T} \rangle$ as a function of $N_{\rm ch}$. Figure 3.18 shows the projections of the 2D results on $p_{\rm T}$ and $N_{\rm ch}$ (upper panels), as well as $\langle p_{\rm T} \rangle$ and $\sigma(p_{\rm T})$ of the transverse-momentum spectra as a function of multiplicity (lower panels) for pp, p-Pb and Pb-Pb collisions at $\sqrt{s_{\rm NN}} = 5.02 \, {\rm TeV}$. Except for the $N_{\rm ch}$ -projection for the peripheral Pb-Pb collisions, there is an overall very good agreement between the unfolded and the generated distributions. This is presumably linked to the previously discussed irregularities at low multiplicities for this dataset. The deviations are in the order of 1-2 % and illustrate that the sequential unfolding procedure is particularly very well suited to extract the $p_{\rm T}$ spectra and multiplicity-dependent moments.

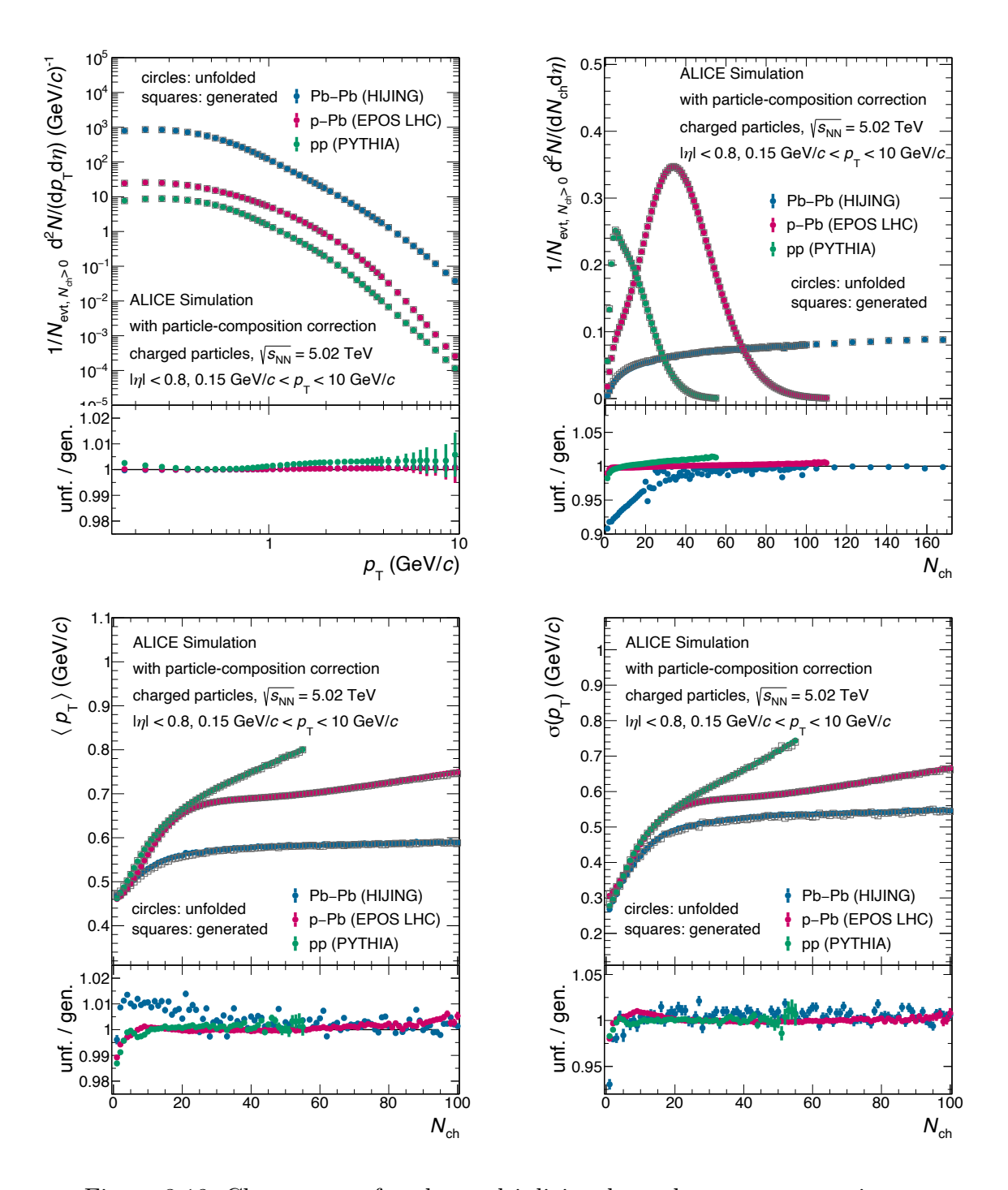


Figure 3.18: Closure test for the multiplicity-dependent $p_{\rm T}$ spectra in pp, p–Pb and Pb–Pb collisions at $\sqrt{s_{\rm NN}}=5.02\,{\rm TeV}$. The figure shows their projection on $p_{\rm T}$ (top left), $N_{\rm ch}$ (top right), as well as the derived $\langle p_{\rm T} \rangle$ (bottom left) and $\sigma(p_{\rm T})$ (bottom right) as a function of $N_{\rm ch}$.

Closure test with an alternative MC production The previously discussed closure test validates the self-consistency of the unfolding method but does not necessarily assess how the detector response, and thus the corrections applied to experimental data, are influenced by the underlying MC generator. One approach to test the effect of such potential generator bias is using an alternative MC production anchored to the same dataset but based on a different event generator that produces different particle distributions.

For the present work, this cross-check can only be performed for pp collisions at $\sqrt{s}=13\,\mathrm{TeV}$ where two anchored MC productions are available based on PYTHIA and EPOS LHC, respectively. These MC simulations are anchored to a reconstruction pass of the experimental data that is older than the one used to obtain the final results presented in this work and thus serve only for this current cross-check. Also, the differences between the PYTHIA and EPOS LHC predictions for the considered observables are small, and it is unclear to what extent any of the two generators agrees with the distributions actually underlying the experimental data. Therefore, no quantitative conclusion that could be reflected in the systematic uncertainties can be inferred from the presented cross-check.

For the following cross-check, the reconstructed tracks from PYTHIA and EPOS LHC are both unfolded with the detector response information inferred from the PYTHIA-based simulation and compared to their respective underlying generated distributions. Figure 3.19 presents the projections of the unfolded and generated multiplicity dependent transverse-momentum spectra on $p_{\rm T}$ (top left), and $N_{\rm ch}$ (top right), respectively, as well as their $\langle p_{\rm T} \rangle$ (bottom left) and $\sigma(p_{\rm T})$ (bottom right) as a function of $N_{\rm ch}$ for PYTHIA (blue) and EPOS LHC (red). The PYTHIA comparisons correspond to the closure test presented in the previous paragraph.

While there is an overall good agreement between the generated and unfolded data shown in the upper panels of the figure, the comparisons illustrate that unfolding the EPOS LHC based simulation with the PYTHIA detector response does not perfectly recover the underlying generated distributions at high $p_{\rm T}$ and $N_{\rm ch}$, respectively. However, the deviations in the $p_{\rm T}$ spectra stay below 5% and in the projection on $N_{\rm ch}$ the deviations appear mainly in low statistics regions at high multiplicity. In the lower panels of the figure, the observed deviations between the unfolded and gener-

ated EPOS LHC results are negligibly small, even though there is a difference in the trends of both observables predicted by PYTHIA and EPOS LHC. This leads to the conclusion that the results presented for $\langle p_{\rm T} \rangle$ and $\sigma(p_{\rm T})$ as a function of $N_{\rm ch}$ are stable against a bias in the generator underlying the applied corrections.

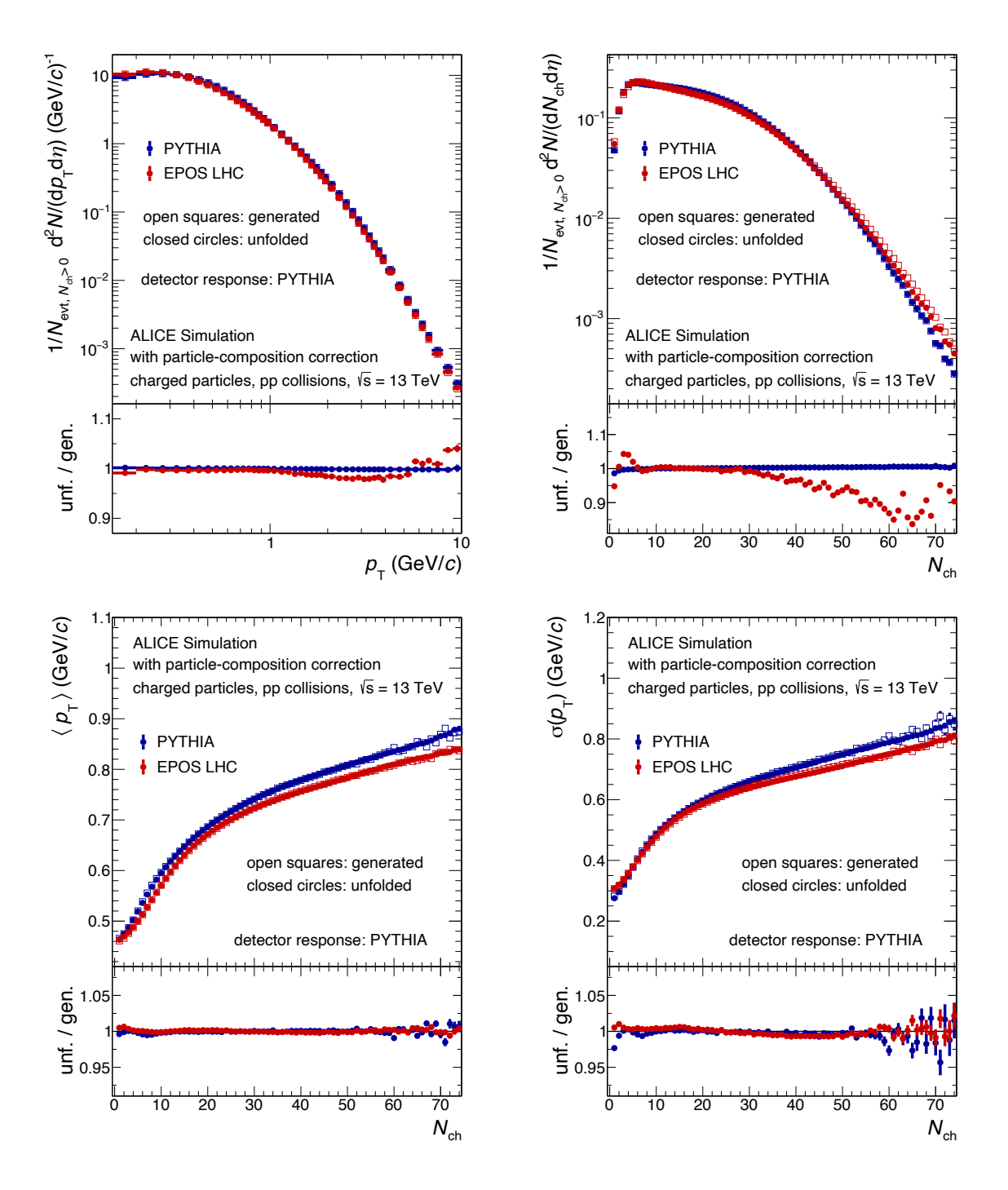


Figure 3.19: Closure test for the multiplicity-dependent $p_{\rm T}$ spectra of PYTHIA and EPOS LHC based simulations unfolded with a PYTHIA detector response. The figure shows their projection on $p_{\rm T}$ (top left), $N_{\rm ch}$ (top right), as well as the derived $\langle p_{\rm T} \rangle$ (bottom left) and $\sigma(p_{\rm T})$ (bottom right) as a function of $N_{\rm ch}$.

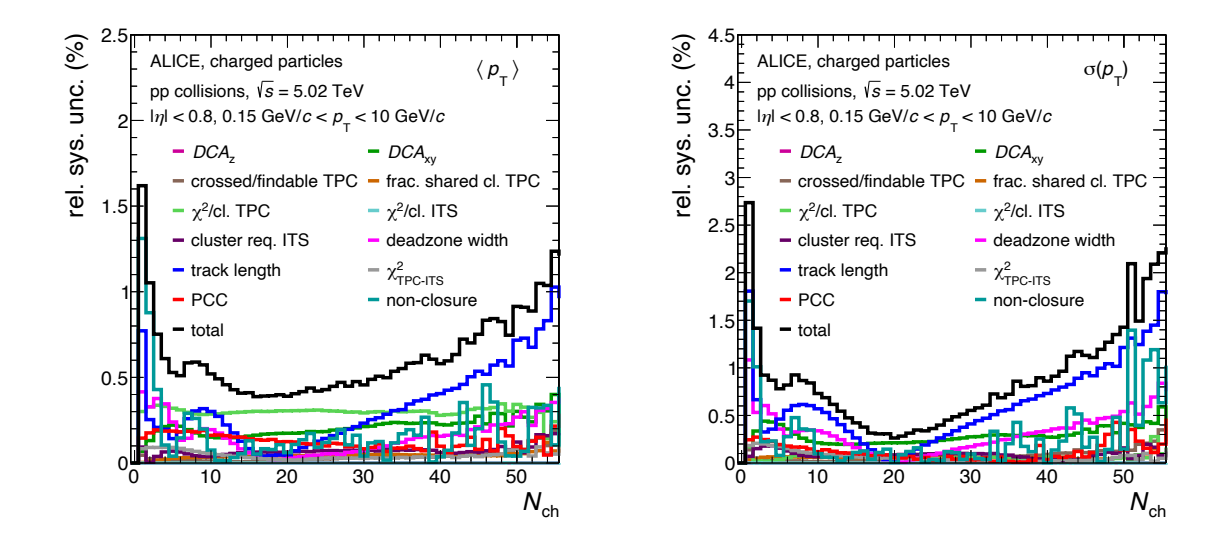


Figure 3.20: Contributions to the systematic uncertainties of $\langle p_{\rm T} \rangle$ and $\sigma(p_{\rm T})$ as a function of multiplicity for the example dataset.

3.7 Systematic uncertainties

The systematic uncertainties are estimated using the previously described MC closure tests and by testing the stability of the measurement against variations of selected analysis decisions. For each variation, the fully corrected results are calculated and their deviation from the nominal outcome contributes to the uncertainty. As a conservative estimate, all individual contributions are assumed to be fully uncorrelated and added in quadrature to obtain the total (symmetric) systematic uncertainties. The systematic uncertainties are calculated separately for each $N_{\rm ch}$ or $p_{\rm T}$ interval and are directly determined for the final observables. The uncertainties are thus not only determined for the multiplicity distribution and the $N_{\rm ch}$ dependent $p_{\rm T}$ spectra but also for derived quantities like the $\langle p_{\rm T} \rangle$ or ratios of multiplicity-dependent $p_{\rm T}$ spectra. For the ratios correlated systematic uncertainties cancel.

Figure 3.20 shows the total systematic uncertainties of $\langle p_{\rm T} \rangle$ and $\sigma(p_{\rm T})$ as a function of $N_{\rm ch}$ and their different components. The results are presented for the common example dataset. The figure highlights the strong multiplicity dependence of the systematic uncertainties which generally increase at the lowest and highest $N_{\rm ch}$ values. The following paragraphs discuss the different contributions in more detail.

Non-closure uncertainty As discussed, the MC closure test is based on dataset specific MC event generators. The systematic uncertainties are determined by comparing the unfolded reconstructed and true data of the MC simulations. This self-consistency check serves to quantify the accuracy of the unfolding method. As shown in the previous subsection, the deviations between the unfolded and generated distributions are generally small and therefore contribute little to the systematic uncertainty. However, at large multiplicities, the non-closure contribution rapidly increases due to the decreasing available MC statistics, which results in an ill-populated detector response matrix. This feature motivates the dataset-dependent restriction of the multiplicity ranges shown in this work. The non-closure contribution to the systematic uncertainties is also generally slightly larger at the lowest multiplicities.

Track-selection uncertainty Variations of the track-quality criteria constitute the dominant source of systematic uncertainty. In the analysis, the track-quality criteria are applied both to data and MC simulation. For a perfect MC simulation, the fully corrected results do not depend on the employed selection criteria. Once the MC simulation differs from a perfect description of the experimental data, the track-quality criteria would influence the data and MC simulation differently and by such, when correcting the data with the MC simulation influence the final result. The track quality requirements as well as their respective variations are listed in Table 3 and are equivalent to the ones used in Refs. [34, 48]. Most selections are varied to a lower and a higher threshold compared to the nominal setting. In these cases, the largest deviation from the nominal result is used as their contribution to the systematic uncertainty. In general, the moments of the multiplicity-dependent $p_{\rm T}$ spectra are very stable against variations of the track selections.

Particle-composition uncertainty The particle-composition correction (PCC) re-weights the particle abundances produced by the MC event generator. It relies on measured multiplicity-dependent transverse-momentum spectra of various particle species. These spectra cover different $p_{\rm T}$ ranges, which often start above the minimal transverse momentum considered in this work and thus need to be extrapolated. To estimate the systematic uncertainty related to the PCC, the measured $p_{\rm T}$ spectra of the individual particles are either shifted to the lower or upper edge of their sys-

tematic uncertainty. Both for the nominal and the shifted data points, the transverse-momentum spectra are extrapolated down to $p_{\rm T}=0.15\,{\rm GeV}/c$ using three different functions. An ALICE-internal document [91] provides a detailed description of the PCC, the input data and the functions used for the parametrization.

In total, this approach results in a set of nominal weights for adjusting the particle abundances of the MC simulation and 21 variations thereof. The variations are used to determine the uncertainty of the weights, defined as the RMS of their deviations from the nominal values. These PCC weight uncertainties are propagated to the fully corrected results of this work by shifting the nominal weights once to the upper and once to the lower edges of their uncertainties. The largest observed deviation from the nominal results is assigned as the corresponding uncertainty.

Normalization uncertainty For the unfolded multiplicity-dependent $p_{\rm T}$ spectra, an additional systematic uncertainty quantifies the accuracy of the absolute normalization in each $N_{\rm ch}$ interval. Since the $p_{\rm T}$ spectra are defined within the same kinematic range as the charged-particle multiplicity, it is possible to directly check if the integral of charged particles per collision in an unfolded $p_{\rm T}$ spectrum at a given $N_{\rm ch}$

$$I_{N_{\rm ch}}^{\rm 2D} = \frac{1}{N_{\rm evt}, N_{\rm ch} > 0} \left. \sum_{p_{\rm T}} \frac{\mathrm{d}^3 N}{\mathrm{d}p_{\rm T} \,\mathrm{d}\eta \,\mathrm{d}N_{\rm ch}} \Delta p_{\rm T} \,\Delta \eta \right|_{N_{\rm ch}}$$
(3.6)

is consistent with the expectation derived from the independently obtained multiplicity distribution

$$I_{N_{\rm ch}}^{\rm 1D} = P(N_{\rm ch}) N_{\rm ch} \Delta N_{\rm ch}$$
 (3.7)

The ratio $R = I_{N_{\rm ch}}^{\rm 2D}/I_{N_{\rm ch}}^{\rm 1D}$ quantifies how well the 2D sequential unfolding of the $p_{\rm T}$ spectra agrees with the more straightforward 1D unfolding of the $N_{\rm ch}$ distribution. The advantage of this consistency check is that, as opposed to the closure tests shown in the previous subsection, it can be carried out not only for the MC simulation but also directly for the unfolded experimental data. Figure 3.21 displays R for all ten analyzed MC simulations (left) and experimental measurements (right). The MC comparisons reveal an almost perfect consistency with variations within 1% between the two unfolding procedures. A larger disagreement of up to 10% is observed for the peripheral Pb–Pb collisions at $\sqrt{s_{\rm NN}} = 5.02\,{\rm TeV}$ as expected from the closure test

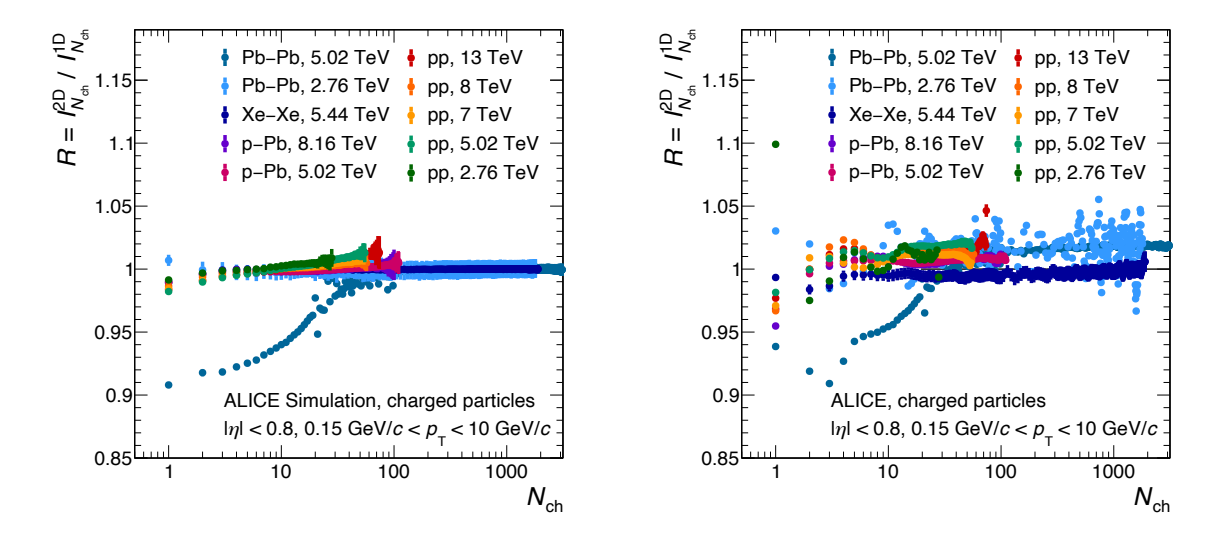


Figure 3.21: Ratio of the number of charged particles per event inferred from the 2D-unfolded $N_{\rm ch}$ -dependent $p_{\rm T}$ spectra to the expectation from the 1D-unfolded multiplicity distributions for the analyzed MC simulations (left) and experimental measurements (right).

shown in the top right panel of Figure 3.18. For the experimental results shown in the right panel of Figure 3.21, the agreement is slightly worse than for the MC simulations, but the deviations are for the most part still below 5%. The observed differences are assigned as purely $N_{\rm ch}$ -dependent systematic uncertainties of the unfolded $p_{\rm T}$ spectra in the respective multiplicity intervals.

Total uncertainties Figure 3.22 summarizes the total systematic uncertainties for the multiplicity distributions (top left), $p_{\rm T}$ spectra (top right) as well as $\langle p_{\rm T} \rangle$ (bottom left) and $\sigma(p_{\rm T})$ (bottom right) as a function of $N_{\rm ch}$ for all analyzed datasets.

Except for $N_{\rm ch}=1$, the precision of the multiplicity distributions is better than 5% in the low $N_{\rm ch}$ range representing most of the collisions, but continuously worsens for high-multiplicities. The uncertainties assigned to the $p_{\rm T}$ spectra also stay well below 5%, except for the two $\sqrt{s_{\rm NN}}=2.76\,{\rm TeV}$ datasets where they reach up to 14% at the highest transverse momenta. The systematic uncertainty of $\langle p_{\rm T}\rangle$ amounts to less than 2% over the entire reported $N_{\rm ch}$ range. For the width of the spectra, $\sigma(p_{\rm T})$, the precision is slightly worse than for $\langle p_{\rm T}\rangle$, but mostly well below 3%.

All multiplicity-dependent observables in AA collisions show minor bin-by-bin fluctuations of the overall small systematic uncertainties. Though this is no desirable

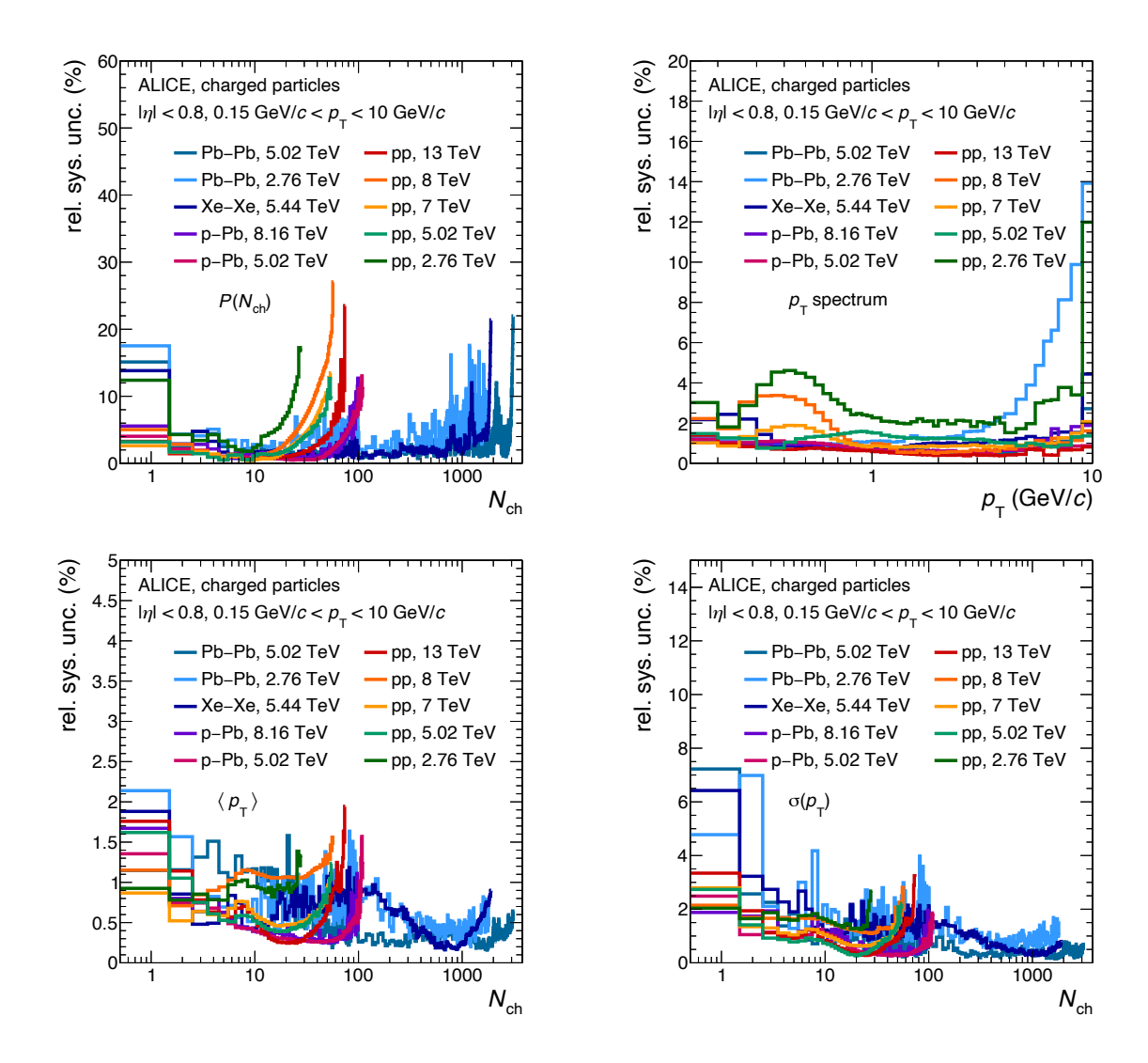


Figure 3.22: Total systematic uncertainties of the multiplicity distribution (top left), the $p_{\rm T}$ spectrum (top right) as well as $\langle p_{\rm T} \rangle$ (bottom left) and $\sigma(p_{\rm T})$ (bottom right) as a function of multiplicity.

feature, no smoothing is performed in order to adhere to a clearly defined method for determining the systematic uncertainties.

In general, the precision of the present measurement surpasses previous publications of comparable observables, e.g. Ref. [38], as a result of the more advanced analysis method employed in this work, the better quality of the newer data reconstruction passes, and the improved MC simulations.

4 Results and discussion

This section discusses the final results of the present work most of which are published in Ref. [1]. All data points are made available on the HEPData [92] archive to enable future analyses based on these measurements.

In the following, the experimental results are presented with a focus on comparing the ten considered collision scenarios. The measured observables are then compared to previously published results and available theoretical predictions. These main results of the thesis are complemented by two supplementary studies discussed at the end of this section.

4.1 Experimental results

The present work covers pp collisions at $\sqrt{s}=2.76\,\mathrm{TeV}$, 5.02 TeV, 7 TeV, 8 TeV and 13 TeV, p–Pb collisions at $\sqrt{s_\mathrm{NN}}=5.02\,\mathrm{TeV}$ and 8.16 TeV, Xe–Xe collisions at $\sqrt{s_\mathrm{NN}}=5.44\,\mathrm{TeV}$, as well as Pb–Pb collisions at $\sqrt{s_\mathrm{NN}}=2.76\,\mathrm{TeV}$ and 5.02 TeV. Charged particles are measured within $|\eta|<0.8$ and 0.15 GeV/ $c< p_\mathrm{T}<10\,\mathrm{GeV}/c$. All results are exclusively reported for collisions with $N_\mathrm{ch}>0$, where the multiplicity N_ch is defined as the number of charged particles within this kinematic range. This corresponds to the fiducial event class discussed in Section 3.3. Most of the measurements are presented in single multiplicity intervals, except for AA collisions above $N_\mathrm{ch}=100$, where their width is increased to $\Delta N_\mathrm{ch}=9$. All multiplicity-dependent results are shown only up to a dataset-specific maximum N_ch value, as the systematic uncertainties increase drastically towards higher multiplicities. Particularly in case of the AA collisions this restriction of the multiplicity ranges implies that the results are not shown for the most central collisions.

Global event properties The first results presented in this work are the multiplicity distributions and the multiplicity-integrated $p_{\rm T}$ spectra, which are compared among the ten different collision scenarios. Figure 4.1 displays the probability density distribution $P(N_{\rm ch})$ of the multiplicities (left), and the multiplicity-integrated $p_{\rm T}$ spectra (right) for all analyzed datasets. $P(N_{\rm ch})$ reaches a maximum around $N_{\rm ch} \approx 2$ before falling off steeply over several orders of magnitude. While the maximum number of produced charged particles is well below 100 for pp collisions, in p-Pb collisions

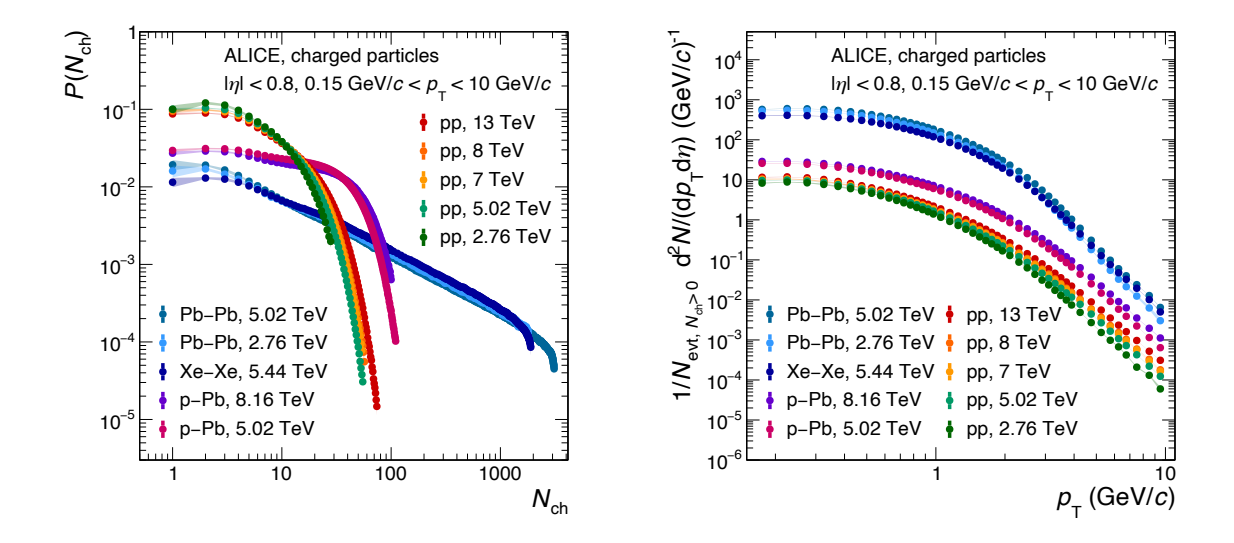


Figure 4.1: Multiplicity distributions (left) and multiplicity-integrated $p_{\rm T}$ spectra (right) for the ten datasets considered in this work.

the multiplicity extends up to almost 200 and can reach 3000 in AA collisions. The maximal range depends both on the collision energy and the number of colliding nucleons. Therefore, the multiplicity reach is smaller in Xe–Xe (A=129) compared to Pb–Pb (A=208) collisions despite the slightly higher center-of-mass energy per nucleon pair.

Similarly, the ordering of the $p_{\rm T}$ spectra shows that the number of particles produced per collision depends on both the system size and energy. This becomes particularly apparent for Xe–Xe collisions, where due to the smaller number of participating nucleons fewer low- $p_{\rm T}$ particles are produced than in Pb–Pb collisions at $\sqrt{s_{\rm NN}}=2.76\,{\rm TeV}$, while more particles are produced at high $p_{\rm T}$ as a result of the larger center-of-mass energy per nucleon pair. Generally, AA collisions exhibit significantly flatter $p_{\rm T}$ spectra than pp collisions, a feature that is also present, though less pronounced, in p–Pb collisions. In particular for pp and p–Pb collisions, the occurrence probability for high-multiplicity events as well as the particle production rate at high $p_{\rm T}$ increase with center-of-mass energy, which can be attributed to the enhanced possibility for large momentum transfers in the initial parton scattering processes.

On the basis of the $P(N_{\rm ch})$ and the multiplicity-integrated $p_{\rm T}$ spectra, four global event properties are determined for each dataset: the mean $\langle N_{\rm ch} \rangle$ and standard deviation $\sigma(N_{\rm ch})$ of $P(N_{\rm ch})$ as well as the mean $\langle p_{\rm T} \rangle_{\rm incl}$ and standard deviation $\sigma(p_{\rm T})_{\rm incl}$ of the multiplicity-integrated $p_{\rm T}$ spectra. These global event properties are summa-

	/2	/ N 7 \	$\sigma(N)$	/m \	5 (n)
	$\sqrt{s_{ m NN}}$	$\langle N_{ m ch} angle$	$\sigma(N_{ m ch})$	$\langle p_{ m T} angle_{ m incl}$	$\sigma(p_{\mathrm{T}})_{\mathrm{incl}}$
	(TeV)			(MeV/c)	(MeV/c)
pp	2.76	7.18 ± 0.24	6.05 ± 0.17	589.7 ± 2.6	483 ± 4
	5.02	8.21 ± 0.10	7.20 ± 0.08	612.2 ± 2.7	520.2 ± 1.0
	7	8.86 ± 0.12	7.88 ± 0.11	627.1 ± 1.6	541.3 ± 2.1
	8	9.05 ± 0.22	8.11 ± 0.18	631 ± 5	547 ± 4
	13	10.31 ± 0.09	9.48 ± 0.07	654.0 ± 1.0	582.4 ± 0.9
p–Pb	5.02	25.51 ± 0.25	19.79 ± 0.20	711.9 ± 1.3	619.8 ± 1.1
	8.16	29.56 ± 0.26	23.13 ± 0.23	741.5 ± 1.4	657.0 ± 1.3
Xe-Xe	5.44	458 ± 10	514 ± 13	717.4 ± 1.8	568.4 ± 1.4
Pb–Pb	2.76	573 ± 9	667 ± 12	687.3 ± 1.3	528.0 ± 1.7
	5.02	682 ± 13	819 ± 16	724.1 ± 1.1	564.9 ± 1.0

Table 4: Global event properties of the analyzed datasets with corresponding systematic uncertainties. All values are calculated for the whole multiplicity range.

rized in Table 4 and constitute a crucial input for the following studies comparing charged-particle production among different collision scenarios.

Evolution of $p_{\rm T}$ spectra with multiplicity In addition to the previously discussed multiplicity-integrated $p_{\rm T}$ spectra, the sequential unfolding approach applied in this work enables the measurement of multiplicity-differential $p_{\rm T}$ spectra in fine $N_{\rm ch}$ intervals. To compare the evolution of the spectral shape with multiplicity between the different collision scenarios, the moments of these $p_{\rm T}$ spectra are calculated. Figure 4.2 shows the mean $\langle p_{\rm T} \rangle$ (left) and standard deviation $\sigma(p_{\rm T})$ (right) of the multiplicity-dependent $p_{\rm T}$ spectra as a function of $N_{\rm ch}$ for all datasets. While the upper panels illustrate the full multiplicity range in a logarithmic scale, the lower panels focus on the $N_{\rm ch} \leq 100$ range.

After an initial similarity of the charged-particle final state at the lowest multiplicities, first the AA collisions and then the p-Pb collisions diverge from the trend observed for pp collisions. The similarity at low $N_{\rm ch}$ might be due to the small number of nucleons participating in the scattering of peripheral p-Pb or AA collisions. At higher $N_{\rm ch}$, for each collision system both the $\langle p_{\rm T} \rangle$ and $\sigma(p_{\rm T})$ increase with center-of-mass energy. Generally, in all datasets an initial fast rise of the two observables with $N_{\rm ch}$ is followed by an increase with reduced slope. For $\sigma(p_{\rm T})$ in AA collisions this second slope is almost zero, meaning that the width of the spectra stays constant over most of the

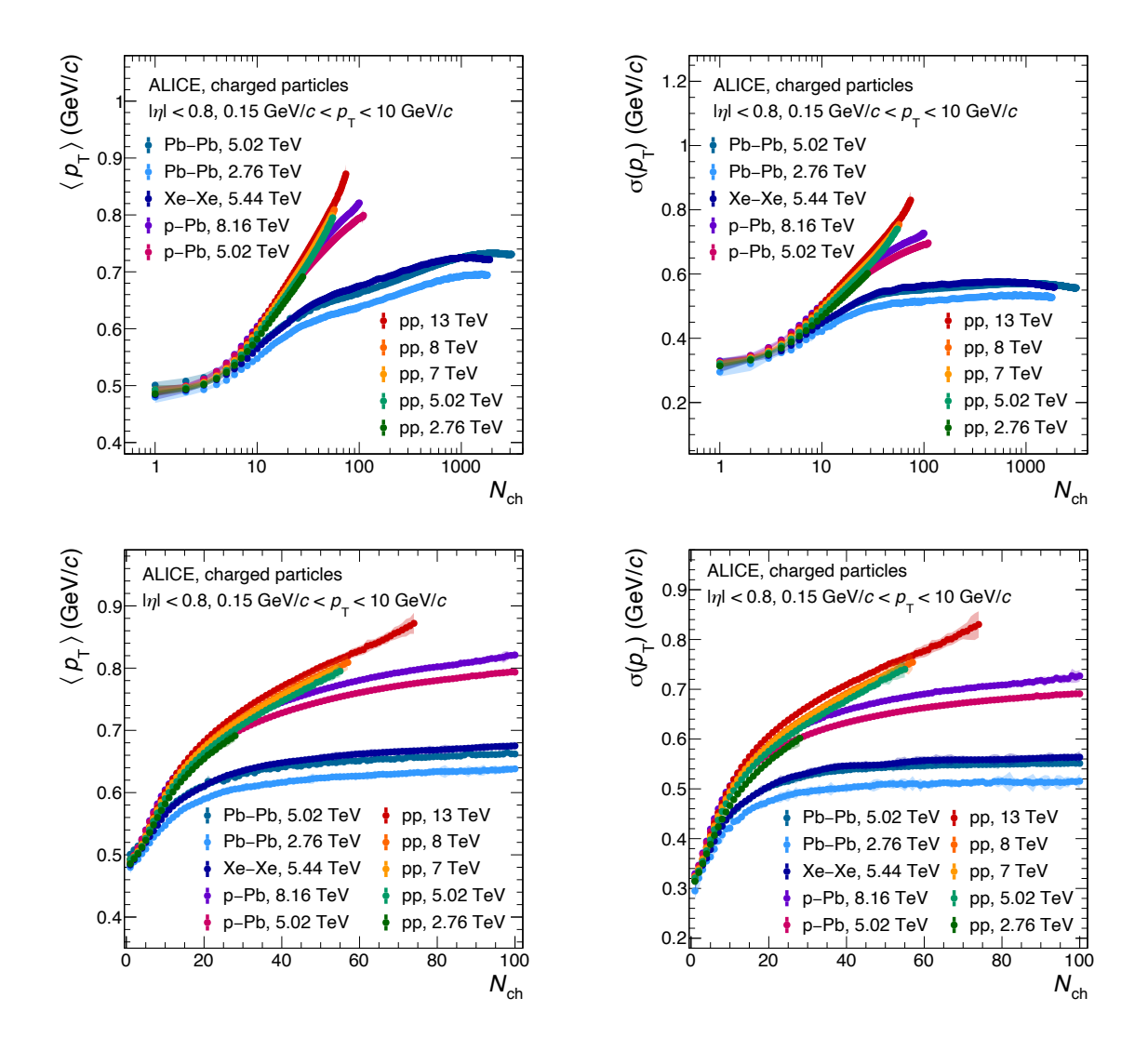


Figure 4.2: Mean $\langle p_{\rm T} \rangle$ (left) and standard deviation $\sigma(p_{\rm T})$ (right) of the multiplicity-dependent $p_{\rm T}$ spectra for the full $N_{\rm ch}$ range in logarithmic scale (top) and for $N_{\rm ch} \leq 100$ in linear scale (bottom).

multiplicity range.

To visualize the relation between $\langle p_{\rm T} \rangle$ and $\sigma(p_{\rm T})$, Figure 4.3 shows the relative standard deviation $\sigma(p_{\rm T})/\langle p_{\rm T} \rangle$ as a function of $N_{\rm ch}$. The increasing trend of $\sigma(p_{\rm T})/\langle p_{\rm T} \rangle$ in pp collisions illustrates that the transverse-momentum spectra broaden faster than $\langle p_{\rm T} \rangle$ rises with multiplicity. At low multiplicities, the larger collision systems follow a similar trend. The $\sigma(p_{\rm T})/\langle p_{\rm T} \rangle$ in p-Pb collisions saturates at a constant value, indicating that the width and mean of the spectra rise at the same rate with $N_{\rm ch}$. In AA collisions at higher multiplicities $\sigma(p_{\rm T})/\langle p_{\rm T} \rangle$ decreases as the width of the spectra remains constant while their mean continues to rise slowly. This decrease of the relative standard spectra remains constant while their mean continues to rise slowly.

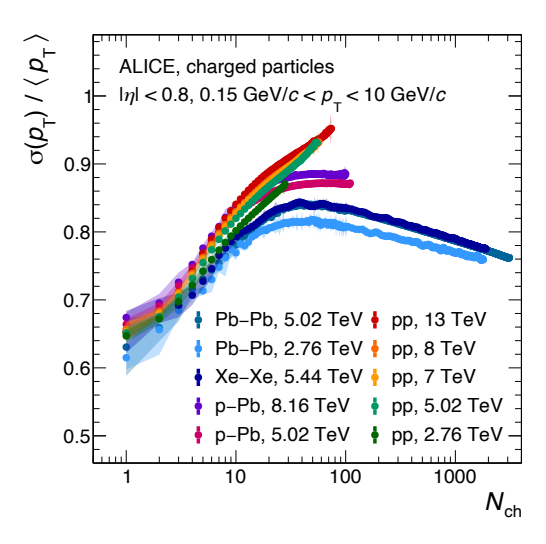


Figure 4.3: Relative standard deviation $\sigma(p_{\rm T})/\langle p_{\rm T}\rangle$ of the $p_{\rm T}$ spectra as a function of multiplicity.

tive spread around the mean is unique to AA collisions and could be a consequence of radial flow driving the low momentum particles towards higher $p_{\rm T}$ and parton energy loss simultaneously reducing the particle yield at high transverse momenta.

Relative multiplicity To further investigate similarities between different collision systems and center-of-mass energies, the multiplicity-dependent measurements presented in this thesis are expressed in terms of the relative multiplicity $N_{\rm ch}/\langle N_{\rm ch} \rangle$. This quantity represents a classifier for relative event activity, similar to the widely used multiplicity percentile MP. This multiplicity percentile categorizes an event in terms of the fraction of collisions with the highest multiplicities it belongs to:

$$MP(N_{\rm ch}) = 100 \cdot \int_{N'_{\rm ch} = N_{\rm ch}}^{\infty} P(N'_{\rm ch}) \, dN'_{\rm ch} ,$$
 (4.1)

which corresponds to the definition of centrality in AA collisions. In this work, MP is calculated using the previously shown probability density $P(N_{\rm ch})$ of the multiplicity. Figure 4.4 illustrates the relation between the two relative event activity classifiers MP and $N_{\rm ch}/\langle N_{\rm ch} \rangle$. For each collision system (pp, p–Pb, and AA) the curves follow a unique trend that is approximately independent of the center-of-mass energy. In all ten datasets, collisions producing the average number of particles, i.e. with $N_{\rm ch}/\langle N_{\rm ch} \rangle = 1$, correspond to a multiplicity percentile in the range of 35-45 %. All results presented in

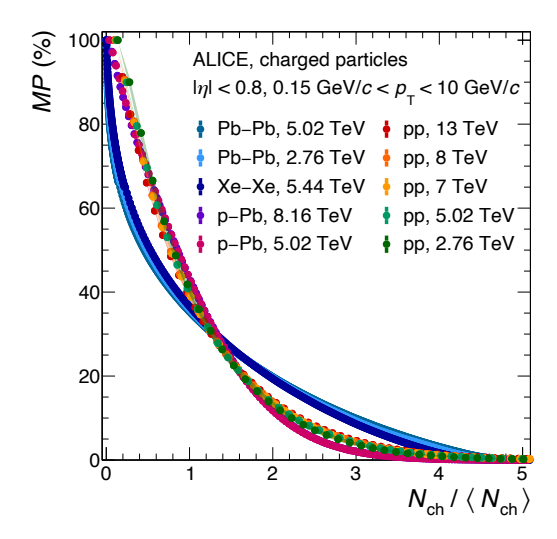


Figure 4.4: Relation of the multiplicity percentile MP and the relative multiplicity $N_{\rm ch}/\langle N_{\rm ch}\rangle$ for the ten datasets considered in this work.

the following are exclusively shown as a function of $N_{\rm ch}/\langle N_{\rm ch} \rangle$ and can be converted to MP by means of the relation presented in Figure 4.4.

The probability density $P(N_{\rm ch}/\langle N_{\rm ch}\rangle)$ of the relative multiplicity can be calculated from the frequency distribution $n(N_{\rm ch})$ of collisions within the chosen multiplicity intervals $\Delta N_{\rm ch}$. In contrast to the definition of $P(N_{\rm ch})$ shown in Equation (3.1), the interval widths of $P(N_{\rm ch}/\langle N_{\rm ch}\rangle)$ are scaled by $1/\langle N_{\rm ch}\rangle$:

$$P(N_{\rm ch}/\langle N_{\rm ch}\rangle) = \frac{1}{\Delta N_{\rm ch}/\langle N_{\rm ch}\rangle} \frac{n(N_{\rm ch})}{\sum_{N'_{\rm ch}} n(N'_{\rm ch})} = \langle N_{\rm ch}\rangle P(N_{\rm ch}) \quad . \tag{4.2}$$

This equation further illustrates the equivalence of $P(N_{\rm ch}/\langle N_{\rm ch}\rangle)$ and the Koba-Nielsen-Olesen (KNO) scaling form $\langle N_{\rm ch}\rangle P(N_{\rm ch})$ discussed in Section 1.3.1, which is used to transform multiplicity distributions to an approximately energy-independent form. Therefore, the following studies of $P(N_{\rm ch}/\langle N_{\rm ch}\rangle)$ allow to test the validity of KNO-scaling for the results presented in this work.

The top left panel of Figure 4.5 displays these KNO-scaled multiplicity distributions for all datasets. The distributions follow different trends for pp, p–Pb and AA collisions, but are similar for the different energies within each collision system as $\langle N_{\rm ch} \rangle$ increases with $\sqrt{s_{\rm NN}}$. Figure 4.5 also shows the ratios of the KNO-scaled multiplicity distributions for pp (top right), p–Pb (bottom left) and AA (bottom right) collisions at various center-of-mass energies relative to the results at $\sqrt{s}=13\,{\rm TeV}$, $\sqrt{s_{\rm NN}}=8.16\,{\rm TeV}$ and

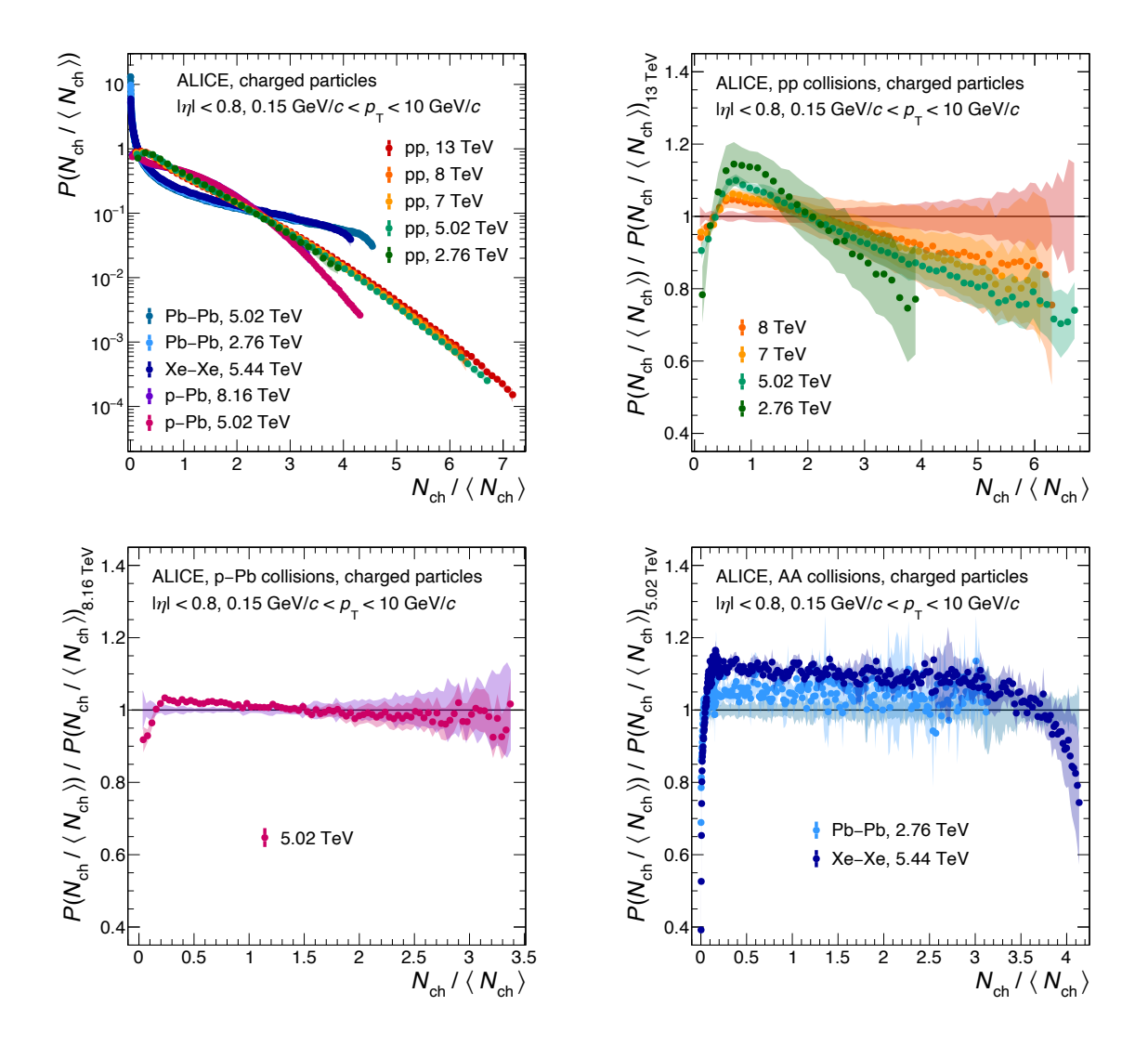


Figure 4.5: KNO-scaled multiplicity distributions (top left) and their ratio to reference energies for pp (top right), p–Pb (bottom left) and AA (bottom right) collisions.

 $\sqrt{s_{\mathrm{NN}}} = 5.02\,\mathrm{TeV}$, respectively. Since these ratios are calculated using interpolations of the reference distributions, the systematic uncertainties of the latter are not propagated but instead indicated as semi-transparent bands around unity. The ratios show that the KNO-scaled distributions for pp and AA collisions agree within 20% over most of the $N_{\mathrm{ch}}/\langle N_{\mathrm{ch}} \rangle$ range, while the results for the two p–Pb energies are in even better agreement with deviations below 10%.

As previous studies primarily focused on e^+e^- , $p\bar{p}$ and pp collisions, these results provide the first insight into the applicability of KNO scaling of multiplicity distributions in larger collision systems.

Evolution of $p_{\rm T}$ spectra with relative multiplicity Complementary to the previous study of the probability density $P(N_{\rm ch}/\langle N_{\rm ch}\rangle)$, the evolution of the $p_{\rm T}$ spectra with $N_{\rm ch}/\langle N_{\rm ch}\rangle$ is investigated. To enable comparisons between the different center-of-mass energies of a collision system, the $p_{\rm T}$ spectra are studied in intervals of the relative multiplicity. Since the average multiplicity $\langle N_{\rm ch}\rangle$ differs between the different center-of-mass energies, these intervals in relative multiplicity translate into different intervals $[N_{\rm ch}^{\rm min}, N_{\rm ch}^{\rm max}]$ in the actual multiplicity.

The $p_{\rm T}$ spectra are obtained by integrating the $N_{\rm ch}$ and $p_{\rm T}$ dependent charged-particle production rate $\frac{1}{N_{\rm evt,N_{\rm ch}>0}}\frac{{\rm d}^3N}{{\rm d}p_{\rm T}\,{\rm d}\eta\,{\rm d}N_{\rm ch}}$ over the $[N_{\rm ch}^{\rm min},N_{\rm ch}^{\rm max}]$ multiplicity interval. In order to normalize these $p_{\rm T}$ spectra to the number of collisions within the given multiplicity interval, the total number of events $N_{\rm evt,N_{\rm ch}>0}$ is scaled by the corresponding fraction of all collisions, which is derived from the probability density $P(N_{\rm ch})$ as follows:

$$N_{\text{evt},[N_{\text{ch}}^{\text{min}},N_{\text{ch}}^{\text{max}}]} = N_{\text{evt},N_{\text{ch}}>0} \int_{N_{\text{ch}}^{\text{min}}}^{N_{\text{ch}}^{\text{max}}} P(N_{\text{ch}}) dN_{\text{ch}} \quad . \tag{4.3}$$

The $p_{\rm T}$ spectra per collision of the given multiplicity interval are thus defined as:

$$\frac{1}{N_{\text{evt},[N_{\text{ch}}^{\text{min}},N_{\text{ch}}^{\text{max}}]}} \frac{\mathrm{d}^{2}N_{[N_{\text{ch}}^{\text{min}},N_{\text{ch}}^{\text{max}}]}}{\mathrm{d}p_{\text{T}}\,\mathrm{d}\eta} = \frac{1}{N_{\text{evt},N_{\text{ch}}>0}} \frac{\int_{N_{\text{ch}}^{\text{min}}}^{N_{\text{ch}}^{\text{max}}} \frac{\mathrm{d}^{3}N}{\mathrm{d}p_{\text{T}}\,\mathrm{d}\eta\,\mathrm{d}N_{\text{ch}}} \mathrm{d}N_{\text{ch}}}{\int_{N_{\text{ch}}^{\text{min}}}}^{N_{\text{ch}}^{\text{max}}} P(N_{\text{ch}}) \mathrm{d}N_{\text{ch}}}$$
(4.4)

For the interval $[1, \infty)$ this is equivalent to the multiplicity-integrated $p_{\rm T}$ spectrum shown in right panel of Figure 4.1. This multiplicity-integrated $p_{\rm T}$ spectrum is used as a reference to quantify the relative change of the $p_{\rm T}$ spectra with $N_{\rm ch}/\langle N_{\rm ch} \rangle$. Thus, the ratio of a $p_{\rm T}$ spectrum representing collisions within a given $N_{\rm ch}$ range to this reference is defined as:

$$R(p_{\mathrm{T}}) = \left(\frac{1}{N_{\mathrm{evt},[N_{\mathrm{ch}}^{\mathrm{min}},N_{\mathrm{ch}}^{\mathrm{max}}]}} \frac{\mathrm{d}^{2}N_{[N_{\mathrm{ch}}^{\mathrm{min}},N_{\mathrm{ch}}^{\mathrm{max}}]}}{\mathrm{d}p_{\mathrm{T}}\,\mathrm{d}\eta}\right) / \left(\frac{1}{N_{\mathrm{evt},N_{\mathrm{ch}}>0}} \frac{\mathrm{d}^{2}N}{\mathrm{d}p_{\mathrm{T}}\,\mathrm{d}\eta}\right) \quad . \tag{4.5}$$

Figure 4.6 shows $R(p_{\rm T})$ for pp (top left), p–Pb (top right) and AA collisions (bottom) in five different $N_{\rm ch}/\langle N_{\rm ch}\rangle$ intervals. Within each collision system, the results for different center-of-mass energies are in almost perfect agreement. This indicates that the relative change of the $p_{\rm T}$ spectra with multiplicity is independent of the center-of-mass energy and can be characterized solely by $N_{\rm ch}/\langle N_{\rm ch}\rangle$. Thus, $R(p_{\rm T})$ could in

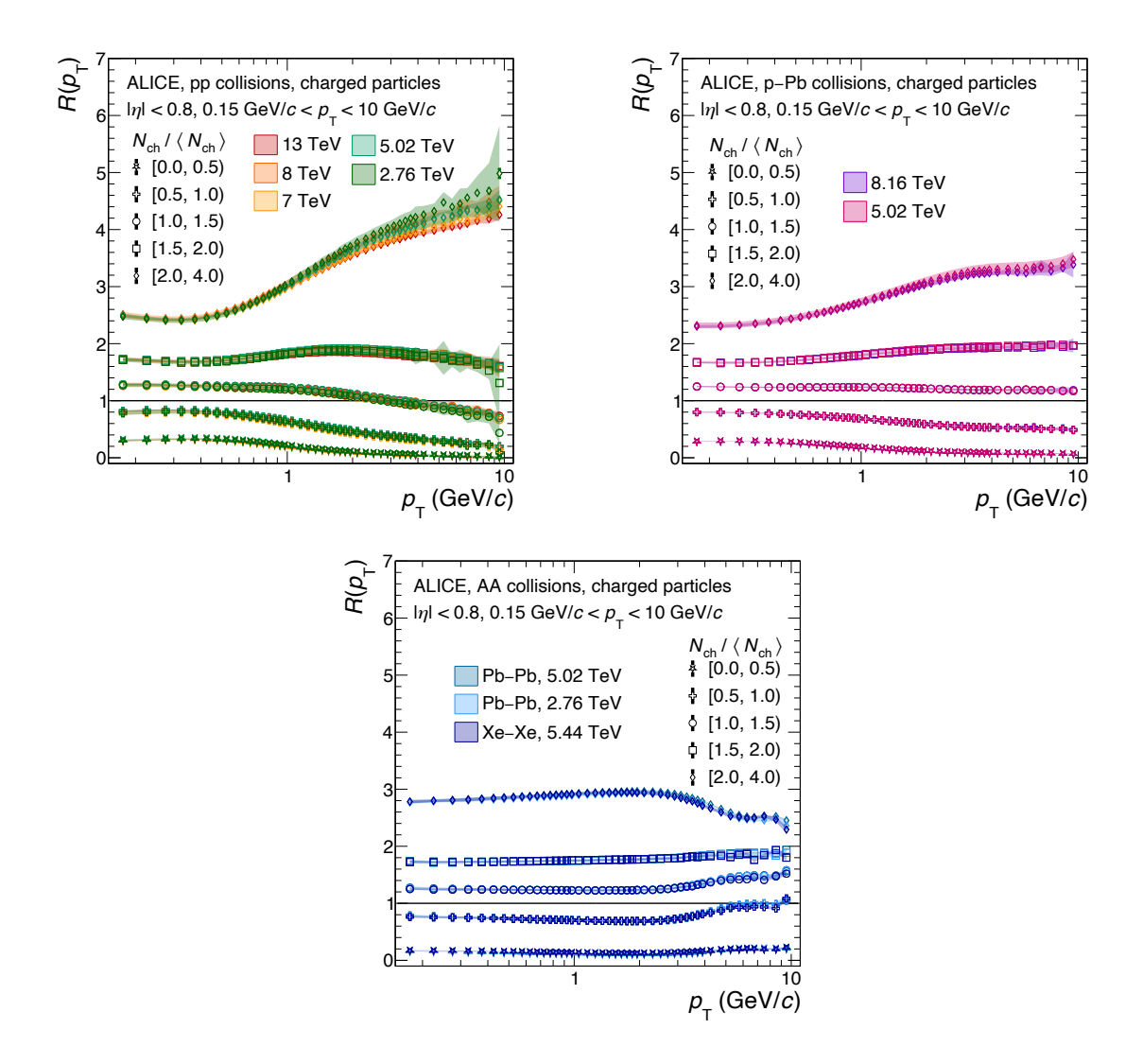


Figure 4.6: Ratio $R(p_{\rm T})$ of the $p_{\rm T}$ spectra of collisions in five different $N_{\rm ch}/\langle N_{\rm ch}\rangle$ intervals to the multiplicity-integrated $p_{\rm T}$ spectrum for pp (top left), p-Pb (top right) and AA collisions (bottom).

principle be used to predict the multiplicity-dependent $p_{\rm T}$ spectra at a given $\sqrt{s_{\rm NN}}$ purely based on the corresponding multiplicity-integrated $p_{\rm T}$ spectrum.

Since the spectra themselves are in fact $\sqrt{s_{\rm NN}}$ dependent and change significantly over the range of considered energies, the perfect alignment of the ratios also implies that the modification of the spectra related to the center-of-mass energy can be separated from the changes correlated with the total number of produced particles.

For each of the three collision systems shown in Figure 4.6, an increase of relative multiplicity has qualitatively different effects on the $p_{\rm T}$ spectra. In pp collisions, a significant enhancement of high- $p_{\rm T}$ particle production with increasing $N_{\rm ch}/\langle N_{\rm ch} \rangle$ is

observed. A similar, but less pronounced, increase is also present in p-Pb collisions. Contrarily, in central AA collisions the contribution of high- $p_{\rm T}$ particles decreases, which might be a result of parton energy loss in the medium.

The offset between the different ratios $R(p_T)$ in Figure 4.6 results from the varying number of particles per collision represented by the compared p_T spectra. In order to study only the spectral shapes regardless of this difference in normalization, the p_T spectra defined in Equation (4.4) are normalized to unity (the number of events cancels in the ratio):

$$P(p_{\rm T}) = \frac{1}{\int \frac{\mathrm{d}^2 N_{[N_{\rm ch}^{\rm min}, N_{\rm ch}^{\rm max}]}}{\mathrm{d}p_{\rm T} \,\mathrm{d}\eta} \mathrm{d}p_{\rm T}} \frac{\mathrm{d}^2 N_{[N_{\rm ch}^{\rm min}, N_{\rm ch}^{\rm max}]}}{\mathrm{d}p_{\rm T} \,\mathrm{d}\eta} \quad . \tag{4.6}$$

This corresponds to the probability density for particle production as a function of $p_{\rm T}$. The relative change in the shape of the $p_{\rm T}$ spectra is then quantified by dividing $P(p_{\rm T})$ for a given multiplicity interval to the corresponding probability density $P(p_{\rm T})_{\rm incl}$ of the multiplicity-integrated $p_{\rm T}$ spectrum. This ratio $P(p_{\rm T})/P(p_{\rm T})_{\rm incl}$ corresponds to $R(p_{\rm T})$ defined in Equation (4.5), but with the $p_{\rm T}$ spectra in both the numerator and denominator separately normalized to unity.

The top panel of Figure 4.7 displays $P(p_{\rm T})/P(p_{\rm T})_{\rm incl}$ of collisions with multiplicities above and below $\langle N_{\rm ch} \rangle$. As previously observed in Figure 4.6, the measurements of the different collision systems follow distinct energy-independent trends. Both for $N_{\rm ch}/\langle N_{\rm ch} \rangle < 1$ and $N_{\rm ch}/\langle N_{\rm ch} \rangle > 1$ the ratio $P(p_{\rm T})/P(p_{\rm T})_{\rm incl}$ crosses unity at $p_{\rm T} \approx 650\,{\rm MeV}/c$. The probability for producing charged particles with transverse momenta below this crossing point is enhanced for $N_{\rm ch}/\langle N_{\rm ch} \rangle < 1$ collisions, while the probability for higher transverse momenta increases in events with $N_{\rm ch}/\langle N_{\rm ch} \rangle > 1$. For AA collisions this trend changes for the particles with transverse momenta above $p_{\rm T} \approx 3.2\,{\rm GeV}/c$ as the higher transverse momenta are suppressed in the more central collisions, probably as a consequence of parton energy loss in the hot and dense medium.

To further characterize the evolution of the relative change of the spectral shapes as a function of $N_{\rm ch}/\langle N_{\rm ch} \rangle$, their moments are compared to the corresponding moments of the multiplicity-integrated $p_{\rm T}$ spectrum. The bottom panels of Figure 4.7 show the mean $\langle p_{\rm T} \rangle$ (left) and standard deviation $\sigma(p_{\rm T})$ (right) of the $p_{\rm T}$ spectra as a function

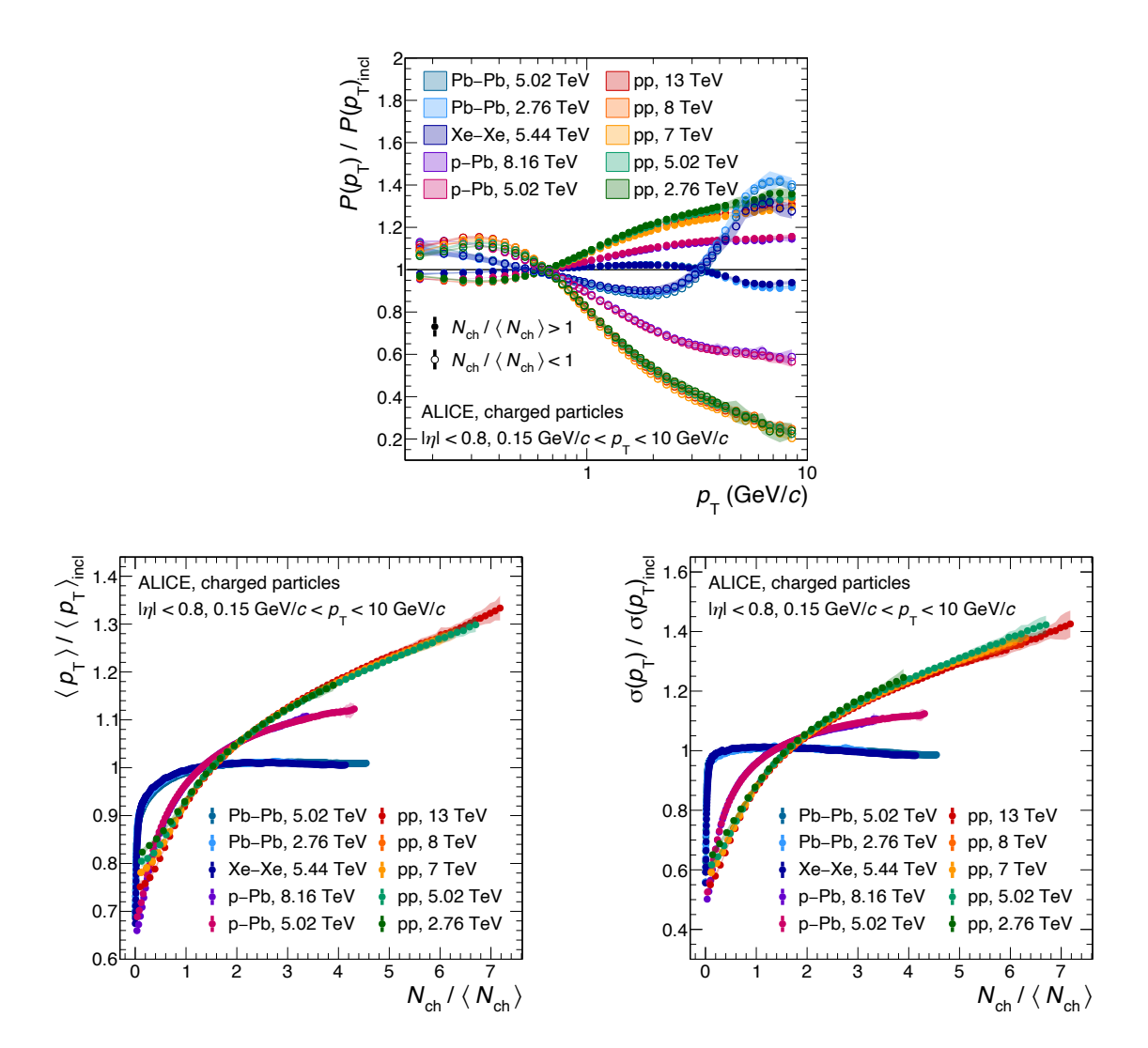


Figure 4.7: $P(p_{\rm T})/P(p_{\rm T})_{\rm incl}$ in two $N_{\rm ch}/\langle N_{\rm ch}\rangle$ intervals (top) as well as $\langle p_{\rm T}\rangle/\langle p_{\rm T}\rangle_{\rm incl}$ (bottom left) and $\sigma(p_{\rm T})/\sigma(p_{\rm T})_{\rm incl}$ (bottom right) as a function of $N_{\rm ch}/\langle N_{\rm ch}\rangle$.

of $N_{\rm ch}/\langle N_{\rm ch}\rangle$ normalized to their equivalent of the multiplicity-integrated $p_{\rm T}$ spectrum $\langle p_{\rm T}\rangle_{\rm incl}$ and $\sigma(p_{\rm T})_{\rm incl}$, respectively. Apart from the lowest relative multiplicities, where the $\langle p_{\rm T}\rangle$ and $\sigma(p_{\rm T})$ are independent of the center-of-mass energy of the collision (see Figure 4.2), $\langle p_{\rm T}\rangle/\langle p_{\rm T}\rangle_{\rm incl}$ and $\sigma(p_{\rm T})/\sigma(p_{\rm T})_{\rm incl}$ coincide for different $\sqrt{s_{\rm NN}}$ of a given collision system. This underlines the previously observed universal dependence of the $p_{\rm T}$ spectra on the relative multiplicity.

Quantifying medium effects in heavy-ion collisions The previous comparisons revealed significant suppression of the particle production at high p_T in AA collisions.

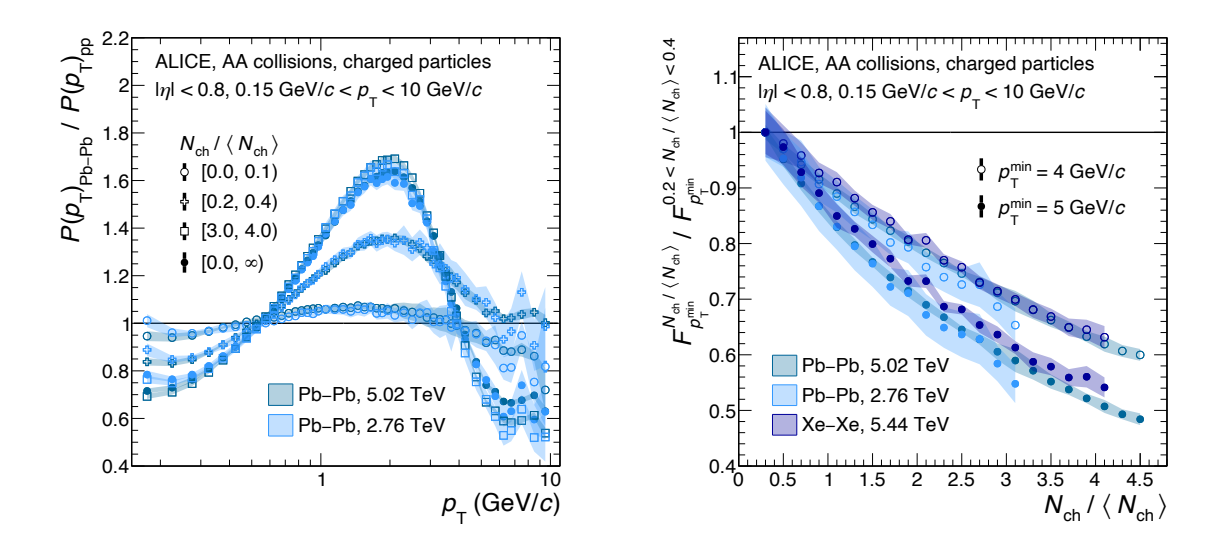


Figure 4.8: Ratio of $P(p_T)_{Pb-Pb}$ for different relative multiplicity intervals in Pb-Pb collisions to $P(p_T)_{pp}$ in pp collisions (left) and ratio of the high- p_T fraction of particles to peripheral AA collisions (right).

To study the modification of the heavy-ion spectra, the probability density $P(p_T)_{Pb-Pb}$ of different $N_{ch}/\langle N_{ch}\rangle$ intervals is divided by the probability density $P(p_T)_{pp}$ for pp collisions at the same center-of-mass energy. This is shown in the left panel of Figure 4.8 for Pb-Pb and pp collisions at $\sqrt{s_{NN}}=2.76\,\text{TeV}$ and 5.02 TeV. While in peripheral Pb-Pb collisions $P(p_T)_{Pb-Pb}$ is similar to $P(p_T)_{pp}$, with increasing relative multiplicity, low- p_T particles are pushed to higher transverse momenta, potentially by radial flow, resulting in an enhancement of the spectrum around $p_T\approx 2\,\text{GeV}/c$. Contrarily, the probability of producing particles at higher transverse momenta depletes with increasing centrality.

This suppression of high- $p_{\rm T}$ particle production is further illustrated in the right panel of Figure 4.8. It shows the fraction $F_{p_{\rm T}^{\rm min}}^{N_{\rm ch}/\langle N_{\rm ch}\rangle}$ of particles above a given transverse momentum threshold $p_{\rm T}^{\rm min}$ at a relative multiplicity $N_{\rm ch}/\langle N_{\rm ch}\rangle$ normalized to the corresponding fraction in peripheral collisions $(0.2 < N_{\rm ch}/\langle N_{\rm ch}\rangle < 0.4)$. This quantity is shown for all three AA datasets employing two different momentum thresholds $p_{\rm T}^{\rm min} = 4\,{\rm GeV}/c$ and $p_{\rm T}^{\rm min} = 5\,{\rm GeV}/c$. With increasing relative multiplicity, i.e. collision centrality, a decreasing fraction of the particles are produced at high transverse momenta. This suppression of high- $p_{\rm T}$ particle production as a function of relative multiplicity follows the same trend for Pb–Pb and Xe–Xe collisions and is more pronounced for the higher transverse momenta. It is a unique feature of AA collisions

and could be related to the energy loss of partons in the hot and dense QCD medium created in these interactions.

In conclusion, the similarities and differences of the charged-particle final state in pp, p-Pb and AA collisions at different center-of-mass energies provided in this subsection concisely characterize particle production at LHC energies. Complemented by theoretical models, the extensive measurements will help to better understand the underlying particle production mechanisms. The results of this work significantly extend the previous measurements, as will be discussed in the next subsection.

4.2 Comparison to published experimental results

To highlight how the present work complements and extends existing measurements of the charged-particle final state at LHC collision energies, selected results are compared to five ALICE publications. The kinematic range chosen for the observables presented in this thesis limits the number of compatible results from previous analyses and often requires an additional transformation of the data to obtain approximately similar observables, thus allowing only for qualitative comparisons.

The top left panel of Figure 4.9 shows a comparison of the charged-particle multiplicity distribution of pp collisions at $\sqrt{s}=7\,\mathrm{TeV}$ with a similar measurement from 2013 published in Ref. [93]. In the latter analysis, the unfolded distribution is obtained using a regularized χ^2 -minimization procedure with a parametrized detector response matrix and without applying a particle-composition correction. The results of both analyses agree within deviations of less than 10 % that are mostly covered by the combined systematic uncertainties.

The top right panel of Figure 4.9 compares $\langle p_{\rm T} \rangle$ as a function of $N_{\rm ch}$ for AA collisions with $\langle p_{\rm T} \rangle$ values derived from the centrality-dependent $p_{\rm T}$ spectra published in Refs. [34, 48]. Each centrality class used in the two publications is related to an average charged-particle density at mid-rapidity as presented in Refs. [95, 96, 97]. To obtain multiplicities within the pseudorapidity range $|\eta| < 0.8$, these $\langle {\rm d}N_{\rm ch}/{\rm d}\eta \rangle$ values are scaled by a factor of 1.6. The results presented in this thesis agree well with the published measurements, though the constructed multiplicities would actually be 7-10% smaller considering that the $N_{\rm ch}$ definition used in this work does not include

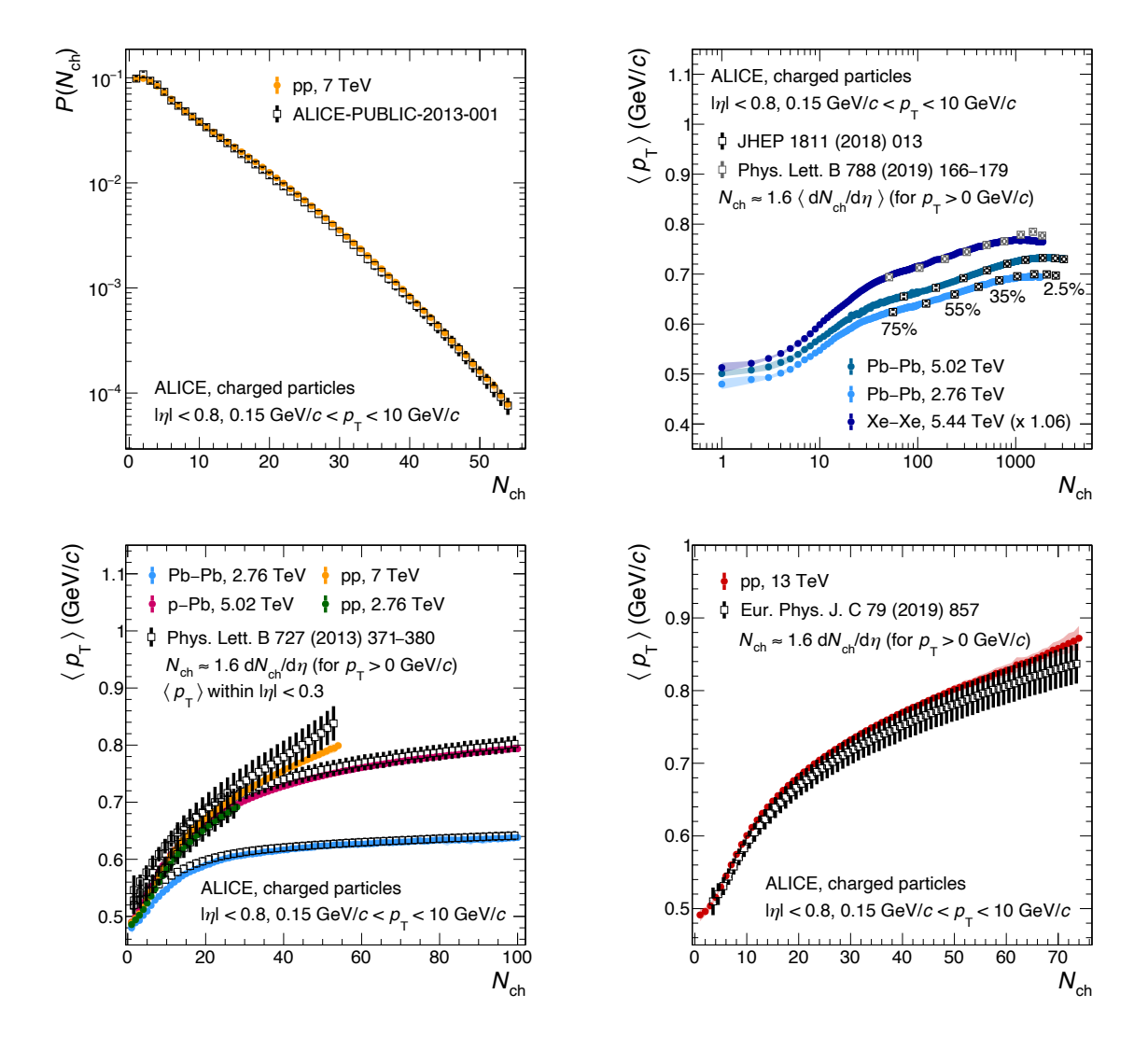


Figure 4.9: Comparison of selected results of this work to five previous ALICE measurements published in Refs. [93, 34, 48, 38, 94].

particles with transverse momenta below $p_{\rm T}=0.15\,{\rm GeV}/c$. The figure illustrates that the results of the present work exhibit a finer granularity compared to the previous measurements of $\langle p_{\rm T} \rangle$ as a function of $N_{\rm ch}$ in AA collisions and extend it to the most peripheral collisions.

The bottom left panel of Figure 4.9 shows a comparison of $\langle p_{\rm T} \rangle$ as a function of $N_{\rm ch}$ to a similar measurement from 2013 reported in Ref. [38] for pp collisions at $\sqrt{s} = 2.76\,\text{TeV}$ and 7 TeV, p-Pb collisions at $\sqrt{s_{\rm NN}} = 5.02\,\text{TeV}$ and Pb-Pb collisions at $\sqrt{s_{\rm NN}} = 2.76\,\text{TeV}$. In the latter publication, the $\langle p_{\rm T} \rangle - N_{\rm ch}$ correlation is obtained by re-weighting the average transverse momenta measured as a function of the number of charged-particle tracks with the detector response matrix. No correction for the MC

particle composition is applied. The $\langle p_{\rm T} \rangle$ is calculated within a narrow pseudorapidity window of $|\eta| < 0.3$ and is reported as a function of the charged-particle density at mid-rapidity including particles with transverse momenta down to $p_{\rm T} \approx 0$. For compatibility with the present work, the multiplicity values of the publication are again scaled by a factor of 1.6. The comparison of the results illustrates that the analysis method employed in this thesis achieves smaller systematic uncertainties and hence an increased precision of the measured $\langle p_{\rm T} \rangle - N_{\rm ch}$ correlation.

The bottom right panel of Figure 4.9 shows a comparison of $\langle p_{\rm T} \rangle$ as a function of $N_{\rm ch}$ for pp collisions at $\sqrt{s}=13\,{\rm TeV}$ to a measurement from 2019 published in Ref. [94]. The latter analysis employs the same re-weighting procedure as used in Ref. [38] and the results are also reported as a function of the charged-particle density at midrapidity without a lower $p_{\rm T}$ threshold. After scaling the multiplicity density with a factor of 1.6, the measurements agree within their uncertainties. The systematic shift of the published $\langle p_{\rm T} \rangle$ towards lower values at high $N_{\rm ch}$ with respect to the results of the present work is consistent with the expected bias originating from the re-weighting procedure as presented in Ref. [98].

In conclusion, these comparisons illustrate that the present work is consistent with previous measurements while providing a higher precision due to the newly developed analysis technique. The novel analysis method additionally allows for a finer granularity in $N_{\rm ch}$, while at the same time giving access to additional observables of the charged-particle final state that are discussed in the previous subsection. By including all LHC Run 1 and Run 2 datasets this analysis also extends the previously available measurements by more collision systems and center-of-mass energies.

4.3 Comparison to theoretical models

Another goal of this work is to compare the presented experimental measurements to different MC event generators in order to test their accuracy of modeling charged-particle production at LHC energies. Figure 4.10, Figure 4.11 and Figure 4.12 show the ratios of generator predictions to the pp, p–Pb and AA measurements, respectively. All three figures display these ratios for four different observables: the multiplicity distribution (top left), the multiplicity-integrated $p_{\rm T}$ spectrum (top right), and the $\langle p_{\rm T} \rangle$

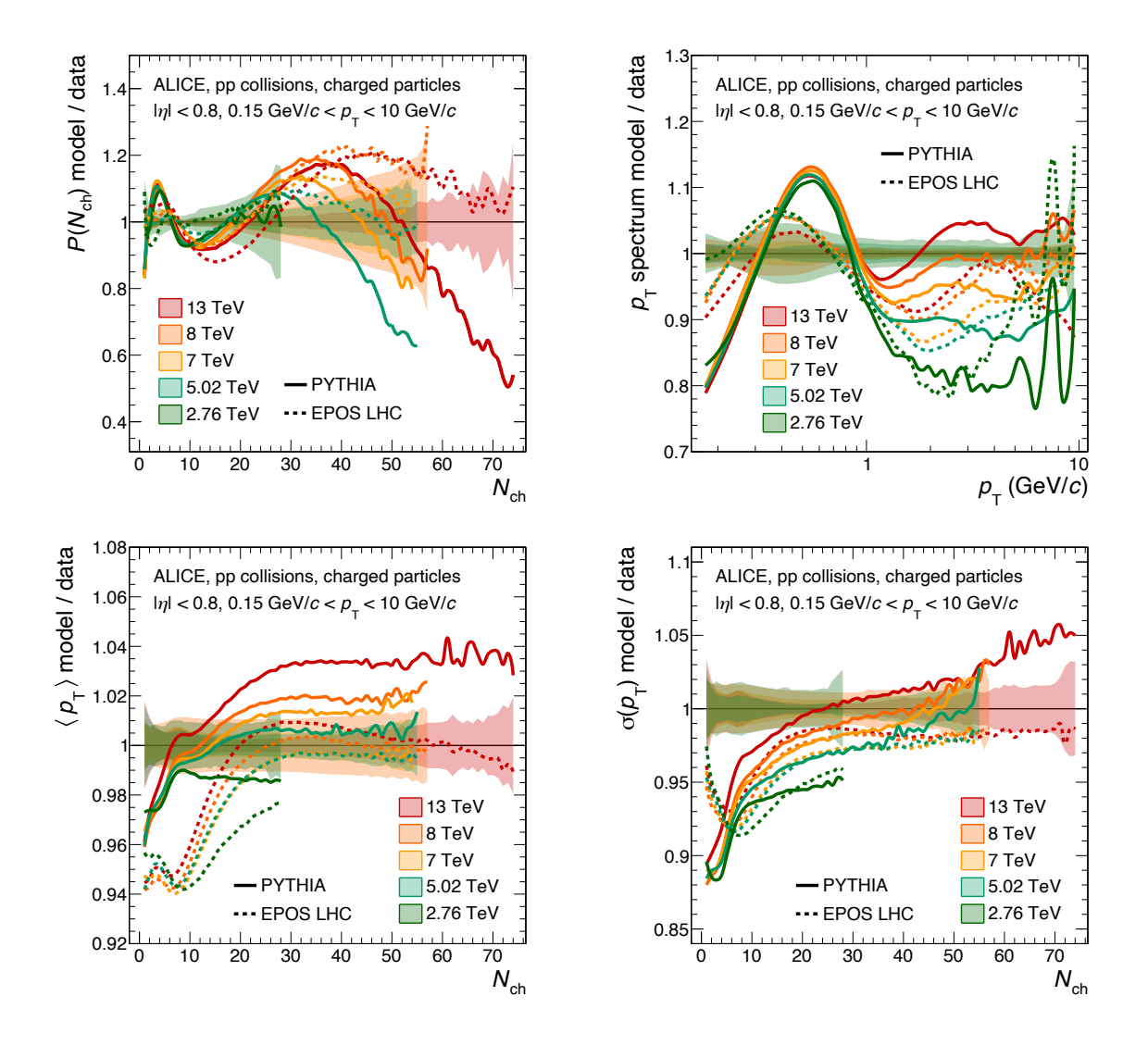


Figure 4.10: PYTHIA and EPOS LHC predictions for the pp multiplicity distributions (top left), $p_{\rm T}$ spectra (top right), $\langle p_{\rm T} \rangle$ (bottom left), and $\sigma(p_{\rm T})$ (bottom right) compared to the measurements.

and $\sigma(p_{\rm T})$ as a function of $N_{\rm ch}$ (bottom left and right, respectively). The measurements in pp and p–Pb collisions are compared to predictions from both PYTHIA (solid lines) and EPOS LHC (dashed lines), while AA collisions are only compared to the HIJING event generator. PYTHIA is used in version 8.306 with the Monash-2013 tune [13] and with the Angantyr model [99] for collisions involving heavy nuclei.

pp collisions For pp collisions, the multiplicity distributions and $p_{\rm T}$ spectra shown in the upper panels of Figure 4.10 are described by both PYTHIA and EPOS LHC within 20%, except at high multiplicities where PYTHIA increasingly deviates from

the data. For low multiplicities $N_{\rm ch} < 10$ and transverse momenta $p_{\rm T} < 1\,{\rm GeV}/c$, the PYTHIA predictions differ equally from the measurements for all five datasets, implying that the overall energy dependence of charged-particle production is modeled realistically in this soft regime. For EPOS LHC this correct modeling of the energy dependence is not observed. However, below $p_{\rm T} \approx 1\,{\rm GeV}/c$ EPOS LHC generally describes the measured $p_{\rm T}$ spectra better than PYTHIA.

For $\langle p_{\rm T} \rangle$ and $\sigma(p_{\rm T})$ as a function of $N_{\rm ch}$ shown in the bottom panels of Figure 4.10, the model predictions are more accurate than for the multiplicity distributions and $p_{\rm T}$ spectra. PYTHIA underpredicts the experimental data on $\langle p_{\rm T} \rangle$ at the lowest values of $N_{\rm ch}$ only by up to 4%, while EPOS LHC deviates by up to 6%. Above $N_{\rm ch} \approx 30$, EPOS LHC describes the measurements within its systematic uncertainties, while PYTHIA deviates more with increasing collision energy. The $N_{\rm ch}$ -dependent $p_{\rm T}$ spectra are generally predicted too narrow by both models, most pronounced for PYTHIA which underpredicts $\sigma(p_{\rm T})$ by more than 10% at the lowest multiplicities. An exception is the PYTHIA prediction for high-multiplicity collisions at $\sqrt{s}=13\,{\rm TeV}$, where the spectra are up to 5% broader than observed in the experiment.

p-Pb collisions For p-Pb collisions, the differences between the two MC event generators are more pronounced than for pp collisions. Overall, both models provide significantly worse descriptions of the data than for pp collisions, in particular of the multiplicity distributions and $p_{\rm T}$ spectra shown in the top panels of Figure 4.11. PYTHIA deviates from the measured multiplicity distribution by up to 30%. EPOS LHC provides a slightly better description for $N_{\rm ch} < 70$ where it agrees with the data within 20%, but underestimates the occurrence probability of high-multiplicity collisions by up to 80%. However, EPOS LHC describes the $p_{\rm T}$ spectrum at $p_{\rm T} < 5\,{\rm GeV}/c$ significantly better than PYTHIA, which deviates from the measurement by up to 40%. Both models severely underestimate the charged-particle production at high transverse momenta.

PYTHIA models the multiplicity dependence of the $p_{\rm T}$ spectra significantly worse than EPOS LHC as apparent in the bottom panels of Figure 4.11. While EPOS LHC reproduces the measured $\langle p_{\rm T} \rangle$ as well as $\sigma(p_{\rm T})$ within less than 10%, the PYTHIA prediction deviates increasingly with $N_{\rm ch}$ by up to 25%. These large deviations are potentially a result of the missing color reconnection between partons from different

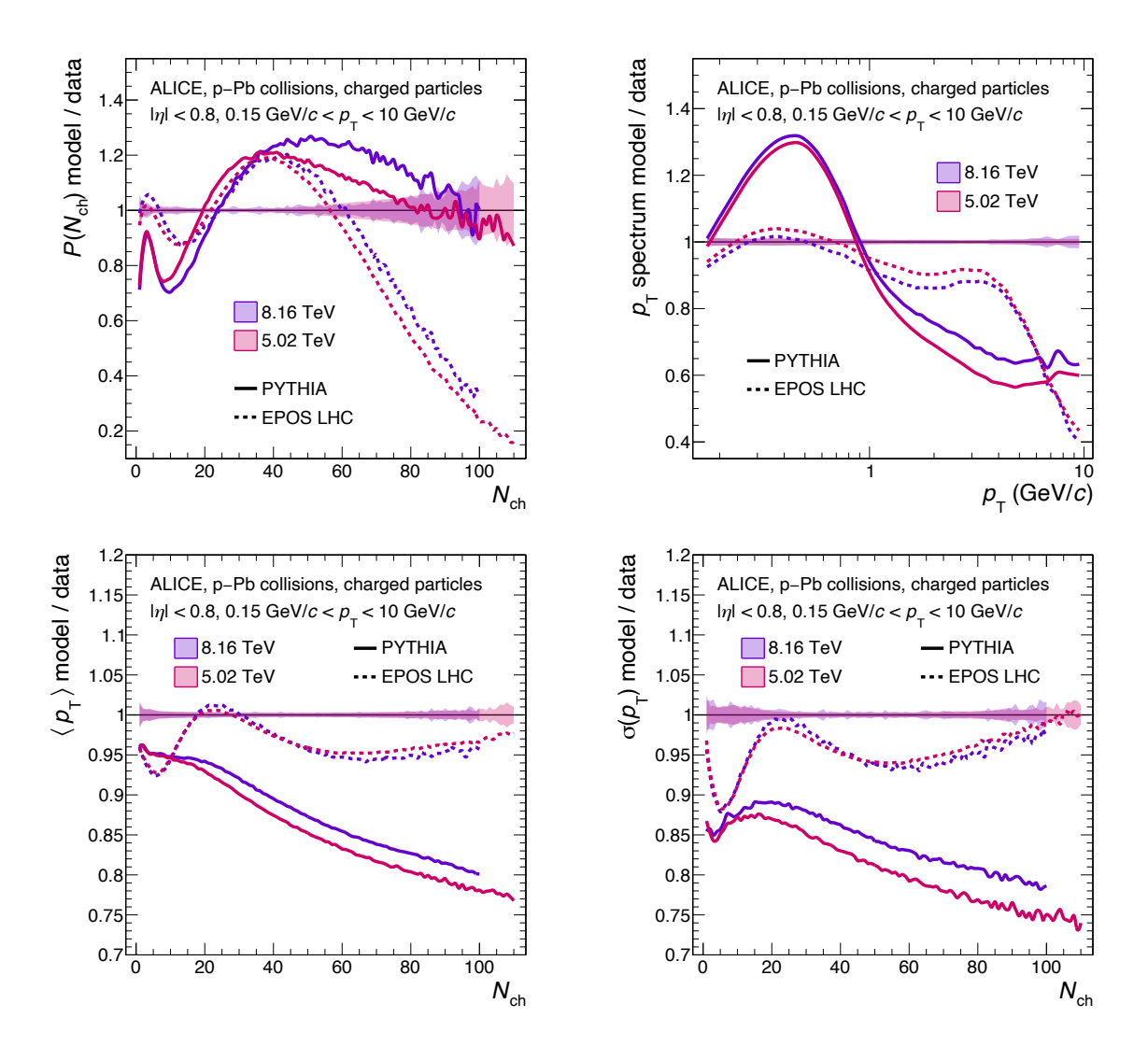


Figure 4.11: PYTHIA and EPOS LHC predictions for the p-Pb multiplicity distributions (top left), $p_{\rm T}$ spectra (top right), $\langle p_{\rm T} \rangle$ (bottom left), and $\sigma(p_{\rm T})$ (bottom right) compared to the measurements.

nucleons and might improve in newer PYTHIA versions [100, 101]. Both models systematically underpredict the average transverse momentum and the width of the spectra as a function of multiplicity. Considering only the observables presented here, EPOS LHC generally seems better suited than PYTHIA to describe p–Pb collisions. Apparently EPOS LHC also better reproduces the overall energy dependence of all four observables as the ratios of the model predictions to the experimental data are almost the same for $\sqrt{s_{\rm NN}} = 5.02\,{\rm TeV}$ and $8.16\,{\rm TeV}$.

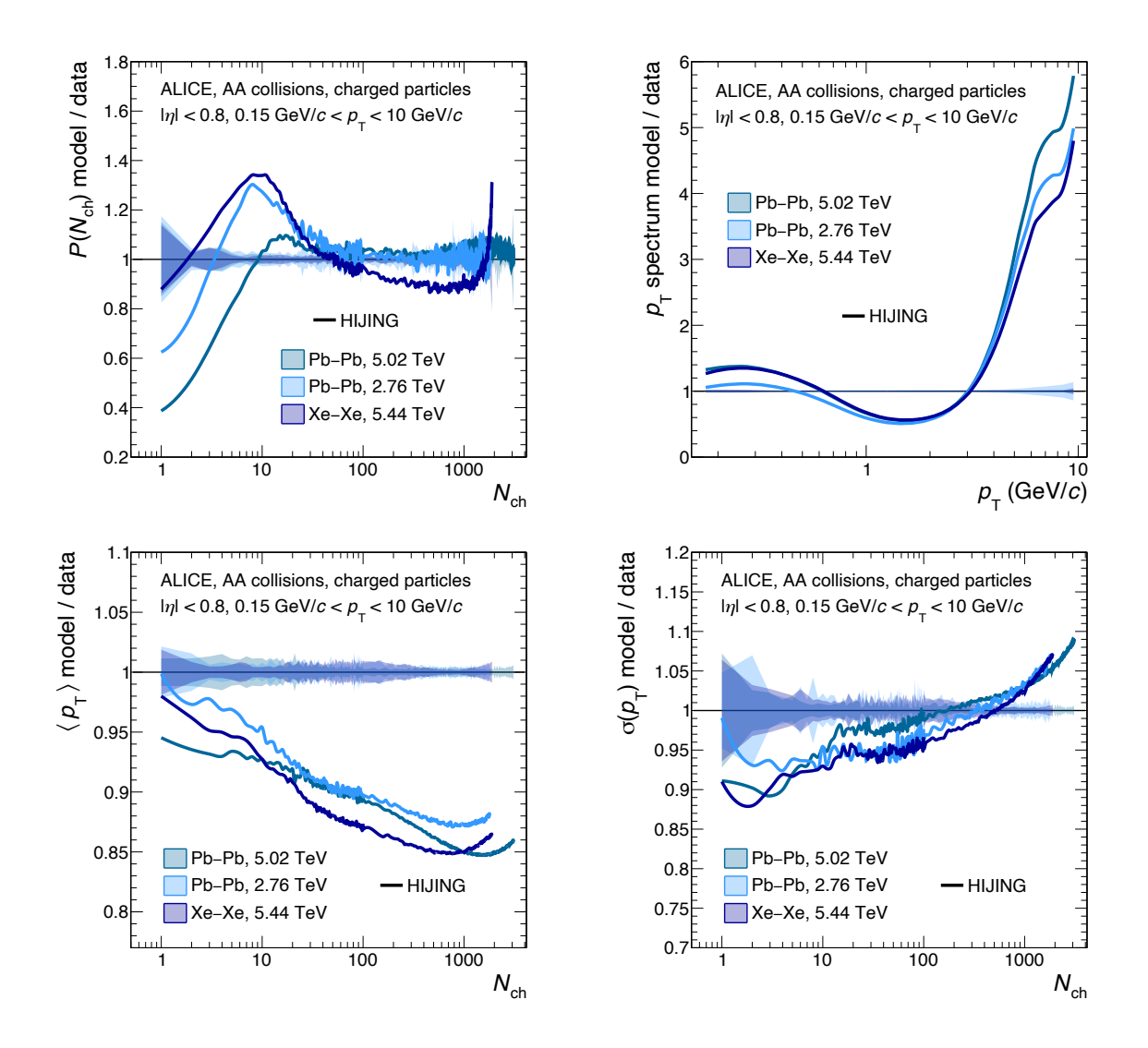


Figure 4.12: HIJING predictions for the AA multiplicity distributions (top left), $p_{\rm T}$ spectra (top right), $\langle p_{\rm T} \rangle$ (bottom left), and $\sigma(p_{\rm T})$ (bottom right) compared to the measurements.

AA collisions Figure 4.12 shows a comparison of the measurements in Pb–Pb and Xe–Xe collisions to the HIJING event generator. The multiplicity distributions are well described over most of the $N_{\rm ch}$ range, with the largest deviations of 10% for Xe–Xe collisions. However, for very peripheral collisions ($N_{\rm ch} < 30$) the discrepancies reach up to 60%. The $p_{\rm T}$ spectra predicted by HIJING differ by up to 40% below $p_{\rm T} \approx 3\,{\rm GeV}/c$ and overestimate the charged-particle production at high $p_{\rm T}$ by a factor five. HIJING underestimates the mean transverse momentum of the spectra with an increasing deviation towards the more central collisions, where it reaches up to 25%. The width of the simulated spectra deviates from the measurement by around 10%.

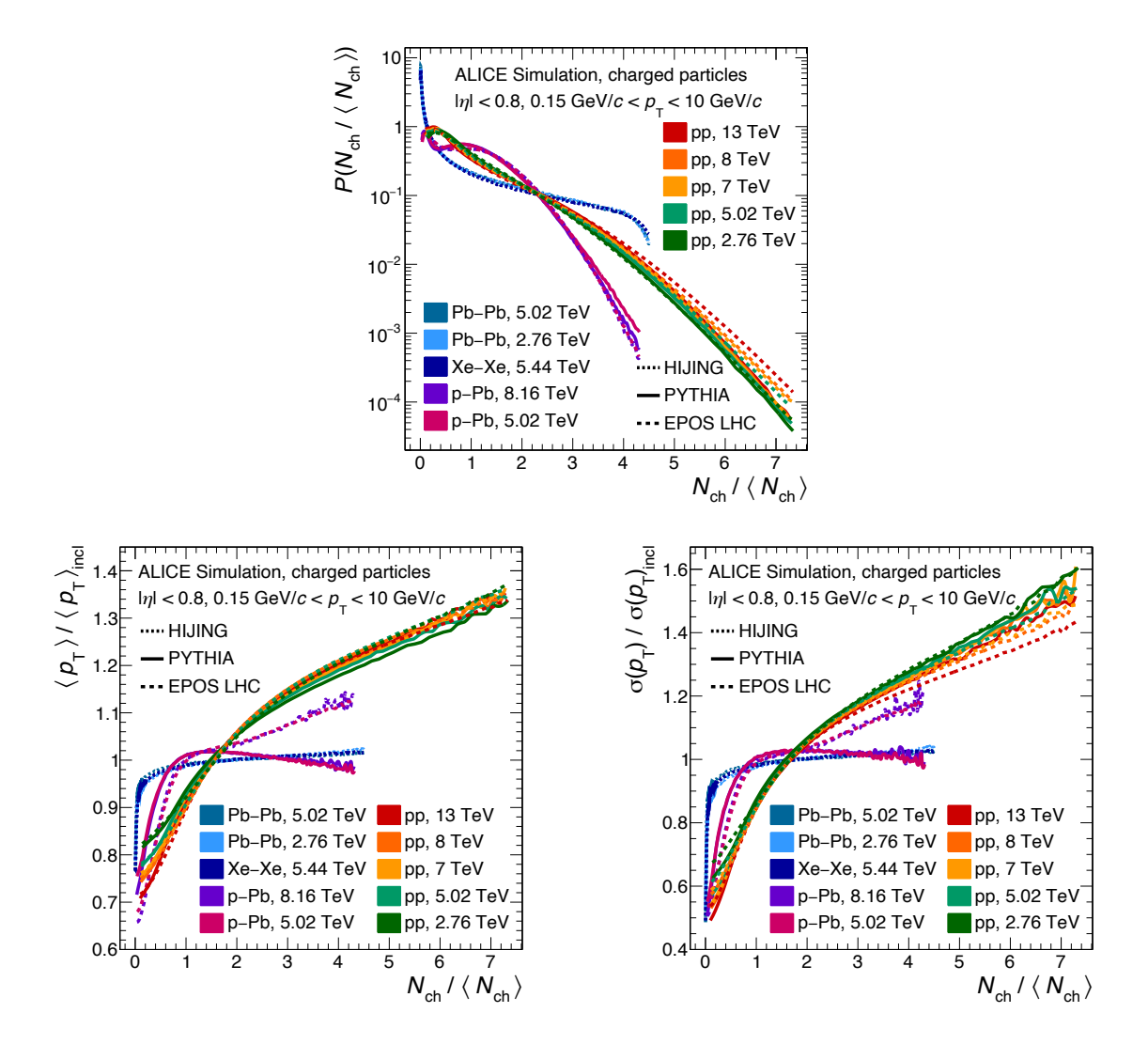


Figure 4.13: PYTHIA, EPOS LHC and HIJING predictions for $P(N_{\rm ch}/\langle N_{\rm ch}\rangle)$ (top), $\langle p_{\rm T}\rangle/\langle p_{\rm T}\rangle_{\rm incl}$ (bottom left) and $\sigma(p_{\rm T})/\sigma(p_{\rm T})_{\rm incl}$ (bottom right) as a function of $N_{\rm ch}/\langle N_{\rm ch}\rangle$.

Relative-multiplicity dependence in the models The study of experimental observables as a function of relative multiplicity revealed similarities among the different center-of-mass energies within each collision system. To test if the models also exhibit these characteristics, the experimental observables shown in Figure 4.5 and Figure 4.7 are presented for the four available MC event generators.

Figure 4.13 shows $P(N_{\rm ch}/\langle N_{\rm ch}\rangle)$, as well as the $\langle p_{\rm T}\rangle/\langle p_{\rm T}\rangle_{\rm incl}$ and $\sigma(p_{\rm T})/\sigma(p_{\rm T})_{\rm incl}$ of the $p_{\rm T}$ spectra as a function of the relative multiplicity $N_{\rm ch}/\langle N_{\rm ch}\rangle$ for PYTHIA, EPOS LHC and HIJING. For pp collisions, the KNO-scaled multiplicity distributions at different center-of-mass energies better coincide for PYTHIA than for EPOS LHC.

This is also the case for $\sigma(p_{\rm T})/\sigma(p_{\rm T})_{\rm incl}$, while for $\langle p_{\rm T} \rangle/\langle p_{\rm T} \rangle_{\rm incl}$ the EPOS LHC predictions at different energies better align on a common curve than the PYTHIA simulations. For p–Pb collisions, the KNO-scaled multiplicity distributions follow similar trends in EPOS LHC and PYTHIA, with a pronounced double peak structure that is not observed in the measurement. In EPOS LHC, the KNO-scaled distributions of the two different center-of-mass energies are in better agreement than in PYTHIA. Both $\langle p_{\rm T} \rangle/\langle p_{\rm T} \rangle_{\rm incl}$ and $\sigma(p_{\rm T})/\sigma(p_{\rm T})_{\rm incl}$ follow distinctly different trends for the two generators, neither resembling the trend observed in the experimental data. All three observables are similar for the AA collisions at different center-of-mass energies simulated with HIJING. In contrast to the previously discussed observation in the experimental data, HIJING predicts no decrease of $\sigma(p_{\rm T})/\sigma(p_{\rm T})_{\rm incl}$ with relative multiplicity and also predicts no comparable suppression of the particles with high transverse momenta (not shown).

Further model comparisons In addition to the predictions from the event generators PYTHIA, EPOS LHC and HIJING, further theoretical calculations are available for the $\langle p_{\rm T} \rangle - N_{\rm ch}$ correlation in different collision systems. Figure 4.14 shows the measured $\langle p_{\rm T} \rangle$ as a function of $N_{\rm ch}$ for pp, p-Pb and Pb-Pb collisions at the same center-of-mass energy per nucleon pair, $\sqrt{s_{\rm NN}} = 5.02 \, {\rm TeV}$, together with three different theoretical calculations. The left panel represents predictions from PYTHIA which, as discussed previously, describes $\langle p_{\rm T} \rangle$ vs. $N_{\rm ch}$ in pp collisions well, while the p-Pb measurements are significantly underpredicted. Also in Pb-Pb collisions, $\langle p_{\rm T} \rangle$ is systematically underestimated by PYTHIA over the whole multiplicity range. The middle panel shows projections of the EPOS3 model, which also cannot reproduce the $\langle p_{\rm T} \rangle$ evolution with $N_{\rm ch}$. EPOS3 overpredicts $\langle p_{\rm T} \rangle$ below $N_{\rm ch} \approx 15$ for all three systems, and underestimates it at higher multiplicities, although less than PYTHIA in case of the p-Pb and Pb-Pb collisions. It is noteworthy that EPOS3 does not describe pp and p-Pb collisions as well as EPOS LHC. The right panel of Figure 4.14 shows hydrodynamic calculations with CGC initial conditions [102], which strongly deviate from the measurements in all three collision systems. In contrast to PYTHIA, EPOS3, and the experimental data, the predictions for pp, p-Pb and Pb-Pb collisions do not converge to similar $\langle p_{\rm T} \rangle$ values at the lowest multiplicities. However, for the more central Pb-Pb collisions, the hydrodynamic calculation yields an average transverse

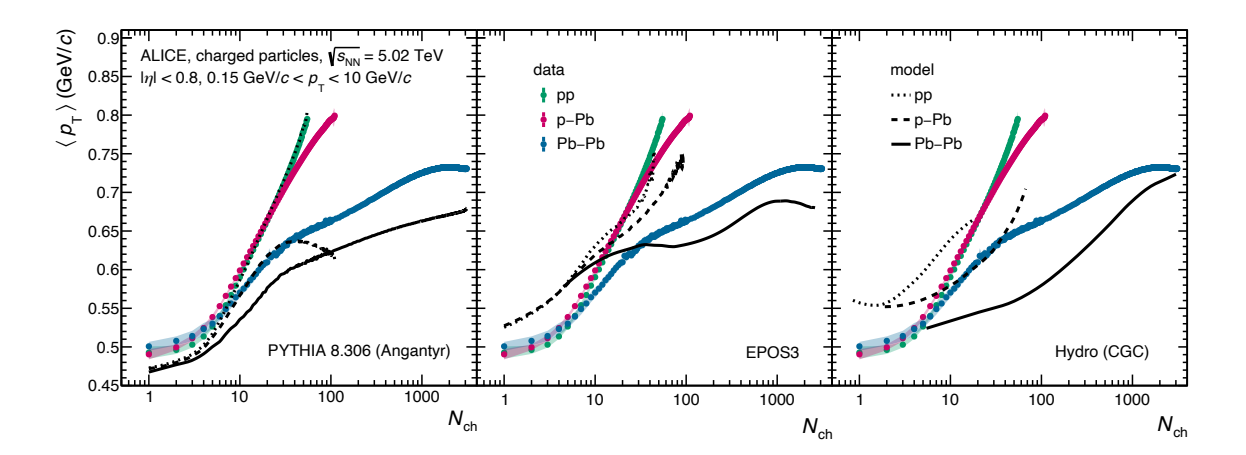


Figure 4.14: Comparisons of the measured $\langle p_{\rm T} \rangle$ as a function of $N_{\rm ch}$ in pp, p–Pb and Pb–Pb collisions at $\sqrt{s_{\rm NN}}=5.02\,{\rm TeV}$ with PYTHIA, EPOS3 and a CGC-based hydrodynamical calculation.

momentum more similar to the experimental results than the other models.

In conclusion, all previously shown comparisons highlight that describing the fundamental observables presented in this thesis poses a serious challenge to the current theoretical modeling of particle production in high-energy collisions. Since the presented measurements precisely characterize the charged-particle final state across various collision scenarios, they provide a crucial reference for future model development and tuning. To facilitate this process, a RIVET [103] analysis was developed in the scope of this work. Through the interface provided by RIVET, simulated collisions from various MC event generators can be processed and the same observables as in the measurement are calculated. This makes the results presented in this work more accessible for future model comparisons.

Additionally, the data are published on the data preservation website HEPData [92] and can therefore be used for further studies like those presented in the next subsection.

4.4 Supplementary studies

The main results of this thesis are complemented by two supplementary studies that are briefly outlined in the following. The first study aims to extrapolate the multiplicity distributions and $p_{\rm T}$ spectra of the five pp datasets to unmeasured center-of-mass energies. The second study demonstrates the potential of LHC Run 3 data to extend the set of collision scenarios analyzed in this work.

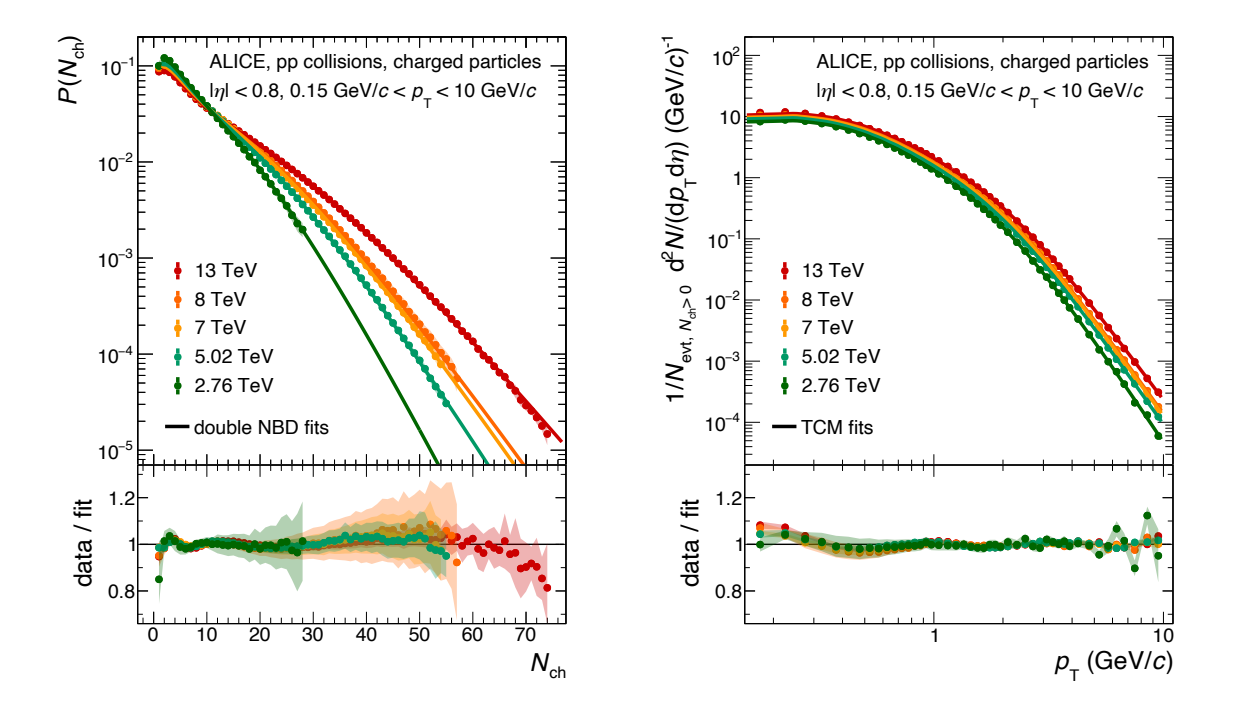


Figure 4.15: Multiplicity distributions (left) and $p_{\rm T}$ spectra (right) of pp collisions parametrized with double NBD and TCM functions, respectively.

4.4.1 Extrapolations to unmeasured pp collision energies

In order to predict charged-particle production in pp collisions beyond the discrete center-of-mass energies available at the LHC, the five measurements presented in this thesis are parametrized. The multiplicity distributions are parametrized by a combination of two negative binomial distributions (NBDs), representing soft and semi-hard sources of particle production, respectively, as discussed in Refs. [109, 24]. The multiplicity-integrated $p_{\rm T}$ spectra are parametrized with a two component model (TCM), consisting of a sum of an exponential and a power law function describing the trends at low and high transverse momenta, respectively, as proposed in Ref. [36]. Further physics-inspired parametrizations of the $p_{\rm T}$ spectra presented in this thesis are discussed in Ref. [110].

Figure 4.15 shows the multiplicity distributions (left) and the multiplicity-integrated $p_{\rm T}$ spectra (right) together with the corresponding functions. The ratios of the parametrization to the data shown in the bottom panels illustrate that both functions provide a good description of the data, allowing to extrapolate the $N_{\rm ch}$ range of the multiplicity distributions and the $p_{\rm T}$ range of the transverse-momentum spectra be-

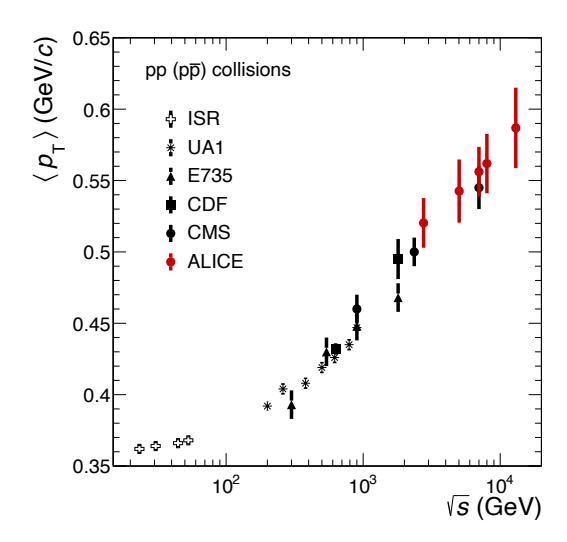


Figure 4.16: World data for the \sqrt{s} dependence of the $\langle p_{\rm T} \rangle$ in pp collisions. The bars represent the systematic uncertainties. The ALICE measurements correspond to the results of this work. The remaining data points are taken from Refs. [104, 41, 105, 106, 107, 35].

yond the reach of the measurement. In particular the extrapolation of the spectra to $p_{\rm T}\approx 0$ permits deriving $\langle p_{\rm T}\rangle$ values that represent the whole transverse momentum range. Their systematic uncertainty is estimated as the difference to corresponding results obtained with a modified Hagedorn parametrization. The $\langle p_{\rm T}\rangle$ as a function of \sqrt{s} for the five LHC energies analyzed in this work are shown in Figure 4.16 together with previous measurements in pp and p \bar{p} collisions.

To predict the multiplicity distributions and $p_{\rm T}$ spectra for an unmeasured center-of-mass energy, the parameters defining the fit functions could be parametrized as a function of \sqrt{s} . An alternative approach to extrapolate the data to unmeasured energies is to use machine-learning techniques. In the extended scope of this work [111, 108], the multiplicity distributions and $p_{\rm T}$ spectra resulting from the present analysis are parametrized using deep neural networks (DNNs). These neural networks parametrize the \sqrt{s} and $N_{\rm ch}$ or $p_{\rm T}$ dependent trends inherent in the data and thereby allow for predicting the two observables at unmeasured energies. A DNN consists of multiple consecutive layers of interconnected nodes that combine incoming signals and transform them utilizing non-linear activation functions. According to the universal approximation theorem [112], such a setup can parametrize any given distribution, provided it has a sufficient amount of nodes. The optimal number of nodes and layers,

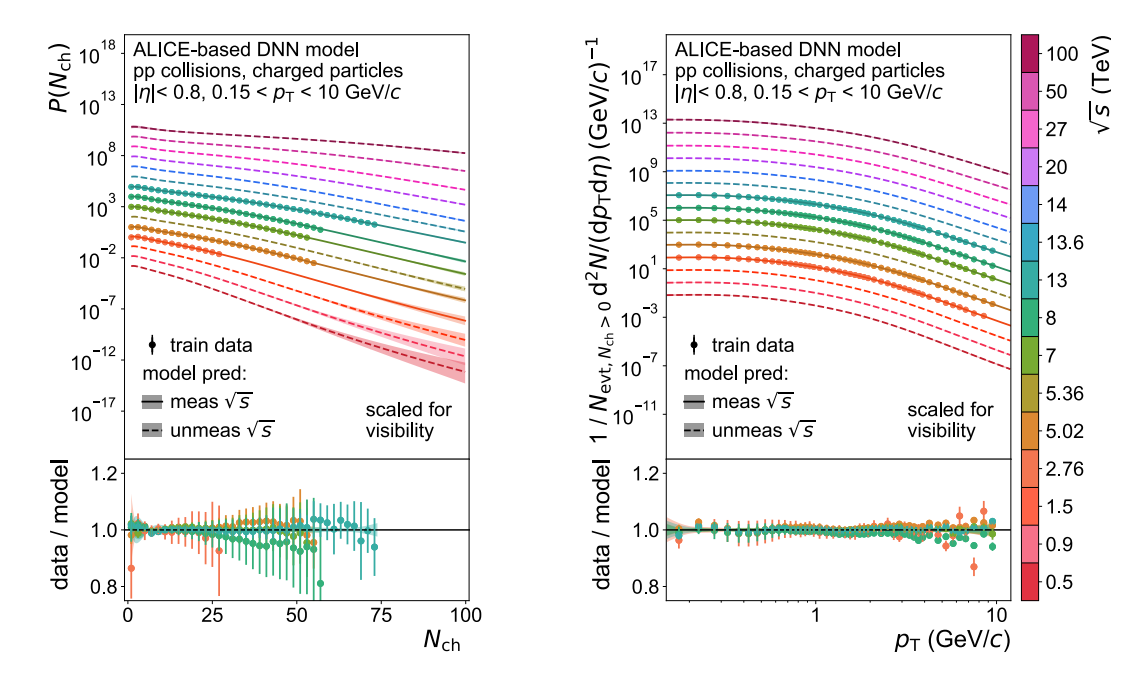


Figure 4.17: Multiplicity distributions (left) and $p_{\rm T}$ spectra (right) of pp collisions as predicted by DNNs trained on the measurements [108].

the activation function, and other so-called hyperparameters defining the network have to be determined by a search through many possible configurations. In the referenced studies, the \sqrt{s} extrapolation capability of different hyperparameter choices is evaluated by training the different network architectures on PYTHIA simulated data at the energies available from the LHC measurements and testing the model predictions against simulations at center-of-mass energies beyond the training data. The best model architecture is then trained with the ALICE data, enabling purely data-driven predictions that in contrast to PYTHIA and other event generators do not rely on QCD-inspired modeling of the collision. Systematic uncertainties of the predictions are determined by varying the choice of network architecture and the random initialization of its parameters. Figure 4.17 shows the resulting DNN predictions for selected energies in the range between $\sqrt{s} = 0.5$ TeV and 100 TeV. The ratios of the predictions to the training data indicate that the DNNs are capable of parametrizing the measurement well.

A prominent use case for interpolating transverse-momentum spectra to an unmeasured energy is the construction of a pp reference for calculating the nuclear modification factor R_{AA} in heavy-ion collisions. In the past, such interpolations relied either

on assuming a power-law dependence of particle production as a function of \sqrt{s} or on the energy dependence implemented in MC event generators.

The previously described study is discussed in more detail in Refs. [111, 108] and shows that the presented measurements serve as a crucial input for a data-driven prediction of the particle production at unmeasured collision energies.

4.4.2 Outlook: First results from LHC Run 3

During the LHC Run 3 data-taking campaign, pp collisions at $\sqrt{s} = 0.9 \, \text{TeV}$ and $\sqrt{s} = 13.6 \, \text{TeV}$ as well as Pb–Pb collisions at $\sqrt{s_{\text{NN}}} = 5.36 \, \text{TeV}$ were recorded. Together with the planned O–O and p–O collisions at the conjectured energies of approximately $\sqrt{s_{\text{NN}}} = 6.37 \, \text{TeV}$ and $\sqrt{s_{\text{NN}}} = 9 \, \text{TeV}$ [113], respectively, these measurements will extend the previously presented LHC Run 1 and 2 results of this thesis and thus provide further constraints to the theoretical modeling of high-energy collisions.

For LHC Run 3, the ALICE experiment underwent a major upgrade of its main tracking detectors. The new Inner Tracking System 2 (ITS2) consists of seven layers of silicon pixel detectors and the new TPC readout employs a GEM technology. This hardware upgrade allows for continuous data-taking with rates of about 500 kHz for pp, and 50 kHz for Pb–Pb collisions. To cope with the increased data rates, an entirely new software framework, called O², had to be developed both for the data reconstruction and the physics analyses.

In the scope of this work, the presented analysis is implemented in O², where equivalent event and track selection criteria are applied. The unfolding framework [79] developed for the LHC Run 1 and 2 measurements is employed for the corrections. Converted LHC Run 2 data is then used to validate the whole analysis chain.

Figure 4.18 shows first preliminary results for the mean and standard deviation of the multiplicity-dependent $p_{\rm T}$ spectra in pp collisions at $\sqrt{s}=0.9\,{\rm TeV}$ and $\sqrt{s}=13.6\,{\rm TeV}$ from LHC Run 3 together with the corresponding results from LHC Run 1 and 2. Even though the analysis of the LHC Run 3 data is still work in progress and lacks an estimate for the systematic uncertainties, these preliminary results align well with the previous measurements.

This demonstrates that the implementation of the analysis in O^2 is well advanced, suggesting that in the near future, the main results of this thesis can be extended to

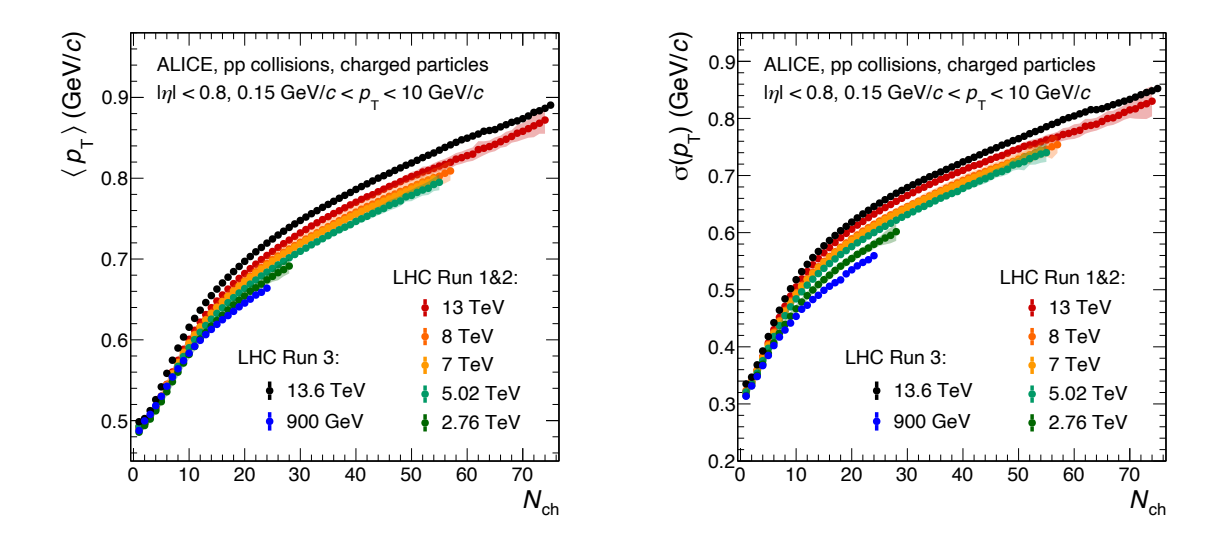


Figure 4.18: Mean (left) and standard deviation (right) of the transverse-momentum spectra as a function of $N_{\rm ch}$ for pp collisions with additional preliminary data from LHC Run 3.

include additional collision scenarios from the LHC Run 3 data-taking campaign.

5 Summary

This thesis presents a measurement of multiplicity-dependent charged-particle production in high-energy collisions at the Large Hadron Collider (LHC). The measurement includes ten datasets from LHC Run 1 and 2 covering pp collisions at $\sqrt{s} = 2.76$ TeV, 5.02 TeV, 7 TeV, 8 TeV and 13 TeV, p–Pb collisions at $\sqrt{s_{\rm NN}} = 5.02$ TeV and 8.16 TeV, Xe–Xe collisions at $\sqrt{s_{\rm NN}} = 5.44$ TeV, as well as Pb–Pb collisions at $\sqrt{s_{\rm NN}} = 2.76$ TeV and 5.02 TeV. For all datasets, the multiplicity ($N_{\rm ch}$) distributions and multiplicity-dependent transverse momentum ($p_{\rm T}$) spectra are measured within $|\eta| < 0.8$ and 0.15 GeV/ $c < p_{\rm T} < 10$ GeV/c. Only collisions with at least one charged particle produced in this kinematic range are considered.

The measurement is performed with the ALICE experiment, in particular using its main tracking detectors, the Inner Tracking System (ITS) and the Time Projection Chamber (TPC). Since trajectories of charged particles emerging from a collision are bent in the magnetic field of ALICE, their transverse momenta can be inferred from the curvature of the reconstructed tracks. Strict quality criteria are employed to select the reconstructed collisions and charged-particle tracks.

The selected sample of tracks has to be corrected for detector efficiency and acceptance, resolution effects and contaminating background in order to extract the underlying charged-particle production rates. The performance metrics of the measurement process are determined using Monte Carlo (MC) simulations consisting of an event generator based on a theoretical model of the collisions and a virtual representation of the ALICE experiment. Since an inaccurate composition of the different particle species in the event generator can bias the corrections extracted from the simulation, a data-driven procedure is employed to adjust the generated particle abundances.

The effects of efficiency, smearing, and contamination on the measurement of a given observable are corrected using the established Iterative Bayesian Unfolding (IBU) procedure. This method is employed to unfold the measured number of collisions as a function of the corresponding number of charged-particle tracks, providing the fully corrected multiplicity distribution. The same unfolding procedure cannot be applied for the correction of the $N_{\rm ch}$ and $p_{\rm T}$ dependent production rates of charged particles with a very high granularity in those two dimensions. In order to extract this observable, a novel sequential unfolding approach is developed, which can be employed using

the limited MC statistics. With this procedure, the transverse-momentum spectra are for the first time measured in single multiplicity intervals. The $\langle p_{\rm T} \rangle$ and standard deviation $\sigma(p_{\rm T})$ of these multiplicity-dependent $p_{\rm T}$ spectra are then compared for the ten datasets. Both observables decrease with increasing size of the collision system, following characteristic trends for pp, p-Pb, and AA collisions, respectively. Within the same system a clear ordering with center-of-mass energy is observed. While for pp and p-Pb collisions both $\langle p_{\rm T} \rangle$ and $\sigma(p_{\rm T})$ rise continuously as a function of $N_{\rm ch}$, in AA collisions the average transverse momentum only gradually increases over the wide range of multiplicities and the width of the $p_{\rm T}$ spectra saturates to an almost constant value. As a result, the relative spread around the mean $\sigma(p_T)/\langle p_T \rangle$ decreases as a function of $N_{\rm ch}$, which is a unique feature of AA collisions. The particles' transverse momenta are focussed closely around the mean value, possibly as a consequence of radial flow driving low- $p_{\rm T}$ particles towards higher momenta and high- $p_{\rm T}$ partons losing energy in the hot and dense QCD matter. Both medium effects are also visible when comparing the shape of the transverse-momentum spectra from particles produced in AA collisions with the corresponding shape in pp collisions at the same energy. The comparison shows an enhanced particle production at around $p_{\rm T} \approx 2\,{\rm GeV}/c$ and a reduced probability for producing high- $p_{\rm T}$ particles. The effect of parton energy loss is additionally illustrated by comparing the fraction of particles produced above $p_{\mathrm{T}}^{\mathrm{min}}=4\,\mathrm{GeV}/c$ or $p_{\mathrm{T}}^{\mathrm{min}}=5\,\mathrm{GeV}/c$ at different relative multiplicities with the one in peripheral collisions. A common decreasing trend of this relative fraction as a function of the relative multiplicity $N_{\rm ch}/\langle N_{\rm ch}\rangle$ is observed for Pb-Pb and Xe-Xe collisions. The probability densities $P(N_{\rm ch}/\langle N_{\rm ch}\rangle)$ of the relative multiplicity at different centerof-mass energies align for each system and agree within 20 % for pp and AA collisions and within 10 % for p-Pb collisions. For a given collision system, the ratio of the $p_{\rm T}$ spectra in relative multiplicity intervals to the multiplicity-integrated $p_{\rm T}$ spectrum is similar for the different center-of-mass energies. This indicates that even though the total energy available in a collision affects the charged-particle production, and changes both the average multiplicity and the shape of the $p_{\rm T}$ spectra, the relative change with $N_{\rm ch}/\langle N_{\rm ch} \rangle$ is universal. To illustrate this universality, the $\langle p_{\rm T} \rangle$ and $\sigma(p_{\rm T})$ of the spectra are normalized to their multiplicity-integrated values and shown as a function of the relative multiplicity. In this representation, the distributions at

different center-of-mass energies align almost perfectly for pp, p–Pb and AA collisions, respectively.

The presented measurements precisely characterize the charged-particle final state of a collision and thus provide a stringent test for theoretical models. For pp and p-Pb collisions, the widely used event generators PYTHIA and EPOS LHC are compared to the measured multiplicity distributions, p_T spectra, as well as $\langle p_T \rangle$ and $\sigma(p_T)$ as a function of $N_{\rm ch}$. While pp collisions are fairly well described by both generators, predicting charged-particle production in p-Pb collisions is still challenging, in particular for PYTHIA. For AA collisions, the same observables are compared to the HIJING event generator, which describes the multiplicity distributions well, but strongly underpredicts the average transverse momentum in the more central collisions and generally overestimates the high- $p_{\rm T}$ particle production. Additional predictions by EPOS3 and a hydrodynamical calculation with a CGC initial state prove incapable of predicting the measured $\langle p_{\rm T} \rangle - N_{\rm ch}$ correlation. The comparisons illustrate that a higher accuracy could still be achieved in the theoretical modeling of charged-particle production. To contribute to the process of improving the models, a RIVET analysis is implemented to facilitate future comparisons of the experimental data to various MC generators. The main results of this thesis are further complemented by two supplementary studies that highlight the potential for future research based on this work. First, the five pp datasets are used to make data-driven predictions for the multiplicity distributions and $p_{\rm T}$ spectra at unmeasured center-of-mass energies. Second, preliminary results from the LHC Run 3 data-taking campaign are presented for pp collisions at $\sqrt{s} = 0.9 \,\mathrm{TeV}$ and $13.6 \,\mathrm{TeV}$.

Looking to the future, the extensive dataset created in the course of this work, along with the anticipated extension to additional collision scenarios from LHC Run 3, holds great promise for significantly advancing our understanding of charged-particle production in high-energy collisions.

References

- [1] ALICE, "Multiplicity dependence of charged-particle production in pp, p-Pb, Xe-Xe and Pb-Pb collisions at the LHC", *Phys. Lett. B* 845 138110, arXiv:2211.15326 [nucl-ex], 2023.
- [2] A. Deur, S. J. Brodsky and G. F. de Teramond, "The QCD Running Coupling", Nucl. Phys. 90 1, arXiv:1604.08082 [hep-ph], 2016.
- [3] Particle Data Group, "Review of Particle Physics", PTEP 2022 083C01, 2022.
- [4] C. Bierlich *et al.*, "A comprehensive guide to the physics and usage of PYTHIA 8.3", *SciPost Phys. Codeb.* 2022 8, arXiv:2203.11601 [hep-ph], 2022.
- [5] H. Büsching, "Lecture notes on nuclear and particle physics", 2023.
- [6] S. Navin, "Diffraction in Pythia", LUTP-09-23, MCNET-10-09, arXiv:1005.3894 [hep-ph], 2010.
- [7] P. D. B. Collins, "An Introduction to Regge Theory and High Energy Physics", Cambridge Monographs on Mathematical Physics, Cambridge University Press, 2023.
- [8] V. N. Gribov, "Possible Asymptotic Behavior of Elastic Scattering", *JETP Lett.* 41 667–669, 1961.
- [9] F. Gelis, E. Iancu, J. Jalilian-Marian and R. Venugopalan, "The Color Glass Condensate", Ann. Rev. Nucl. Part. Sci. 60 463-489, arXiv:1002.0333 [hep-ph], 2010.
- [10] H. Weigert, "Evolution at small $x_{\rm bj}$: The Color glass condensate", *Prog. Part. Nucl. Phys.* 55 461–565, arXiv:hep-ph/0501087, 2005.
- [11] H. Satz, "Extreme states of matter in strong interaction physics. An introduction", Springer Verlag, New York, 2012.
- [12] J. C. Collins, D. E. Soper and G. F. Sterman, "Factorization of Hard Processes in QCD", Adv. Ser. Direct. High Energy Phys. 5 1-91, arXiv:hep-ph/0409313, 1989.

- [13] P. Skands, S. Carrazza and J. Rojo, "Tuning PYTHIA 8.1: the Monash 2013 Tune", Eur. Phys. J. C 74 no. 8, 3024, arXiv:1404.5630 [hep-ph], 2014.
- [14] T. Martin, P. Skands and S. Farrington, "Probing Collective Effects in Hadronisation with the Extremes of the Underlying Event", Eur. Phys. J. C 76 no. 5, 299, arXiv:1603.05298 [hep-ph], 2016.
- [15] B. Andersson, G. Gustafson, G. Ingelman and T. Sjostrand, "Parton Fragmentation and String Dynamics", *Phys. Rept.* 97 31–145, 1983.
- [16] M. L. Miller, K. Reygers, S. J. Sanders and P. Steinberg, "Glauber Modeling in High-Energy Nuclear Collisions", Ann. Rev. Nucl. Part. Sci. 57 205–243, arXiv:nucl-ex/0701025, 2007.
- [17] K. J. Eskola, H. Paukkunen and C. A. Salgado, "EPS09: A New Generation of NLO and LO Nuclear Parton Distribution Functions", *JHEP* 04 065, arXiv:0902.4154 [hep-ph], 2009.
- [18] M. Klasen and H. Paukkunen, "Nuclear PDFs After the First Decade of LHC Data", MS-TP-23-45, arXiv:2311.00450 [hep-ph], 2023.
- [19] P. Braun-Munzinger and B. Dönigus, "Loosely-bound objects produced in nuclear collisions at the LHC", Nucl. Phys. A 987 144-201, arXiv:1809.04681 [nucl-ex], 2019.
- [20] K. Werner, "Revealing a deep connection between factorization and saturation: New insight into modeling high-energy proton-proton and nucleus-nucleus scattering in the EPOS4 framework", *Phys. Rev. C* 108 no. 6, 064903, arXiv:2301.12517 [hep-ph], 2023.
- [21] T. Pierog et al., "EPOS LHC: Test of collective hadronization with data measured at the CERN Large Hadron Collider", Phys. Rev. C 92 no. 3, 034906, arXiv:1306.0121 [hep-ph], 2015.
- [22] ALICE, "The ALICE experiment A journey through QCD", CERN-EP-2022-227, arXiv:2211.04384 [nucl-ex], 2022.

- [23] J. F. Grosse-Oetringhaus and K. Reygers, "Charged-Particle Multiplicity in Proton-Proton Collisions", J. Phys. G 37 083001, arXiv:0912.0023 [hep-ex], 2010.
- [24] ALICE, "Charged-particle multiplicities in proton-proton collisions at $\sqrt{s} = 0.9$ to 8 TeV", Eur. Phys. J. C 77 no. 1, 33, arXiv:1509.07541 [nucl-ex], 2017.
- [25] Z. Koba, H. B. Nielsen and P. Olesen, "Scaling of multiplicity distributions in high energy hadron collisions", *Nucl. Phys. B* 40 317–334, 1972.
- [26] UA5, "Scaling Violation Favoring High Multiplicity Events at 540 GeV CMS Energy", *Phys. Lett. B* 138 304–310, 1984.
- [27] UA5, "Charged Particle Multiplicity Distributions at 200 GeV and 900 GeV Center-Of-Mass Energy", Z. Phys. C 43 357, 1989.
- [28] ABCDHW, "Charged Multiplicity Distribution in p p Interactions at ISR Energies", *Phys. Rev. D* 30 528, 1984.
- [29] CMS, "Charged Particle Multiplicities in pp Interactions at $\sqrt{s} = 0.9$, 2.36, and 7 TeV", JHEP 01 079, arXiv:1011.5531 [hep-ex], 2011.
- [30] ALICE, "Charged-particle multiplicity measurement in proton-proton collisions at $\sqrt{s}=0.9$ and 2.36 TeV with ALICE at LHC", Eur. Phys. J. C 68 89–108, arXiv:1004.3034 [hep-ex], 2010.
- [31] UA5, "A New Empirical Regularity for Multiplicity Distributions in Place of KNO Scaling", *Phys. Lett. B* 160 199–206, 1985.
- [32] ALICE, "Centrality dependence of particle production in p-Pb collisions at $\sqrt{s_{\rm NN}}=5.02$ TeV", Phys. Rev. C 91 no. 6, 064905, arXiv:1412.6828 [nucl-ex], 2015.
- [33] ALICE, "Centrality determination of Pb-Pb collisions at $\sqrt{s_{\rm NN}}=2.76$ TeV with ALICE", *Phys. Rev. C* 88 no. 4, 044909, arXiv:1301.4361 [nucl-ex], 2013.

- [34] ALICE, "Transverse momentum spectra and nuclear modification factors of charged particles in pp, p-Pb and Pb-Pb collisions at the LHC", *JHEP* 11 013, arXiv:1802.09145 [nucl-ex], 2018.
- [35] CMS, "Transverse-momentum and pseudorapidity distributions of charged hadrons in pp collisions at $\sqrt{s} = 7$ TeV", Phys. Rev. Lett. 105 022002, arXiv:1005.3299 [hep-ex], 2010.
- [36] A. A. Bylinkin and A. A. Rostovtsev, "Parametrization of the shape of hadron-production spectra in high-energy particle interactions", *Phys. Atom.* Nucl. 75 999–1005, 2012.
- [37] PHENIX, "Detailed measurement of the e^+e^- pair continuum in p+p and Au+Au collisions at $\sqrt{s_{\rm NN}}=200$ GeV and implications for direct photon production", *Phys. Rev. C* 81 034911, arXiv:0912.0244 [nucl-ex], 2010.
- [38] ALICE, "Multiplicity dependence of the average transverse momentum in pp, p-Pb, and Pb-Pb collisions at the LHC", *Phys. Lett. B* 727 371–380, arXiv:1307.1094 [nucl-ex], 2013.
- [39] UA1, "Transverse Momentum Spectra for Charged Particles at the CERN Proton anti-Proton Collider", *Phys. Lett. B* 118 167–172, 1982.
- [40] ABCDHW, "Multiplicity dependence of the average transverse momentum and of the particle source size in p-p interactions at $\sqrt{s} = 62$, 44 and 31 GeV", Z. Phys. C 33 333, 1987.
- [41] UA1, "A study of the general characteristics of proton-antiproton collisions at $\sqrt{s} = 0.2$ TeV to 0.9 TeV", Nucl. Phys. B 335 261–287, 1990.
- [42] T. Alexopoulos *et al.*, "Multiplicity Dependence of the Transverse Momentum Spectrum for Centrally Produced Hadrons in Antiproton-Proton Collisions at $\sqrt{s} = 1.8$ TeV", *Phys. Rev. Lett.* 60 1622, 1988.
- [43] STAR, "Multiplicity dependence of inclusive p_t spectra from p-p collisions at $\sqrt{s} = 200$ GeV", Phys. Rev. D 74 032006, arXiv:nucl-ex/0606028, 2006.

- [44] CDF, "Measurement of particle production and inclusive differential cross sections in $p\bar{p}$ collisions at $\sqrt{s} = 1.96$ TeV", *Phys. Rev. D* 79 112005, arXiv:0904.1098 [hep-ex], 2009. [Erratum: Phys.Rev.D 82, 119903 (2010)].
- [45] ALICE, "Transverse momentum spectra of charged particles in proton-proton collisions at $\sqrt{s} = 900$ GeV with ALICE at the LHC", *Phys. Lett. B* 693 53-68, arXiv:1007.0719 [hep-ex], 2010.
- [46] ATLAS, "Charged-particle multiplicities in pp interactions measured with the ATLAS detector at the LHC", New J. Phys. 13 053033, arXiv:1012.5104 [hep-ex], 2011.
- [47] ALICE, "Pseudorapidity and transverse-momentum distributions of charged particles in proton-proton collisions at $\sqrt{s} = 13$ TeV", *Phys. Lett. B* 753 319–329, arXiv:1509.08734 [nucl-ex], 2016.
- [48] ALICE, "Transverse momentum spectra and nuclear modification factors of charged particles in Xe–Xe collisions at $\sqrt{s_{\rm NN}}=5.44$ TeV", *Phys. Lett. B* 788 166–179, arXiv:1805.04399 [nucl-ex], 2019.
- [49] G. Cowan, "Statistical Data Analysis", Oxford science publications, Clarendon Press, 1998.
- [50] G. D'Agostini, "A multidimensional unfolding method based on Bayes' theorem", Nucl. Instrum. Meth. A 362 487–498, 1995.
- [51] B. Malaescu, "An Iterative, Dynamically Stabilized (IDS) Method of Data Unfolding", PHYSTAT 2011 271-275, arXiv:1106.3107 [physics.data-an], 2011.
- [52] A. Hocker and V. Kartvelishvili, "SVD approach to data unfolding", *Nucl. Instrum. Meth. A* 372 469–481, arXiv:hep-ph/9509307, 1996.
- [53] S. Schmitt, "TUnfold: an algorithm for correcting migration effects in high energy physics", JINST 7 T10003, arXiv:1205.6201 [physics.data-an], 2012.

- [54] A. Andreassen et al., "OmniFold: A Method to Simultaneously Unfold All Observables", Phys. Rev. Lett. 124 no. 18, 182001, arXiv:1911.09107 [hep-ph], 2020.
- [55] M. Backes, A. Butter, M. Dunford and B. Malaescu, "An unfolding method based on conditional invertible neural networks (cINN) using iterative training", SciPost Phys. Core 7 no. 1, 007, arXiv:2212.08674 [hep-ph], 2024.
- [56] N. Huetsch *et al.*, "The Landscape of Unfolding with Machine Learning", arXiv:2404.18807 [hep-ph], 2024.
- [57] J. F. Grosse-Oetringhaus, "Measurement of the Charged-Particle Multiplicity in Proton-Proton Collisions with the ALICE Detector". PhD thesis, University of Muenster, 2009.
- [58] T. Bayes and R. Price, "An essay towards solving a problem in the doctrine of chances", *Phil. Trans. R. Soc.* 53 370–418, 1763.
- [59] M. J. Kuusela, "Uncertainty quantification in unfolding elementary particle spectra at the Large Hadron Collider". PhD thesis, Ecole Polytechnique Lausanne, 2016.
- [60] W. H. Richardson, "Bayesian-Based Iterative Method of Image Restoration", J. Opt. Soc. Am. 62 no. 1, 55–59, 1972.
- [61] L. B. Lucy, "An iterative technique for the rectification of observed distributions", *Astron. J.* 79 745–754, 1974.
- [62] T. Adye, "Unfolding algorithms and tests using RooUnfold" in *PHYSTAT 2011*, pp. 313-318. CERN, Geneva, 2011. arXiv:1105.1160 [physics.data-an].
- [63] O. S. Brüning *et al.*, "LHC Design Report", CERN Yellow Reports: Monographs, CERN, Geneva, 2004.
- [64] J. Gronefeld, "Transverse Momentum Distributions and Nuclear Modification Factors in Heavy-Ion Collisions with ALICE at the Large Hadron Collider". PhD thesis, Technical University Darmstadt, 2018.

- [65] ALICE, "Schematics of the ALICE expeirment", https://alice-figure.web.cern.ch/node/11219, 2017.
- [66] ALICE, "The ALICE experiment at the CERN LHC", JINST 3 S08002, 2008.
- [67] ALICE, "Performance of the ALICE VZERO system", JINST 8 P10016, arXiv:1306.3130 [nucl-ex], 2013.
- [68] ALICE, "Alignment of the ALICE Inner Tracking System with cosmic-ray tracks", JINST 5 P03003, arXiv:1001.0502 [physics.ins-det], 2010.
- [69] ALICE, "Technical Design Report for the Upgrade of the ALICE Inner Tracking System", J. Phys. G 41 087002, 2014.
- [70] ALICE, "Upgrade of the ALICE Time Projection Chamber", CERN-LHCC-2013-020, ALICE-TDR-016, 2013.
- [71] J. Alme *et al.*, "The ALICE TPC, a large 3-dimensional tracking device with fast readout for ultra-high multiplicity events", *Nucl. Instrum. Meth. A* 622 316–367, arXiv:1001.1950 [physics.ins-det], 2010.
- [72] ALICE TPC, "The upgrade of the ALICE TPC with GEMs and continuous readout", JINST 16 no. 03, P03022, arXiv:2012.09518 [physics.ins-det], 2021.
- [73] ALICE, "Performance of the ALICE Experiment at the CERN LHC", Int. J. Mod. Phys. A 29 1430044, arXiv:1402.4476 [nucl-ex], 2014.
- [74] R. Fruhwirth, "Application of Kalman filtering to track and vertex fitting", Nucl. Instrum. Meth. A 262 444–450, 1987.
- [75] ALICE, "The ALICE definition of primary particles", 2017.
- [76] S. G. Weber and A. Andronic, "ALICE event display of a Pb-Pb collision at 2.76A TeV" 2015. General Photo.
- [77] X.-N. Wang and M. Gyulassy, "HIJING: A Monte Carlo model for multiple jet production in p p, p A and A A collisions", *Phys. Rev. D* 44 3501–3516, 1991.

- [78] R. Brun *et al.*, "GEANT Detector Description and Simulation Tool", CERN-W5013, CERN-W-5013, W5013, W-5013, 1994.
- [79] M. Krüger, "UnfoldingFramework", https://gitlab.cern.ch/mkruger/unfoldingframework.
- [80] M. Krüger, "SciRooPlot", https://github.com/SciRooPlot/SciRooPlot.
- [81] P. Z. Skands, "Tuning Monte Carlo Generators: The Perugia Tunes", Phys. Rev. D 82 074018, arXiv:1005.3457 [hep-ph], 2010.
- [82] ALICE, "Enhanced production of multi-strange hadrons in high-multiplicity proton-proton collisions", Nature Phys. 13 535-539, arXiv:1606.07424 [nucl-ex], 2017.
- [83] ALICE, "Multiplicity dependence of π , K, and p production in pp collisions at $\sqrt{s}=13$ TeV", Eur. Phys. J. C 80 no. 8, 693, arXiv:2003.02394 [nucl-ex], 2020.
- [84] P. Huhn, Personal communication.
- [85] P. Huhn, "Datenbasierte Effizienzkorrektur zum Nachweis geladener Teilchen im ALICE Experiment" Master's thesis, Goethe University Frankfurt, 2017.
- [86] ALICE, "Multiplicity dependence of (multi-)strange hadron production in proton-proton collisions at $\sqrt{s} = 13$ TeV", Eur. Phys. J. C 80 no. 2, 167, arXiv:1908.01861 [nucl-ex], 2020.
- [87] ALICE, "Multiplicity dependence of charged pion, kaon, and (anti)proton production at large transverse momentum in p-Pb collisions at $\sqrt{s_{\rm NN}} = 5.02$ TeV", *Phys. Lett. B* 760 720–735, arXiv:1601.03658 [nucl-ex], 2016.
- [88] ALICE, "Multiplicity Dependence of Pion, Kaon, Proton and Lambda Production in p-Pb Collisions at $\sqrt{s_{\rm NN}}=5.02$ TeV", *Phys. Lett. B* 728 25–38, arXiv:1307.6796 [nucl-ex], 2014.
- [89] ALICE, "Centrality dependence of π , K, p production in Pb-Pb collisions at $\sqrt{s_{\rm NN}}=2.76$ TeV", Phys. Rev. C 88 044910, arXiv:1303.0737 [hep-ex], 2013.

- [90] M. Krüger, "Analysis Note: Multiplicity dependence of charged-particle production in pp, p-Pb, Xe-Xe and Pb-Pb collisions at the LHC", https://alice-publications.web.cern.ch/node/8188.
- [91] P. Huhn, "Analysis Note: Re-weighting Monte Carlo abundances", https://alice-notes.web.cern.ch/node/1311.
- [92] IPPP Durham, "HEPData", https://www.hepdata.net/.
- [93] ALICE, "Charged-particle multiplicity measurement with Reconstructed Tracks in pp Collisions at $\sqrt{s} = 0.9$ and 7 TeV with ALICE at the LHC", ALICE-PUBLIC-2013-001, 2013.
- [94] ALICE, "Charged-particle production as a function of multiplicity and transverse spherocity in pp collisions at $\sqrt{s} = 5.02$ and 13 TeV", Eur. Phys. J. C 79 no. 10, 857, arXiv:1905.07208 [nucl-ex], 2019.
- [95] ALICE, "Centrality and pseudorapidity dependence of the charged-particle multiplicity density in Xe–Xe collisions at $\sqrt{s_{\rm NN}} = 5.44$ TeV", *Phys. Lett. B* 790 35–48, arXiv:1805.04432 [nucl-ex], 2019.
- [96] ALICE, "Centrality Dependence of the Charged-Particle Multiplicity Density at Midrapidity in Pb–Pb Collisions at $\sqrt{s_{\rm NN}} = 2.76$ TeV", Phys. Rev. Lett. 106 032301, arXiv:1012.1657 [nucl-ex], 2011.
- [97] ALICE, "Centrality Dependence of the Charged-Particle Multiplicity Density at Midrapidity in Pb-Pb Collisions at $\sqrt{s_{\rm NN}}=5.02$ TeV", Phys. Rev. Lett. 116 no. 22, 222302, arXiv:1512.06104 [nucl-ex], 2016.
- [98] M. Krüger, "Bayesian unfolding of charged particle p_T spectra with ALICE at the LHC", PoS Confinement2018 236, arXiv:1909.06109 [hep-ex], 2018.
- [99] C. Bierlich, G. Gustafson, L. Lönnblad and H. Shah, "The Angantyr model for heavy-ion collisions in PYTHIA8", JHEP 10 134, arXiv:1806.10820 [hep-ph], 2018.
- [100] J. R. Christiansen and P. Z. Skands, "String Formation Beyond Leading Colour", JHEP 08 003, arXiv:1505.01681 [hep-ph], 2015.

- [101] L. Lönnblad and H. Shah, "A spatially constrained QCD colour reconnection in pp, pA, and AA collisions in the PYTHIA8/Angantyr model", Eur. Phys. J. C 83 no. 7, 575, arXiv:2303.11747 [hep-ph], 2023. [Erratum: Eur.Phys.J.C 83, 639 (2023)].
- [102] B. Schenke, C. Shen and P. Tribedy, "Running the gamut of high energy nuclear collisions", *Phys. Rev. C* 102 no. 4, 044905, arXiv:2005.14682 [nucl-th], 2020.
- [103] C. Bierlich *et al.*, "Robust Independent Validation of Experiment and Theory: Rivet version 3", *SciPost Phys.* 8 026, arXiv:1912.05451 [hep-ph], 2020.
- [104] A. M. Rossi *et al.*, "Experimental study of the energy dependence in proton-proton inclusive reactions", *Nucl. Phys. B* 84 269–305, 1975.
- [105] E735, "Multiplicity dependence of transverse momentum spectra of centrally produced hadrons in $\bar{p}p$ collisions at 0.3, 0.54, 0.9, and 1.8 TeV center of mass energy", *Phys. Lett. B* 336 599–604, 1994.
- [106] CDF, "Transverse Momentum Distributions of Charged Particles Produced in $\bar{p}p$ Interactions at $\sqrt{s}=630$ GeV and 1800 GeV", Phys. Rev. Lett. 61 1819, 1988.
- [107] CMS, "Transverse Momentum and Pseudorapidity Distributions of Charged Hadrons in pp Collisions at $\sqrt{s} = 0.9$ and 2.36 TeV", *JHEP* 02 041, arXiv:1002.0621 [hep-ex], 2010.
- [108] M. A. Calmon Behling, J. Jung, M. Krüger and H. Büsching, "Modeling $N_{\rm ch}$ distributions and $p_{\rm T}$ spectra in high-energy pp collisions with DNNs". To be published.
- [109] A. Giovannini and R. Ugoccioni, "Possible scenarios for soft and semihard components structure in central hadron hadron collisions in the TeV region", Phys. Rev. D 59 094020, arXiv:hep-ph/9810446, 1999. [Erratum: Phys.Rev.D 69, 059903 (2004)].

- [110] D. R. Herrera *et al.*, "Entropy and heat capacity of the transverse momentum distribution for pp collisions at RHIC and LHC energies", *Phys. Rev. C* 109 no. 3, 034915, arXiv:2402.07372 [hep-ph], 2024.
- [111] M. A. Calmon Behling, "Modeling charged-particle spectra of proton-proton collisions in ALICE using deep neural networks" Bachelor's thesis, Goethe University Frankfurt, 2023.
- [112] K. Hornik, M. Stinchcombe and H. White, "Multilayer feedforward networks are universal approximators", *Neural Networks* 2 no. 5, 359–366, 1989.
- [113] ALICE, "ALICE physics projections for a short oxygen-beam run at the LHC", https://cds.cern.ch/record/2765973, 2021.

Acknowledgements

In the course of this thesis I have received invaluable help and guidance from many people, to whom I owe deep gratitude. First and foremost I want to thank Prof. Henner Büsching for the consistent support and encouragement throughout the years. Apart from the many inspiring discussions about physics and beyond, I am very grateful for the numerous opportunities to attend conferences and workshops which helped me grow and expand my knowledge. I extend my sincere thanks to Prof. Harald Appelshäuser for kindly agreeing to examine this thesis.

The presented analysis was only possible through the close and fruitful collaboration with several colleagues. In particular the contributions of Patrick Huhn, who implemented the data-driven corrections and set up the MC simulations, are crucial to this work. I really enjoyed sharing the office with him and tackling the many technical problems that we encountered along the way. I am also grateful to Michael Knichel, whose extraordinary knowledge and expertise was invaluable especially at the beginning of the project. Special thanks are due to Prof. Anton Andronic and Kai Schweda, whose ideas and constant encouragement were crucial for both the outcome of this analysis and its publication. I also wish to acknowledge the ALICE internal reviewing committees for their constructive feedback.

My time spent on this thesis has been profoundly shaped by the people of the ALICE group in Frankfurt. The coffee breaks, excursions, and social activities created a supportive and enjoyable working environment. I owe much of my knowledge about ALICE and CERN to my former colleagues Stefan Heckel, Pascal Raisig, and Ernst Hellbär with whom I shared many memorable 'Falafel Fridays'. I am also grateful to Joshua König and Tim Rogoschinski for the many inspiring discussions. A special 'thank you' goes to Sebastian Scheid, whose companionship during ALICE shifts, conferences, and the TPC uncabeling created some unforgettable memories. The motivation and new perspectives I gained through the collaboration with Jerome Jung and Maria Calmon Behling were instrumental for me to gain enough momentum on the final stretch towards finishing this thesis. I want to express my deepest gratitude to Matthias Kleiner for proofreading the manuscript and for motivating me in the final months. Finally, I want to thank Stefanie Mrozinski for her invaluable feedback and encouragement that helped me complete this thesis.



